AD NUMBER

AD832027

NEW LIMITATION CHANGE

TO

Approved for public release, distribution unlimited

FROM

Distribution authorized to U.S. Gov't. agencies and their contractors; Administrative/Operational use; 1 May 1968. Other requests shall be referred to Naval Ordnance Laboratory, White Oak, MD .

AUTHORITY

NOL ltr, 15 Nov 1971

AD832027

AN EXPERIMENTAL INVESTIGATION OF THE
AERODYNAMIC CHARACTERISTICS OF
SLENDER HYPERSONIC VEHICLES AT HIGH
ANGLES OF ATTACK

NOL

1 MAY 1968

UNITED STATES NAVAL ORDNANCE LABORATORY, WHITE OAK, MARYLAND

NOLTR 68-52

DDC

RECEIVED

MAY 16 1968

C

AN EXPERIMENTAL INVESTIGATION OF THE AERODYNAMIC CHARACTERISTICS OF SLENDER HYPERSONIC VEHICLES AT HIGH ANGLES OF ATTACK

Prepared by:
Robert H. Feldhuhn
Lionel Pasiuk

ABSTRACT: An experimental investigation of the aerodynamic character-
istics of flows around highly inclined axisymmetric configurations
has been conducted in the Hypersonic Tunnel at the U. S. Naval
Ordnance Laboratory, White Oak, at a nominal Mach number of 6 and
at nominal free stream Reynolds numbers per foot of 2.4×10^6 and
21×10^6. Static longitudinal force coefficients, surface pressure
distributions, and heat transfer distributions were measured with a
slightly blunted slender cone ($R_n/R_b = 0.025$, $\theta_c = 5°$) at angles of
attack as large as 54 degrees. The static longitudinal force
coefficients of a slightly blunted 2/3 power law body of revolution
($R_n/R_b = 0.025$, fineness ratio = 5.61), and two ducted cones were
also measured. Additional information concerning the separated flow
field on the leeward side of the inclined cone was determined from
schlieren photographs, surface oil flow patterns, and Pitot tube
surveys which were conducted in the most leeward meridian plane.

The pressure distributions on the windward side of the cone and
the normal force coefficients of the simple bodies of revolution were
adequately predicted by Newtonian theory. Flow separation, as
determined from surface oil flow patterns, was found to occur in a
region on the cone where an adverse pressure gradient exists in the
circumferential direction. Furthermore, a region of attached flow
was found to exist near the plane of symmetry on the leeward side
of the cone at angles of attack below approximately 25 degrees. The
pressure distributions along the leeward meridian generator of an
inclined cone were found to be dependent upon the Reynolds number.

The addition of a duct about the cone was found to substantially
increase the lift to drag ratio at this Mach number.

U. S. NAVAL ORDNANCE LABORATORY
WHITE OAK, MARYLAND

i

NOLTR 68-52   1 May 1968

AN EXPERIMENTAL INVESTIGATION OF THE AERODYNAMIC CHARACTERISTICS
  OF SLENDER HYPERSONIC VEHICLES AT HIGH ANGLES OF ATTACK

This report presents the results of the first phase of an experimental
investigation of fluid dynamic phenomena associated with inclined
axisymmetric configurations at hypersonic velocities. Pressure,
heat transfer, force, flow field surveys and flow visualization
measurements are presented for an inclined slightly blunted 5° half
angle cone at a Mach number of 6. Force measurements were also
obtained for a slightly blunted 2/3 power law body and two ducted-
cone configurations.

                                    E. F. SCHREITER
                                    Captain, USN
                                    Commander

                                    L. H. SCHINDEL
                                    By direction

CONTENTS

LIST OF SYMBOLS

A_b base area of model

$A_{Capture}$ capture area of duct $\dfrac{\pi D_D^2}{4}$

A_{ref} reference area

C_A axial force coefficient $\dfrac{\text{measured axial force}}{q\,A_b}$

C_D drag coefficient $\dfrac{C_N \sin\alpha + C_A \cos\alpha}{q\,A_b}$

C_L lift coefficient $\dfrac{C_N \cos\alpha - C_A \sin\alpha}{q\,A_b}$

C_N normal force coefficient $\dfrac{\text{measured normal force}}{q\,A_b}$

C_p specific heat of air at constant pressure

C_v specific heat of air at constant volume

C_w specific heat of material

D_D diameter of duct

d thickness of material

F fineness ratio $\dfrac{L}{2R_b}$

h heat transfer coefficient $\dfrac{\dot{q}}{T_o - T_w}$

k thermal conductivity of material

L body length

L_D diameter of duct

ℓ distance from insulated back surface

M Mach number

P_b base pressure

P_c static pressure on surface of cone

P_o stagnation pressure

P_∞ free-stream static pressure

q   free-stream dynamic pressure

$\dot{q}$ heat transfer rate per unit area

x distance from vertex measured along the surface of the cone

Re   Reynolds number: $Re_{\infty,L} = \dfrac{\rho_\infty U_\infty L}{\mu_\infty}$; $Re_{\infty,S} = \dfrac{\rho_\infty U_\infty S}{\mu_\infty}$;

$$Re_{e,S} = \frac{\rho_e U_e S}{\mu_e}; \quad Re_{e,\theta} = \frac{\rho_e U_e \theta}{\mu_e};$$

$$Re_{r_n,\infty} = \frac{\rho_\infty U_\infty R_n}{\mu_\infty}; \quad Re_{\infty,X} = \frac{\rho_e U_e X}{\mu_e}$$

R_b base radius

R_n tip radius of curvature

S   distance from the tip measured along the surface of the cone

S_t Stanton number $\dfrac{h}{\rho U C_p}$

$\overline{S_t}_{\infty=0}$ calculated stagnation-streamline Stanton number for a yawed cylinder

T_e equilibrium temperature

T_o free-stream stagnation pressure

T_w wall temperature

U   velocity

X   distance from tip of model measured along the axis of symmetry

$X_{c.p.}$ distance of the center of pressure from tip of model measured along axis of symmetry

Y   radial distance of surface from axis of symmetry

Z   distance along axis of 2/3 power law body measured from the virtual tip

α   angle of attack

α_m thermal diffusivity

γ   ratio of specific heats $\frac{C_p}{C_v}$

δ   boundary layer thickness

θ $\int_0^\delta \left(\frac{\rho U}{\rho_e U_e}\right)\left[1 - \left(\frac{U}{U_e}\right)\right]dy$ = boundary layer momentum thickness

θ_c cone half angle

μ   absolute viscosity

ρ   density of gas

ρ_w density of material

τ   time

φ   azimuthal angle measured from most windward meridian plane

Subscripts

e   local conditions at the outer edge of the boundary layer

∞   free-stream conditions

ix

INTRODUCTION

Slender axisymmetric shapes possess several favorable features which make them prime candidates for high acceleration hypersonic flight. Specifically, axisymmetric conical shapes and slender power law shapes are of interest because these configurations are nearly optimum if one only considers center of pressure variation or aerodynamic drag respectively (refs. (1) through (4)). However, if a body is required to achieve large lateral acceleration, axisymmetric configurations must sustain a large angle of attack, or maintain a very high velocity in order to compensate for their low lift effectiveness. Both of these alternatives lead to rather substantial increases in convective heat transfer. Furthermore, the possibility of sustaining rather large angles of attack immediately confronts the designer with the fact that there will be regions of separated flow on the leeward side of the cone.

It is the purpose of this investigation to provide some fundamental data concerning the aerothermodynamic properties of the flow fields around highly inclined bodies of revolution at hypersonic speeds. One specific objective of this study is to provide some experimental force, heat transfer and pressure data at a hypersonic Mach number where a substantial portion of the model is surrounded by a turbulent boundary layer. An additional objective of the present investigation is to provide some data on axisymmetric bodies

which provide higher lift to drag ratios at hypersonic speeds than

circular conical bodies.

EXPERIMENTAL APPARATUS

1. **Test Facility**

The present investigation was conducted in the Hypersonic
Tunnel at the Naval Ordnance Laboratory at a nominal Mach number
of 6. A two-dimensional contoured nozzle was used during this
investigation. Dry air, the test gas, is compressed and stored in
a bottle field. Before passing into the tunnel, the gas is heated
in a pebble bed heater to a temperature large enough to prevent
condensation. The wind tunnel is an open jet blowdown facility
which at stagnation pressures below 40 atmospheres exhausts
through a fixed diffuser and an aftercooler into a compressor-
driven exhaust system. At supply pressures above 40 atmospheres,
the air is exhausted into the atmosphere after passing through the
diffuser and a silencer. Testing time varies from approximately
two minutes at supply pressures of 100 atmospheres to continuous
operation at supply pressures of 10 atmospheres. A complete
description of the capabilities and the instrumentation of this
facility is given in reference (5).

During these experiments, all of the models were supported
with a simple sting which passes through the base of the model.
The entire model support assembly is attached to a sector at the
base of the sting. The sector is capable of continuously pitching
a model through a total angle of attack range of 75 degrees. The
angle of attack was determined from the output of a servo-driven
potentiometer that was driven by the sector.

2. <u>Models and Instrumentation</u>

    a.   Pressure and Heat Transfer Experiments

Two models with identical overall dimensions were used to obtain the cone pressure and heat transfer data ($\theta_c = 5°$, $R_n/R_b = 0.025$, $L = 13.967$ inches). The pressure model was fabricated from stainless steel and had a nominal wall thickness of 0.063 inches. A sketch is given in figure 1. The locations of the pressure orifices are tabulated in figure 1. At two stations on the pressure model four orifices were circumferentially distributed 90 degrees from each other in order to provide a means of checking for proper alignment with the flow. With the exception of the alignment orifices, all of the pressure taps were equally spaced along two conical rays 180 degrees apart. The diameter of the orifices for the first three pressure taps along each ray was 0.027 inches. The remainder of the orifices were 0.047 inches in diameter. Each orifice was connected to an absolute pressure transducer by a length of stainless steel tubing. During the experiments that were conducted at supply pressures of 10 atmospheres ($Re_\infty/ft = 2.4 \times 10^6$) 15 psia strain gage pressure transducers were employed with the pressure orifices on the windward side and 5 psia strain gage pressure transducers were employed with the pressure orifices on the leeward side. For the 100 atmosphere test conditions ($Re_\infty/ft = 21 \times 10^6$), 100 psia strain gage pressure transducers were employed for the windward measurements and 5 psia transducers were employed for the leeward measurements. The pressure transducers were housed in sealed water cooled containers in the test cell. These containers allow for the simultaneous calibration of up to 96 pressure transducers (ref. (6)).

Heat transfer measurements were made with a stainless steel thin skin slightly blunted conical heat transfer model whose outside dimensions were the same as those of the pressure model. The wall thickness was machined to a nominal value of 0.020 inches. The actual wall thickness at each station which was used in the data reduction was measured by X-ray techniques and is tabulated in Table I. Chromel-Alumel thermocouple wire with a nominal diameter of 0.005 inch was used to instrument the thin wall model. The locations of the thermocouples and the station where the alignment orifices were positioned are noted in figure 1.

b. Static Force and Moments Experiments

Static force measurements were obtained with four different configurations. Sketches of the models used during this program are shown in figures 2 through 5. All of these measurements were obtained with internal water cooled strain gage balances.

The configuration designated 6FN has the same exterior dimensions as the slightly blunted conical pressure and heat transfer models discussed previously. (θ_c = 5°, R_n/R_b = 0.025, L = 13.967 in.)

A slightly blunted body of revolution whose radius (beyond the juncture of the hemispherical nose tip and the afterbody) varies as the axial distance to the 2/3 power was fabricated from stainless steel. This configuration will be referred to as 6FX-1 and is shown in figure 3. At the juncture of the spherical tip with the 2/3 power law afterbody, the radius and slope of the body were continuous. The fineness ratio and nose to base radius ratio of this configuration were 5.61 and 0.025 respectively.

5

Two ducted cone force models were also built to investigate
the possibility of substantially increasing the lift to drag ratio
of bodies of revolution. These configurations designated as
6FX-2-1 and 6FX-2-2, are shown in figures 4 and 5, respectively.
The conical tip and cowl leading edges on each of these configura-
tions was less than 0.005 inch thick. The inner surface of the
duct on configuration 6FX-2-1 was tapered while the inner surface
of the duct on configuration 6FX-2-2 was cylindrical. On each
of these configurations, there were four struts which fastened
the duct to the center-body. Holes were drilled in the struts
to equalize the surface pressure in an attempt to minimize the
lift contribution of the struts. The base of each strut was
flat.

For all the above mentioned configurations normal force,
pitching moment, side force, yawing moment and axial force coefficients
were measured with multicomponent internal balances. The output
of these balances was recorded and stored on magnetic tape.

c. Data Acquisition System

All of the pressure, heat transfer and force data obtained
during the experiments were recorded on magnetic tape. The analog-
digital data recording system in the Hypersonic Tunnel at NOL is
fully described in reference (7). The system features a 12 channel
capability with a data sampling rate of approximately 250 pieces
of data per second. During normal usage ten channels are available
for recording experimental data and two channels are employed to
record supply temperature and supply pressure. A multiplexing

capability of the system allows one to place more than one transducer on each channel. Advantage was taken of this feature during the heat transfer and pressure experiments.

d. Flow Field Investigation

In order to obtain some information concerning the flow field upon the leeward side of a slender cone three different techniques were employed.

1. Optical flow visualization methods:

Schlieren photographs were taken during the pressure, heat transfer, and force experiments. The schlieren system of the Hypersonic Tunnel is a conventional single pass system. A continuous light source (mercury arc lamp) provided the necessary illumination for the schlieren photographs. The knife edge in the schlieren system was horizontal for these experiments.

2. Pitot Tube Survey:

Pitot tube surveys were conducted in the leeward meridian plane of the cone by traversing a Pitot tube in the vertical center-plane of the wind tunnel. The Pitot tube was aligned with the flow direction in the undisturbed free stream. The position of the probe and the Pitot pressure were determined from the outputs of a geared potentiometer and an absolute pressure transducer respectively. The inlet of the Pitot tube was circular and had an outside diameter of 0.063 inches.

3. Oil Flow Studies:

In order to obtain some information relating to the local flow direction near the surface of the cone, some oil flow experiments were made. A mixture of lamp black and silicone oil was

applied to the model at random points. Three protractors were built in order to make angular measurements of the separation point at three different stations.

EXPERIMENTAL PROCEDURE

The investigation was conducted with a wind tunnel nozzle designed to provide a uniform flow at Mach 6. The actual Mach number within the test section depends upon the supply conditions. Average free stream conditions are tabulated below:

Mach Number	Reynolds Number/Ft	Stagnation Pressure	Stagnation Temperature
5.93	2.4×10^6	147 psia	960°R
5.96	4.4×10^6	294 psia	1000°R
6.00	2.1×10^7	1470 psia	1010°R

The Mach number varies by less than ± 0.04 from the average value within the test section. Free stream stagnation conditions were measured in the settling chamber upstream of the nozzle throat. Stagnation pressure was measured with an absolute strain gage pressure transducer. Stagnation temperature was measured with a shielded thermocouple. The voltage outputs of these instruments were recorded on magnetic tape during the experiments and the test conditions were determined at each instant of time. At the given Mach number, free stream conditions were obtained from the measured stagnation conditions by assuming that the gas expands isentropically from the stagnation chamber conditions. Stagnation pressure was controlled during the tests by a tunnel operator who monitored the stagnation pressure from a Bourdon gage.

A brief outline of the test program is given in the table below:

Type of Test	Nominal Angle of Attack	M_∞	Re_∞/ft	Remarks
1. Pressure	$0°,10°,20°,30°,45°,54°$	5.93	2.4×10^6	$0° \le \varphi \le 180°$
	$0°,20°,30°,45°,54°$	6.00	21×10^6	$0° \le \varphi \le 180°$
2. Heat Transfer	$0°,15°,30°,54°$	5.93	2.4×10^6	$0° \le \varphi \le 180°$ $\Delta\varphi = 15°$ $T_w/T_o \sim 0.5$
	$0°,20°,30°,45°,54°$	6.00	21×10^6	$\Delta\varphi = 15°$ $T_w/T_o \sim 0.5$ $T_w/T_o \sim 0.3$
3. Force	$0° - 54°$	5.96	4.4×10^6	Config. 6FN
	$0° - 54°$	6.00	21×10^6	Config. 6FN
	$0° - 54°$	6.00	21×10^6	Config. 6FX-1
	$0° - 15°$	6.00	21×10^6	Config. 6FX-2-1
	$0° - 15°$	6.00	21×10^6	Config. 6FX-2-2
4. Flow Visualization	$10°,15°,20°,30°,40°$	5.93	2.4×10^6	Oil Flow Experiments
5. Pitot Survey	$15°,30°,45°$	5.93	2.4×10^6	Leeward Meridian Plane

1. Pressure Experiments

The pressure measurements were obtained by first pitching the model to the desired angle of attack and then rolling the model about its axis of symmetry in order to obtain the pressure distribution in the circumferential direction. The output of pressure transducers connected with one windward and one leeward pressure tap

respectively, were monitored on an X-Y plotter to minimize the
pressure response time errors. All of the outputs from the pressure
transducers were recorded on magnetic tape and compared with the
calibration obtained for each test.

2. Heat Transfer Experiments

Heat transfer coefficients were obtained by recording the
temperature time variation of the thin wall heat transfer model and
reducing the data in the manner described in ref. (8). Initially
the model was pitched to the angle of attack required for the test
and then covered with a retractable cooling shield. The model was
cooled by spraying liquid nitrogen over its surface until the model
temperature reached some predetermined level. Data at two initial
average wall to total temperature ratios $(T_w/T_o \sim 0.35$ & $0.55)$ were
obtained in this manner during the high Reynolds number experiments
$(M = 6$ $Re_\infty/ft = 21 \times 10^6)$, while data at one average wall tempera-
ture ratio $(T_w/T_o \sim 0.55)$ were obtained during the low Reynolds
number experiments $(M_\infty = 5.93$ $Re_\infty/ft = 2.4 \times 10^6)$. Once the desired
wall temperature was reached and while the model was still covered
by the shield, the flow was established in the wind tunnel. The
cooling shield was retracted after the steady flow was established
at the desired supply pressure. Approximately 0.5 seconds were
required for the shield to clear the model when the model was
inclined at an angle of attack of 54 degrees.

Heat transfer coefficients were calculated by assuming that the
convective heat transfer locally increases the body temperature and
that the effects of conduction along and normal to the skin could

10

be neglected. A simple heat balance relating the convective heat transfer with the heat capacity of the solid then leads to the following ordinary differential equation.

$$\rho_w C_w \; d \left[1 - \frac{d}{2r \tan \theta_c} \right] \frac{dT_w}{d\tau} = -h(T_w - T_e) \tag{1}$$

In order to facilitate the data reduction, this equation was integrated with the assumptions that the specific heat varies linearly with the temperature $C_w = C_{w_0} [1 + \epsilon T]$, the equilibrium temperature T_e is the total temperature T_0, and that h is independent of the temperature.

The result obtained is:

$$\frac{\rho_w C_{w_0} d}{\tau_2 - \tau_1} \left[1 - \frac{d}{2r \tan \theta_c} \right] \left\{ (1+\epsilon T_0) \ln \frac{T_1 - T_0}{T_2 - T_0} - \epsilon(T_2 - T_1) \right\} = h \tag{2}$$

The values of C_{w_0} and ϵ for each interval of time were determined curve fits to available measurements of the specific heat of 17-4PH stainless steel. These expressions for the specific heat (BTU/lb°R) are shown below:

$$T \leq 560°R \qquad C_w = 0.08836 + 0.05773 \left[\frac{T}{310} - 1 \right] - 0.03161 \left[\frac{T}{310} - 1 \right]^2$$

$$T > 560°R \qquad C_w = 0.1043 + 0.00002 \; T$$

Heat transfer coefficients were calculated from eq. (2) for several increments of time from the measured temperature variation. No conduction corrections have been made to the measured data that are presented. The errors introduced by conduction are discussed in the appendix of this report.

11

3. Oil Flow Experiments

Dots of oil were randomly applied to the surface of the model before the test. The cooling shield used for the heat transfer experiments was lowered over the model to prevent the oil pattern from being disturbed while steady flow was established within the tunnel. These tests were conducted at a Mach number of 5.93 and at average free stream Reynolds numbers based upon model length of 2.7×10^6. Once flow was established the shield was withdrawn from the model for approximately 30 seconds. After the oil flow pattern was established, the shield was placed over the model prior to tunnel shutdown. The pattern was examined after each test and angular measurements of separation lines were made at three stations located 5.7, 8.5, and 11.4 inches from the tip. The angular measurements are estimated to be accurate to within $\pm 5°$.

4. Pitot Tube Survey

Pitot tube surveys were conducted in the most leeward meridian plane of an inclined slightly blunted slender cone ($\theta_c = 5°$, $R_n/R_b = 0.025$) at a Mach number = 5.93 and at average free stream Reynolds number per foot = 2.4×10^6. These surveys were obtained while the model was inclined at angles of attack of 15°, 30° and 45°. The probe was traversed perpendicular to the free stream flow direction. The distance of the tip of the Pitot tube from the tip of the cone is tabulated below for each angle of attack.

α	Distance from cone tip
15°	7-5/16"
30°	7-1/16"
45°	7-1/16"

12

The output of the potentiometer which indicated the linear displacement of the probe and the output of the pressure transducers which measured the Pitot pressure were monitored on an x-y recorder and recorded by the data acquisition system on magnetic tape. The model that was used to obtain the surface pressure distributions was also used during the Pitot tube surveys. The pressure model was aligned so that one row of pressure orifices was in the leeward meridian plane. These pressures were also recorded during the survey. The orifice just upstream of where the Pitot tube touched the cone, varied by less than 5 percent during the surveys. One Pitot tube was used for all of the surveys.

5. Force and Moment Experiments

The force experiments were conducted with four different configurations. Average test conditions for each configuration are tabulated below:

Configuration	M_∞	$Re_{\infty,L}$
6FN	6.00	25×10^6
6FN	5.96	5.2×10^6
6FX-1	6.00	25×10^6
6FX-2-1	6.00	33×10^6
6FX-2-2	6.00	29×10^6

Force data were obtained from the output of calibrated mult-component strain gage balances. The output of the balance was continuously recorded while the model was pitched through a specified angle of attack variation. A tare run was conducted for each test to account for the effects of the weight of the model. The balances were calibrated by statically loading the balance with weights at

13

different stations in the manner described in reference(9). The
experimental uncertainties in the normal force coefficient, axial
force coefficient and center of pressure data are tabulated below.

Configuration	ΔC_N	ΔC_A	$\Delta \frac{Xcp}{L}$
Cone - 6FN	±0.02	±0.006	±0.005
2/3 Power Law - 6FX-1	±0.02	±0.006	±0.005
Ducted Cone - 6FX-2-1	±0.04	±0.010	±0.010
Ducted Cone - 6FX-2-2	±0.04	±0.010	±0.010

The balances were calibrated to account for the deflection
induced by the normal loads. The measured angle of attack was
corrected to account for this deflection. The maximum uncertainty
associated with the angle of attack measurements is estimated to
be $\pm0.30°$. Base pressures were measured behind the cone and 2/3
power law body by running 1/8" O.D. stainless steel tubing along
the sting to the base of the model.

The presented drag data includes base pressure drag.

RESULTS AND DISCUSSION

1. Pressure measurements and oil flow experiments

The measured surface pressure distributions on a slightly blunted
inclined cone for the two test conditions $\left[M_\infty = 5.93, \text{Re}_{\infty,L} = 2.8 \times 10^6 \right.$
and $\left. M_\infty = 6.00 \text{ Re}_{\infty,L} = 25 \times 10^6 \right]$ are presented in figures 7-19. The
pressure distributions along different conical generators are shown in
figures 7-15 while the circumferential pressure distribution at a station
4 inches from the tip is shown in figures 16-19. The circumferential
data are compared with the results of calculations based upon Newtonian
flow theory. These Newtonian calculations were obtained from the formula

14

$$\frac{P_c}{P_\infty} = 1 + \gamma M_\infty^2 \left[\cos\alpha \ \sin\theta_c + \sin\alpha \ \cos\theta_c \ \cos\phi \right]^2 \qquad (3)$$

The Newtonian theory predicts the measured pressure distribution to within 10 percent on the windward side of the cone for $\phi < 60°$. The agreement between the measured surface pressure distribution on the windward side of an inclined cone in a hypersonic flow and the Newtonian theory has been observed previously by several investigators (references (10)-(12)). It is noted in figures 7-15 that the pressure distribution along the windward generators shows virtually no dependence upon the distance from the tip of the cone. The invariance of the pressure distribution with respect to distance would certainly be the case if the flow were conical.

In the leeward meridian plane, it is observed that the surface pressure distribution varies with Reynolds number (figures 20-22). One explanation for this observation is that the variation of pressure on the leeward side of the cone is associated with a weak interaction between the inviscid flow and viscous flow in a fashion similar to that which occurs on sharp flat plates, wedges and cones.

It is also noted that a minimum in the circumferential static pressure distributions occurs at an azimuthal angle of approximately 125 degrees for both the high and low Reynolds number data (figures 17 and 19). Angular measurements, which were obtained during the low Reynolds number oil flow pattern experiments (figures 23 and 24) indicated that flow separation occurs at approximately 135 degrees (figure 25).

To within the accuracy of the present data ($\pm 5^\circ$), flow separation appears to occur along a conical generator. The appearance of a separation line very close to a local minimum in pressure is consistent with the data presented by Avduesky and Medvedev (ref. (13)) and Tracy (ref. (11).

In addition to measuring a separation line at approximately 135°, a second separation line was found near the leeward meridian plane at angles of attack below 20° (figures 24 and 25). The oil dots in the region between these two separation lines remained essentially undisturbed. During the oil flow experiments performed at angles of attack of 30° and 40° all the dots of oil remained stationary beyond 135°. The shear which disturbed the oil dots near the leeward meridian plane at moderate angles of attack is associated with a locally attached flow. Additional effects associated with this flow can be found in the heat transfer data, the Pitot tube surveys and the schlieren pictures to be presented in subsequent sections.

2. Heat Transfer Experiments

The heat transfer data are presented in figures 26-36. For convenience, the measured data have been nondimensionalized by properties in the undisturbed free stream.

a. Zero Angle of Attack Heat Transfer Distribution

The measured heat transfer distribution along the surface of the unyawed cone are presented in figure 26 along with calculations based upon the results presented in reference (14) for the laminar heat transfer distribution along sharp cones at zero angle of attack.

Inspection of the zero angle of attack heat transfer data indicates that boundary layer transition occurs over a range of

free stream Reynolds numbers (based upon length from the tip) of 10×10^6 to 14×10^6. The calculated variation of local Reynolds numbers based upon momentum thickness and distance from the tip are presented in figures 27 and 28 for the conditions corresponding to the larger ratio of wall temperature to stagnation temperature. The calculated local Mach number distributions are shown in figure 29. These results were obtained from calculations of the luminar boundary layer growth on a slightly blunted cone by the Momentum Integral technique as described by R. E. Wilson in reference (16). At zero angle of attack, the calculated local conditions at which transition occurs are tabulated below:

$$10 \times 10^6 < Re_{\infty,S} < 14 \times 10^6$$

$$4.45 < Me < 4.75$$

$$5.4 \times 10^6 < Re_{e,S} < 9.5 \times 10^6$$

$$950 < Re_{e,\theta} < 1250$$

For these test conditions, the effects of wall temperature introduced changes no greater than 4 percent in the calculated properties. Furthermore, the present variation of wall temperature did not introduce any large changes in the location of the region where boundary layer transition occurs at zero angle of attack.

b. Heat Transfer Distribution on the Inclined Cone

Data which is representative of measurements obtained with a slender slightly blunted cone inclined at large angles of attack are presented in figures 30-36. The data obtained along the most windward streamline of the cone are presented in figures 30 and 31.

17

The laminar heat transfer along this streamline is compared with the results of an analysis by Reshotko and Beckwith (ref. (15)). In reference (15), the laminar heat transfer coefficient along the windward streamline of a yawed cylinder is given by the equation:

$$h_\Lambda = \frac{\dot{q}}{T_{aw} - T_w} = \frac{k_w}{\mu_w}(\theta'_w)_{Pr=1.0} Pr^{0.46}\sqrt{\rho_w \mu_w \left(\frac{D}{u_\infty}\frac{du_e}{dx}\right)\frac{u_\infty}{D}}$$

This result can be put in the following form from which the laminar heat transfer distribution along the most windward streamline of an inclined cone may be calculated:

$$S_{t_\infty}\Big|_{\omega=0}\sqrt{Re_\infty} = 0.707(\theta'_w)_{Pr=1.0} Pr^{-0.54}\left(\frac{T_w - T_{aw}}{T_w - T_0}\right)\sqrt{\frac{T_\infty \mu_w}{T_w \mu_\infty}\left(\frac{P}{P_\infty}\right)_\alpha \frac{D}{u_\infty}\frac{du_e}{dx}\frac{Sin(\alpha+\theta_c)}{Sin\,\theta_c}}$$

where

$$\left(\frac{P}{P_\infty}\right)_\alpha = 1 + \gamma M_\infty^2\left[Cos\alpha\,Sin\theta_c + Sin\alpha\,Cos\theta_c\right]^2$$

$$\frac{D}{u_\infty}\frac{du_e}{dx} = \frac{2}{M_\infty Sin(\alpha+\theta_c)}\left[1 + \frac{\gamma-1}{2}M_\infty^2 Sin^2(\alpha+\theta_c)\right]^{\frac{1}{2}}\sqrt{\frac{2}{\gamma}\left[1 - \frac{1}{\left(\frac{P}{P_\infty}\right)_\alpha}\right]}$$

The quantity $(\theta'_w)_{Pr=1}$ is a function of the wall temperature, the free stream Mach number, and the angle of yaw of the most windward streamline. This parameter was obtained from calculations of Reshotko and Beckwith (ref. (15)) of the laminar flow over a yawed infinite cylinder.

The local Mach number, which is needed to calculate the dimensionless temperature ratio, $\left(\frac{T_w - T_{aw}}{T_w - T_0}\right)$, was determined from

18

the Newtonian expression for the surface pressure $\left(\frac{P}{P_\infty}\right)_\alpha$ and the measured shock wave inclination with respect to the free stream.

For the angles of attack at which these experiments were conducted, boundary layer transition along the most windward streamline occurred closer to the tip when the model was inclined at an angle of attack then it did when it was at zero angle of attack. At angles of attack greater than 30°, boundary layer transition occurred at a Reynolds number based upon free stream conditions of approximately 2×10^6.

At the present time, not enough data has been obtained to demonstrate conclusively the effects of wall temperature and free stream unit Reynolds number upon boundary layer transition on a highly inclined cone. The present data do appear to indicate that cooling the wall tends to stabilize the laminar boundary layer (figures 30 and 31). This is evidenced in the data obtained at 20° and 30° angle of attack. At an angle of attack of 20°, the free stream transition Reynolds number increased from approximately 3×10^6 to 4×10^6 when the ratio of wall to stagnation temperature was decreased from 0.62 to 0.35. The data obtained at an angle of attack of 30° indicate agreement with laminar calculations of the heat transfer rate at a wall to stagnation temperature ratio of 0.33 and a free stream Reynolds number of 1.6×10^6. The data point obtained at an angle of attack of 30° and at an average wall temperature of 0.57 is about 50 percent greater than that obtained at this angle of attack at the lower wall temperature ratio.

An attempt was made to correlate the measured turbulent heat transfer distribution by fairing a curve of the form $S_{t_\infty} Re_\infty^{0.2} =$ constant

through the data for each test condition. The curves obtained for each test condition are shown in figures 30 and 31 and the constants are tabulated below.

Curve	α	T_w/T_o	$St_\infty Re_\infty^{0.2}$
	20	0.32	0.101
	20	0.60	0.089
	30	0.30	0.134
	30	0.57	0.119
	45	0.33	0.159
	45	0.62	0.151
	54	0.37	0.148
	54	0.66	0.147

The circumferential heat transfer distributions at four stations along the cone are shown in figures 32-36. The measured Stanton numbers have been normalized by the stagnation streamline Stanton number (at the given Reynolds number) as calculated from the results presented in references (14) and (15). The data presented in figures 32, 33, and 34 were obtained at angles of attack of 15°, 30°, and 54°, respectively at a free stream Mach number of 5.93 and an average stream Reynolds number per foot of 2.49×10^6. For these conditions, transition did not occur on the windward streamline within the interval where the measurements were made. The data presented in figures 35 and 36 were obtained at angles of attack of 20° and 54°, respectively, at a free stream Mach number of 6.00 and at an average free stream Reynolds number per foot of 20.2×10^6. The measured circumferential data for these conditions have also been normalized by the stagnation streamline Stanton number which one would calculate by assuming that the flow was laminar (reference (15)).

In comparing these results several features are readily apparent:

20

(1) With the exception of the data obtained at an angle of attack of 20° (figure 35), all of the circumferential heat transfer distributions obtained show a local maximum along the stagnation streamline. The heat transfer data obtained at an angle of attack of 20° ($Re_\infty/ft \approx 21 \times 10^6$) indicate that at the first three stations ($x < 2.50$), a local maximum in the heat transfer distribution occurs between 15° and 30° from the windward meridian. At stations further downstream ($x > 6.25$) a local maximum was measured along the windward meridian.

One plausible explanation for these results is that for a given angle of attack, transition occurs closer to the tip along generators that are further displaced from the windward genera'or. Consequently, the flow along the windward streamline might well be laminar while the flow at the same axial location but at a different azimuthal station will be turbulent. However, when the flow at a given axial station was either completely laminar or completely turbulent, a local maximum was measured along the windward generator.

(2) In addition to the observations concerning the nature of the heat transfer on the windward streamline, it was generally noted (figures 32-36) that the heat transfer distributions reached their lowest values at approximately 120-135° from the windward meridian plane. At angles of attack equal to or larger than 30°, (figures 33, 34 and 36) the variation in the circumferential heat transfer distribution beyond 135° from the windward meridian was negligible. At angles of attack less than 30° (figures 32 and 35), the heat transfer distributions show both a local minimum and a local maximum on the leeward side.

Flow separation on the leeward side of the inclined cone is one
mechanism that could provide an explanation for these observations.
As noted in a previous section, surface oil flow studies provide some
information concerning the extent of the separated flow field upon
the leeward side of the cone. The measurement of a minimum in the
heat transfer distribution between 120° and 135° is consistent with
the observation of flow separation at approximately 135°. The
increase of heat transfer near the leeward meridian plane at angles
of attack of 15° and 20° can be attributed to the fact that there
is a region of attached flow on the leeward side near the plane of
symmetry. The oil flow studies indicated that this region extends
approximately 10-15° from the leeward meridian plane. The appearance
of heat transfer distributions in the plane of symmetry on the
leeward side of an inclined cone which are characterized by a local
maximum in the azimuthal direction is consistent with the results
obtained by Tracey (reference (11)) and Fitch, Morris and Dunkin
(reference (17)), with slender cones at angles of attack between
10° and 24°.

3. Flow Field Surveys and Flow Visualization

In addition to the pressure and heat transfer measurements,
a limited series of Pitot tube surveys were obtained in the most
leeward meridian plane of the slightly blunted cone. These measure-
ments were obtained at a Mach number of 5.93 and at an average free
stream Reynolds number per foot of 2.4×10^6. The results of these
measurements are presented in figures 37-39. (The probe distance
that is referred to in these results is the distance between the
surface and the bottom of the Pitot tube.)

Analysis of the Pitot surveys along with schlieren photographs is particularly useful since a schlieren photograph is sensitive to the density gradient while the Pitot probe measurement varies approximately directly with ρu^2 at Mach numbers above 2. The schlieren pictures, presented in figures 40 and 41 were obtained during the Pitot traverses while the model was at 15° and 30° angle of attack. The schlieren pictures presented in figures 42 and 43 were obtained during the high Reynolds number force experiments when the model was at 16.2° and 27.5° angle of attack. The variation of the sensitivity of schlieren system with the change of density within the test section is apparent.

Three regions between the shock wave and the leeward surface of the cone can be distinguished in the schlieren photographs and the Pitot tube surveys. The large gradients in the Pitot pressure survey occur at approximately the same position as the density gradients that were observed in schlieren photographs. These results indicate that large density gradients exist in the leeward meridian plane. Without a total temperature distribution, it is difficult to determine solely from the Pitot tube surveys whether these gradients are due to viscous or inviscid phenomena associated with the flow around an inclined cone.

The concurrent examination of schlieren photographs and Pitot surveys also provides some useful information concerning the flow field near the body on the leeward side of the cone. In schlieren photographs that were obtained at angles of attack less than 25° ($Re_\infty/ft \sim 21 \times 10^6$) a region was noted near the base of the cone (see figure 42) which appears like a Prandtl-Meyer expansion fan

that one observes on flat based bodies in a sup rsoni flow.   The
Pitot survey conducted in the most leeward meridian plane at an
angle of attack of 15° indicates a Pitot pressure of approximately
4 times as large as the static surface pressure when the probe was
touching the surface.   At angles of attack larger than 25° the
Prandtl-Meyer like expansion fan on the leeward side was no longer
observable in the schlieren photographs (figure 43).   Furthermore,
in the Pitot tube surveys conducted at angles of attack of 30° and
45° (figures 38 and 39), the measured Pitot pressure differed by
less than 10 percent from the measured static pressure at the
surface of the cone.   These results in conjunction with the heat
transfer and oil experiments are indicative of the fact that there
is a region of attached energetic flow near the leeward meridian
plane of a slender cone inclined at a moderate angle of attack
($\alpha < 25°$).

4.   Static Force and Moment Measurements

The data obtained during the force experiments are presented
in figures 44-53.

a.   Configuration 6FN - Slightly blunted cone ($\theta_c = 5°$,
$R_n/R_b = 0.025$, L = 13.967 inches)

In figure 44, the measured normal and axial force coefficients
for an inclined slender cone are presented and compared with
calculations based upon Newtonian theory.   The calculations were
obtained from the results tabulated in reference (18).   These
calculations were obtained by assuming that in regions exposed to
the incident flow, the surface pressure distribution is given by
the relationship $C_p = 2Cos^2\eta$ (where η is the angle between the

incident free stream and the normal to the body surface). In these
calculations, the surface pressure is assumed to be the free stream
static pressure in regions that were shielded from the incident flow.

In addition to comparing the measured normal and axial force
coefficients with numerical calculations based upon Newtonian theory,
the measurements are compared with some previous experimental data
(reference (19)) obtained with a sharp 5° half angle cone at a Mach
number of 6.9 and a Reynolds number based upon model length of 2.8 x
10^6. The agreement between the measured normal force coefficients
and the Newtonian theory is quite good.

In order to assess the comparison between the present axial
force coefficient measurements with those presented in reference (19),
one should note that the total axial force coefficient is:

$$C_A = C_{A_{Skin\ Friction}} + C_{A_{Fore\ Body}} + C_{A_{Base}}$$

The present data include all three contributions to C_A, whereas
the data of reference (19) include only the first two terms. By
calculating the contribution of the base to the axial force coefficient
from the measured base pressure shown in figure 45, it can be shown
that the discrepancy apparent in the axial force measurements in
figure 44 is due primarily to the contribution of $C_{A_{Base}}$.

A calculation was made in order to assess the contributions
of skin friction drag, pressure drag, and base pressure drag to the
total drag coefficient at zero angle of attack. Pressure drag and
skin friction drag of a slightly blunted cone at zero angle of
attack were calculated using the Momentum Integral method described

25

in reference (16). The base pressure drag was determined from the measured base pressure. The contributions of each of these components are tabulated below along with the measured drag coefficient at zero angle of attack. ($Re_{\infty,tr}$ is the free-stream Reynolds number at which transition is assumed to occur in the calculations.)

CASE	I	II	III	IV
P_o	294 psia	294 psia	1470 psia	1470 psia
$Re_{\infty,L}$	5×10^6	5×10^6	25×10^6	25×10^6
$Re_{\infty,tr}$	∞	3.5×10^6	6×10^6	10×10^6
$C_{D_{Pressure}}$ (Calc)	0.023	0.023	0.022	0.022
$C_{D_{Skin\ Friction}}$ (Calc)	0.008	0.016	0.014	0.013
$C_{D_{Base\ Pressure}}$ (Measured)	0.032	0.032	0.036	0.036
$C_{D_{Pressure}} + C_{D_{Skin\ Friction}} + C_{D_{Base\ Press.}}$	0.063	0.071	0.072	0.071
$C_{D_{Measured}}$	$0.073 + 0.006 -$	$0.073 + 0.006 -$	$0.079 + 0.006 -$	$0.079 + 0.006 -$

In view of the experimental uncertainty, the agreement between the measurements and the calculations is considered to be satisfactory.

Lift and drag data are presented in figure 46. A maximum lift to drag ratio of 2.4 was measured for the cone at an angle of attack of 10 degrees. A maximum lift coefficient of 1.88 was measured at angle of attack of $48°$. For these test conditions; the effects of the variation of Reynolds number are negligible.

The measured center of pressure locations for the conical configuration and the three other configurations to be discussed later are presented in figure 47. It has been observed previously (references (3) and (4)) that sharp circular cones have a minimal variation of the center of pressure. This invariance of the center of pressure is associated with the conical nature of the inviscid flow field around a circular cone. The location of the center of pressure of an inclined sharp circular cone in an ideal gas is given by the relation $\frac{Xc.p}{L} = \frac{2}{3Cos^2\theta_c}$ as long as the shock wave is attached, the flow is locally supersonic and viscous effects do not alter the pressure distribution or introduce appreciable shearing moments. At large angles of attack, the measured center of pressure location of the slightly blunted cone lies ahead of the theoretical value for a sharp circular of the same length. In the results of reference (20), it was noted that the center of pressure location of slightly blunted cones at large angles of attack can be adequately estimated by the following equation:

$$\frac{Xc.p}{L} = \frac{\frac{2}{3Cos^2\theta_c}\left[\frac{1 - \left(\frac{R_n}{R_b}\right)^3 Cos^3\theta_c}{1 - \left(\frac{R_n}{R_b}\right)^2 Cos^2\theta_c}\right] - \frac{R_n}{R_b}\frac{(1-Sin\theta_c)}{Cos\theta_c}}{1 - \frac{R_n}{R_b}\frac{(1-Sin\theta_c)}{Cos\theta_c}} \tag{5}$$

In figure 47 one observes excellent agreement between this equation and the measured data.

b.   2/3 Power law body (R_n/R_b = 0.025, Fineness ratio = 5.61)

Force measurements were obtained with a slightly blunted 2/3 power law body at a Mach number of 6.00 and at an average free stream Reynolds number based upon model length of 25 x 10^6.

Normal force and axial force coefficients are presented in figure 48 along with previous experimental measurements obtained with a 2/3 power law body of fineness ratio 5.55 (reference (1)) at a Mach number of 10.03 a   a Reynolds number based upon free stream conditions and the length of the model of 1.4 x 10^6. Calculations based upon Newtonian flow theory are also presented. As was noted in the case of the slender cone, Newtonian theory adequately predicts the normal force coefficients.

The axial force coefficient at zero angle of attack was measured to be 0.075. As in the case of the slender cone, base drag contributes a substantial portion of the total drag coefficient of a slender body at Mach 6. The difference between the measured axial force coefficients and the experimental data presented in reference (1) is due primarily to the differences in the base drag at M = 6 and M = 10.

Lift and drag are presented in figure 49. A maximum lift to drag ratio of 2.63 was measured at angle of attack of 10°. A lift coefficient of 2.20 was measured at angle o attack of 49°.

The measured center of pressure position is plotted in figure 47 for the 2/3 power law configuration. It is noted that over an angle of attack variation from 5° to 50° the center of

pressure varies by approximately 2.5 percent of the body length.

c. Ducted Cone Configurations (6FX-2-1, 6FX-2-2)

Force measurements were obtained with two ducted cone configurations (figures 4 and 5). The center body of each configuration was dimensionally similar. The duct of the first configuration (6FX-2-1) was positioned so that a straight line drawn between the point of maximum thickness within the duct and the vertex would coincide with the shock wave near the tip of the cone at zero angle of attack at $M_\infty = 6$. The duct of the second configuration (6FX-2-2) was positioned such that the lip of the duct would intersect the shock wave emanating from the vertex of the cone at zero angle of attack.

The experiments were conducted at a Mach number of 6.00 and at average free stream Reynolds numbers based upon model length (distance measured from the tip) of 30×10^6 and 29×10^6 for configurations 6FX-2-1 and 6FX-2-2 respectively.

The measured normal force and axial force coefficients of these configurations are presented in figures 50 and 52. (The reference area in all of the measured force coefficients is the maximum cross sectional area of the center body.)

A fair estimation of the measured normal force coefficient of an axisymmetric body surrounded by a thin duct in a hypersonic flow was provided by the following result:

$$C_N = 2 \, Sin\alpha \, Cos\alpha \, \frac{A_{Capture}}{A_{Ref.}} + \frac{4}{3} \frac{L_D D_D}{A_{Ref.}} \, Sin^2\alpha \qquad (6)$$

The first term in the above expression is obtained by assuming that a thin cylindrical shell captures all of the mass flow that is intercepted by the frontal area projected on a plane normal to the

free stream. The flow is assumed to be turned through an angle α, by the duct. In the process of turning through the angle α, it is assumed that the normal component of the momentum in the free stream is transferred to the body while the tangential component of momentum is conserved. In addition to the generation of a force due to a momentum exchange within the body, there is also a contribution associated with the interaction between the free stream and the outer surface of the cylindrical shell. The second term in the above expression is the normal force coefficient for an inclined cylindrical section as determined from Newtonian theory (reference (21)). The above analysis provides a useful means of estimating the normal force coefficients of these configurations.

The measured lift and drag data are presented in figures 51 and 53. It is noted that while the drag coefficient of these configurations are between 2 and 3 times that of the simple bodies of revolution described earlier, the maximum lift to drag ratios of these configurations at Mach 6 are approximately 20 percent to 50 percent higher than the measured lift to drag ratio of the simple bodies of revolution.

The measured center of pressure variation is presented in figure 47. (This data is non-dimensionalized by the length between the vertex of the cone and back of the duct.)

CONCLUSIONS

An experimental investigation concerning the aerothermodynamic characteristics of the flows around highly inclined bodies of revolution has been conducted in a wind tunnel at a nominal Mach

number of 6. From this investigation, the following conclusions are made concerning hypersonic flow around inclined axisymmetric bodies:

(1) The pressure and force measurements have verified the adequacy of Newtonian theory for the prediction of normal force coefficients and pressure distributions on the windward surfaces of inclined slender axisymmetric bodies at large angles of attack.

(2) The heat transfer measurements have verified the adequacy of the theory of Reshotko and Beckwith for predicting laminar heat transfer on the most windward side streamline of slender bodies inclined at large angles of attack.

(3) The flow was found to separate on the leeward side of the inclined cone (at an azimuthal angle of approximately $135°$) in a region where an adverse circumferential pressure gradient exists. A region of attached flow was observed near the leeward meridian plane of the $5°$ half angle cone at angles of attack below approximately $25°$.

(4) The pressure distribution on the leeward side of the cone was found to vary with the Reynolds number based upon the distance from the tip of the cone.

(5) A relative maximum was measured in the heat transfer distribution on the leeward side of the cone at moderate angles of attack.

(6) The measured maximum lift to drag ratio of the ducted conical bodies was as much as 50 percent greater than the maximum lift to drag ratio of the simple bodies of revolution for the specific Mach number and Reynolds number conditions of the present tests. The increase in the lift to drag ratio is realized solely because of the increase in lift effectiveness of these configurations.

TABLE I

X	Wall Thickness (inches)
1.00	0.018
1.75	0.018
2.50	0.018
3.25	0.018
4.00	0.018
4.75	0.018
5.50	0.019
6.25	0.019
7.00	0.019
7.7:	0.019
8.50	0.019
9.25	0.020
10.00	0.020
10.75	0.020
11.50	0.020
12.25	0.020

REFERENCES

1. Spencer, Bernard, Jr. and Fox, Charles H.. Jr.. "Hypersonic Aerodynamic Performance of Minimum-Wave-Drag Bodies," NASA TR R 250, 1966

2. Berman, R. J., "Ballistic Coefficients for Power Law Bodies," AIAA Journal, Vol. 5, No. 1, January 1967, pp. 334-338

3. Penland, Jim A., "A Study of the Stability and Location of the Center of Pressure on Sharp, Right Circular Cones at Hypersonic Speeds," NASA TN D-2283, 1964

4. Maddalon, Dal V., "Aerodynamic Characteristics of the Sharp Right Circular Cone at Mach 20.3 and Angles of Attack to 110° in Helium," NASA TN D-3201, 1966

5. Geineder, F., Schlesinger, M. I., Baum, G., and Cornett, R., "The U. S. Naval Ordnance Laboratory Hypersonic Tunnel," NOLTR 67-27, 1967

6. Risher, D. B., "Multiple Pressure Transducer Banks and Their Application," NOLTR 67-148, 1967

7. Willis, J. W., "Dare II Data Acquisition and Recording Equipment for the Naval Ordnance Laboratory's Hypersonic Tunnel No. 8," NOLTR 63-281, 1964

8. Wilson, D. M. and Fisher, P. D., "Measurements of Hypersonic Turbulent Heat Transfer on Cooled Cones. Proceedings of the 1966 Heat Transfer and Fluid Mechanics Institute," Michel A. Saed and James A. Miller, Editors, Stanford University Press, 1966, pp.236-252

9. Shantz, I., Gilbert, B. D. and White, C. E., "NOL Wind Tunnel Internal Strain Gage Balance System," NAVORD Report 2972, 1953

10. Conti, R. J., "Laminar Heat Transfer and Pressure Measurements at a Mach Number of 6 on Sharp and Blunt 15° Half-Angle Cones at Angles of Attack up to 90°," NASA TN D-962, 1961

11. Tracy, Richard R., "Hypersonic Flow Over a Yawed Circular Cone," GALCIT Hypersonic Research Project Memorandum No. 69, 1963

12. Peckham, D. H., "Experiments at Hypersonic Speeds on Circular Cones at Incidence," Aeronautical Research Council, C.P. 702, 1963

13. Avduevsky, V. S. and Medvedev, K. I., "Investigation of the Laminar Flow Separation on a Cone under Angle of Attack," Izvestia ANSSR, Fluid and Gas Mechanics, No. 3, 1966, pp. 117-119

14. Reshotko, Eli, "Laminar Boundary Layer with Heat Transfer on a Cone at Angle of Attack in a Supersonic Stream," NACA TN 4152, 1957

15. Reshotko, Eli and Beckwith, Ivan E., "Compressible Laminar Boundary Layer Over a Yawed Infinite Cylinder with Heat Transfer and Arbitrary Prandtl Number," NACA Report 1379, 1958

16. Wilson, R. E., "Laminar and Turbulent Boundary Layers on Slightly Blunted Cones at Hypersonic Speeds," NOLTR 66-54, 1966

17. Fitch, C. R., Morris, S. D., and Dunkin, O. L., "Force, Pressure, and Heat Transfer Tests on the GE Skybolt Nose Cone at Mach 10," AEDC-TDR-62-125, 1962

18. Wells, William R., and Armstrong, William O., "Tables of Aerodynamic Coefficients Obtained from Developed Newtonian Expression for Complete and Partial Conic and Spheric Bodies at Combined Angles of Attack and Sideslip with Some Comparisons with Hypersonic Experimental Data," NASA TR R-127, 1962

19. Penland, Jim A., "Effect of Body Nose Blunting, Control Planform Area, and Leading-Edge Bluntness on Aerodynamic Control of a 5°

Semivertex Angle Cone at Mach Number 6.9," NASA T ND-3460, 1960

20. Feldhuhn, Robert H., "An Experimental Investigation of the Effects of Tip Bluntness and Angle of Attack Upon the Static Stability of Cones at Mach Numbers 6 and 9," NOLTR 68-70

21. Truitt, Robert W., "Hypersonic Aerodynamics," The Ronald Press Company, 1959, p.85

22. Trimpi, Robert L. and Jones, Robert A., "Transient Temperature Distribution in a Two-Component Semi-Infinite Composite Slab of Arbitrary Materials Subjected to Aerodynamic Heating with a Discontinuous Change in Equilibrium Temperature of Heat Transfer Coefficient," NASA TN 4308, 1958

23. Schneider, P. J., "Conduction Heat Transfer," Addison Wesley, 1955, p. 250

24. Conti, R. J., "Approximate Temperature Distributions and Streamwise Heat Conduction Effects in the Transient Aerodynamic Heating of Thin-Skinned Bodies"

BLANK PAGE

MATERIAL: ARMCO 17-4 PH
STAINLESS STEEL

TIP RADIUS: 0.0313

5°

2.500

13.967

X
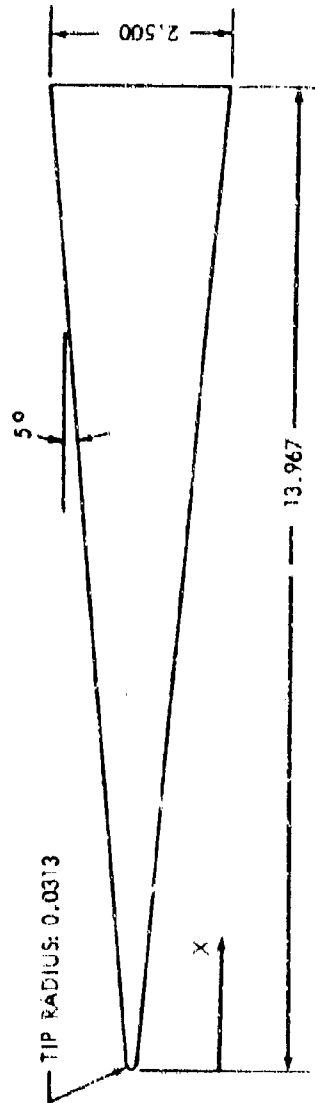
PRESSURE MODEL
WALL THICKNESS: 0.063
4 ALIGNMENT ORIFICES AT X = 4.00 AND 13.25

DISTANCE (X) FROM TIP TO PRESSURE ORIFICES:
1.00, 1.75, 2.50, 3.75, 4.00, 4.75, 5.50, 6.25, 7.00,
7.75, 8.50, 9.25, 10.00, 10.75, 11.50, 12.25, 13.25

DISTANCE (X) FROM TIP TO THERMOCOUPLE JUNCTIONS:
1.00, 1.75, 2.50, 3.25, 4.00, 6.25, 7.75, 9.25, 10.75

HEAT TRANSFER MODEL
WALL THICKNESS: 0.020
4 ALIGNMENT ORIFICES X = 13.27

NOTE: ALL LENGTH DIMENSIONS ARE IN INCHES

FIG. 1 SLIGHTLY BLUNTED CONICAL PRESSURE AND HEAT TRANSFER MODELS

NOSE RADIUS: 0.0313

2.500

5°

13.967

X
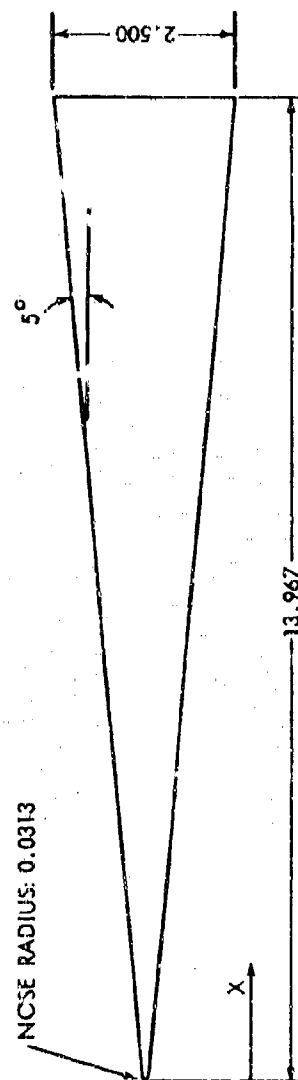
REFERENCE AREA: A_b = 4.91 SQUARE INCHES

REFERENCE LENGTH: L = 13.967 INCHES

NOTE: ALL LENGTH DIMENSIONS ARE IN INCHES

FIG. 2 SLIGHTLY BLUNTED CONICAL FORCE MODEL - CONFIGURATION 6FN

DETAIL "A"

$(Z - X) = 0.030$
$R_n = 0.0313$
FOR $X > 0.020$
$Y = 0.2146 Z^{2/3}$

FOR SKETCH
OF NOSE TIP
SEE DETAIL "A"

$Y = 0.2146 Z^{2/3}$

2.500

14.027

REFERENCE AREA: $A_b = 4.91$ SQUARE INCHES
REFERENCE LENGTH: L = 14.027 INCHES
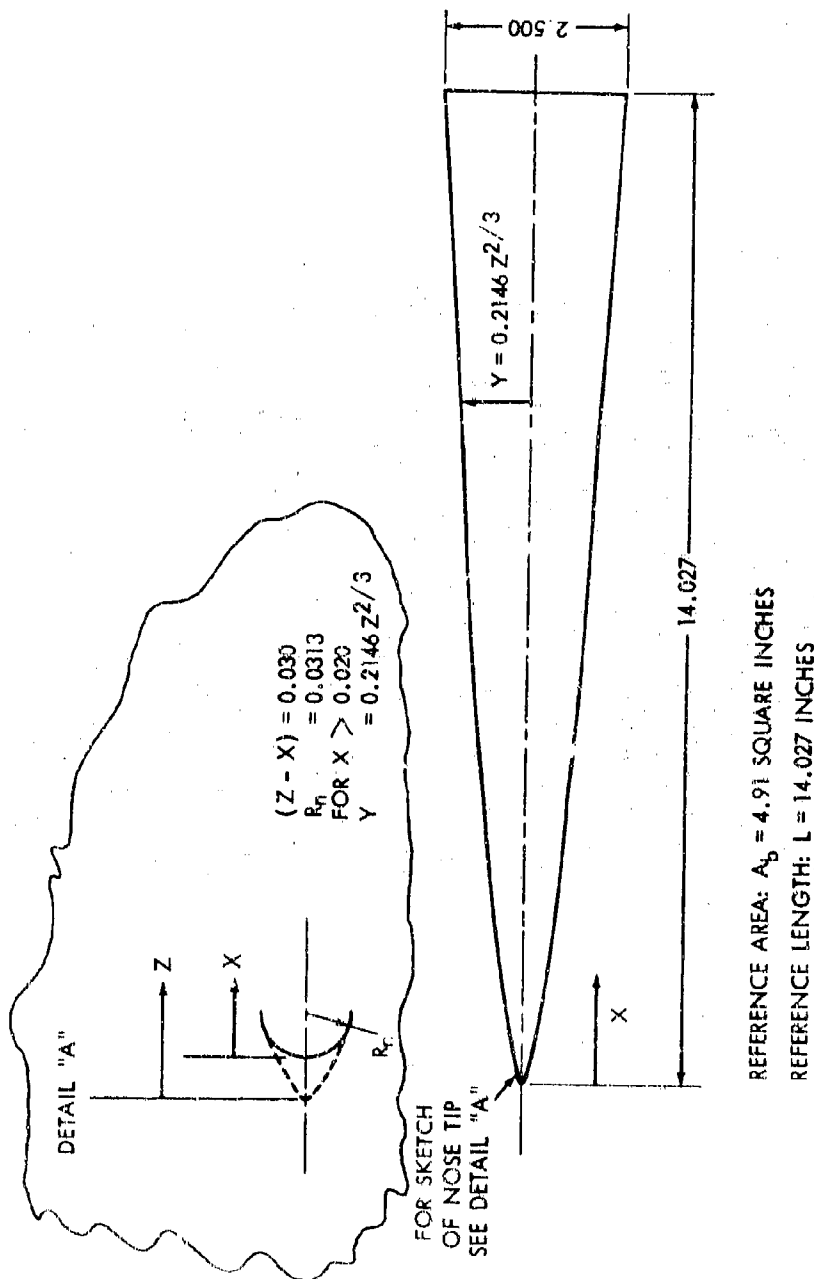
NOTE: ALL LENGTH DIMENSIONS ARE IN INCHES

FIG. 3   SLIGHTLY BLUNTED 2/3 POWER LAW BODY OF REVOLUTION-CONFIGURATION 6FX-1
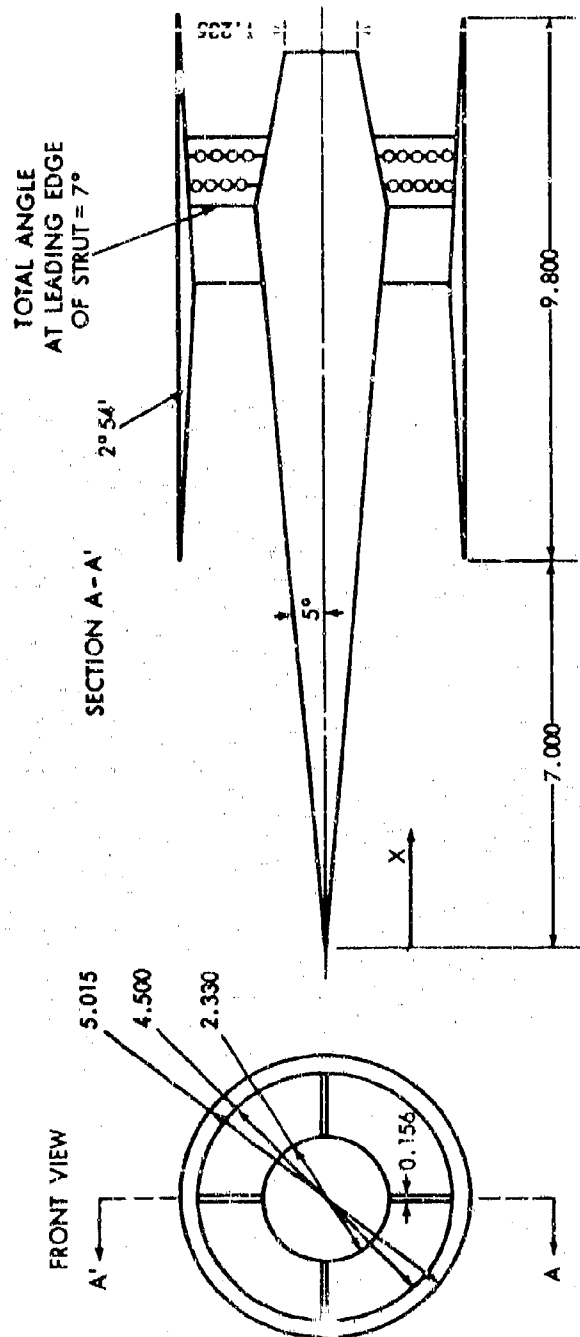
TOTAL ANGLE
AT LEADING EDGE
OF STRUT = 7°

2° 54'

SECTION A-A'

5°

1.235

9.800

7.000

X

FRONT VIEW

5.015
4.500
2.330

0.156

A'

A

REFERENCE AREA: A_b = 4.26 SQUARE INCHES
REFERENCE LENGTH: L = 16.800 INCHES

NOTE: ALL LENGTH DIMENSIONS ARE IN INCHES

FIG. 4 DUCTED CONE - CONFIGURATION 6FX-2-1
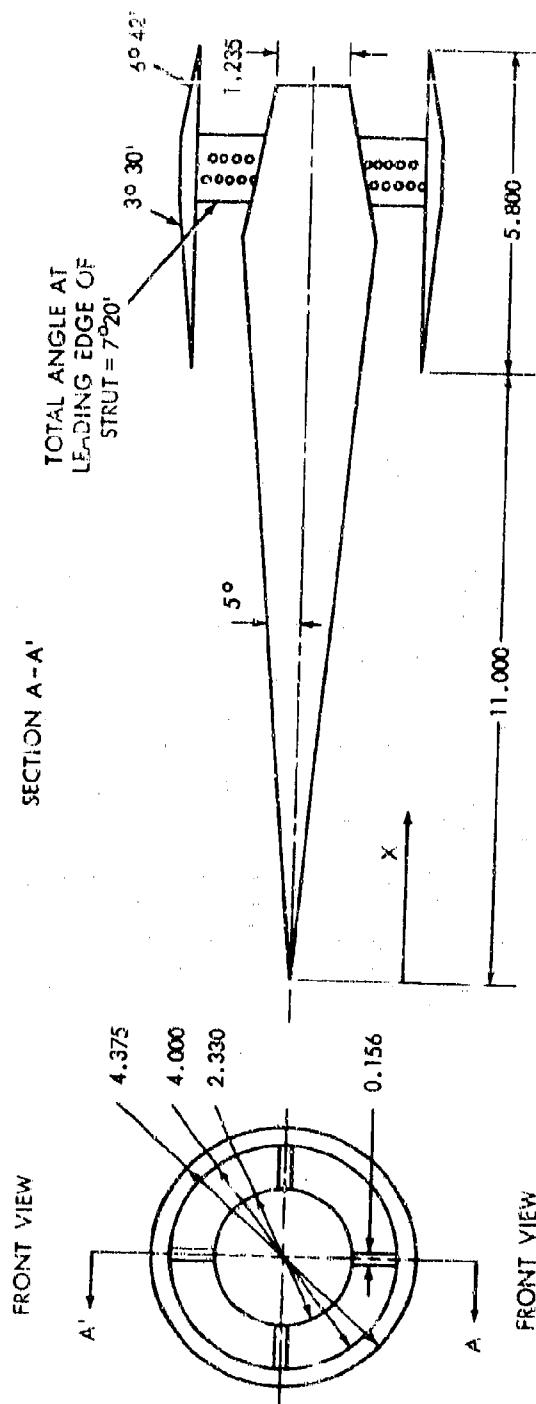
SECTION A-A'

TOTAL ANGLE AT
LEADING EDGE OF
STRUT = 7°20'

5° 42'

1.235

3° 30'

5°

11.000

5.800

X

FRONT VIEW

4.375

4.000

2.330

0.156

A'

A

FRONT VIEW

REFERENCE AREA: A_b = 4.26 SQUARE INCHES

REFERENCE LENGTH: L = 16.800 INCHES

NOTE: ALL LENGTH DIMENSIONS ARE IN INCHES

FIG. 5 DUCTED CONE - CONFIGURATION 6FX-2-2

SYMBOL	M_∞	Re_∞/FT
□	5.93	2.38×10^6
O	6.00	22.6×10^6
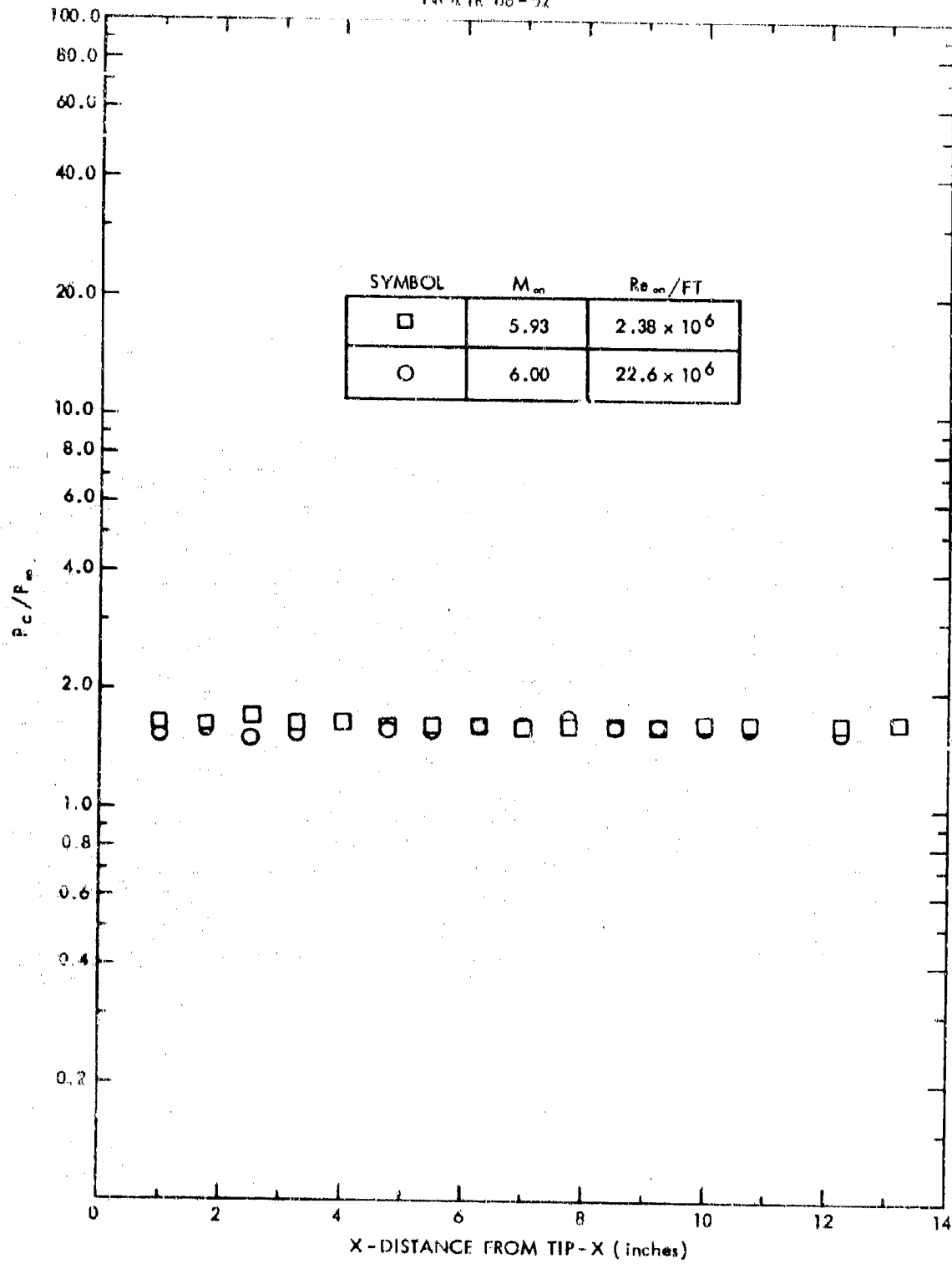
FIG. 6 SURFACE PRESSURE DISTRIBUTION - α $0°$
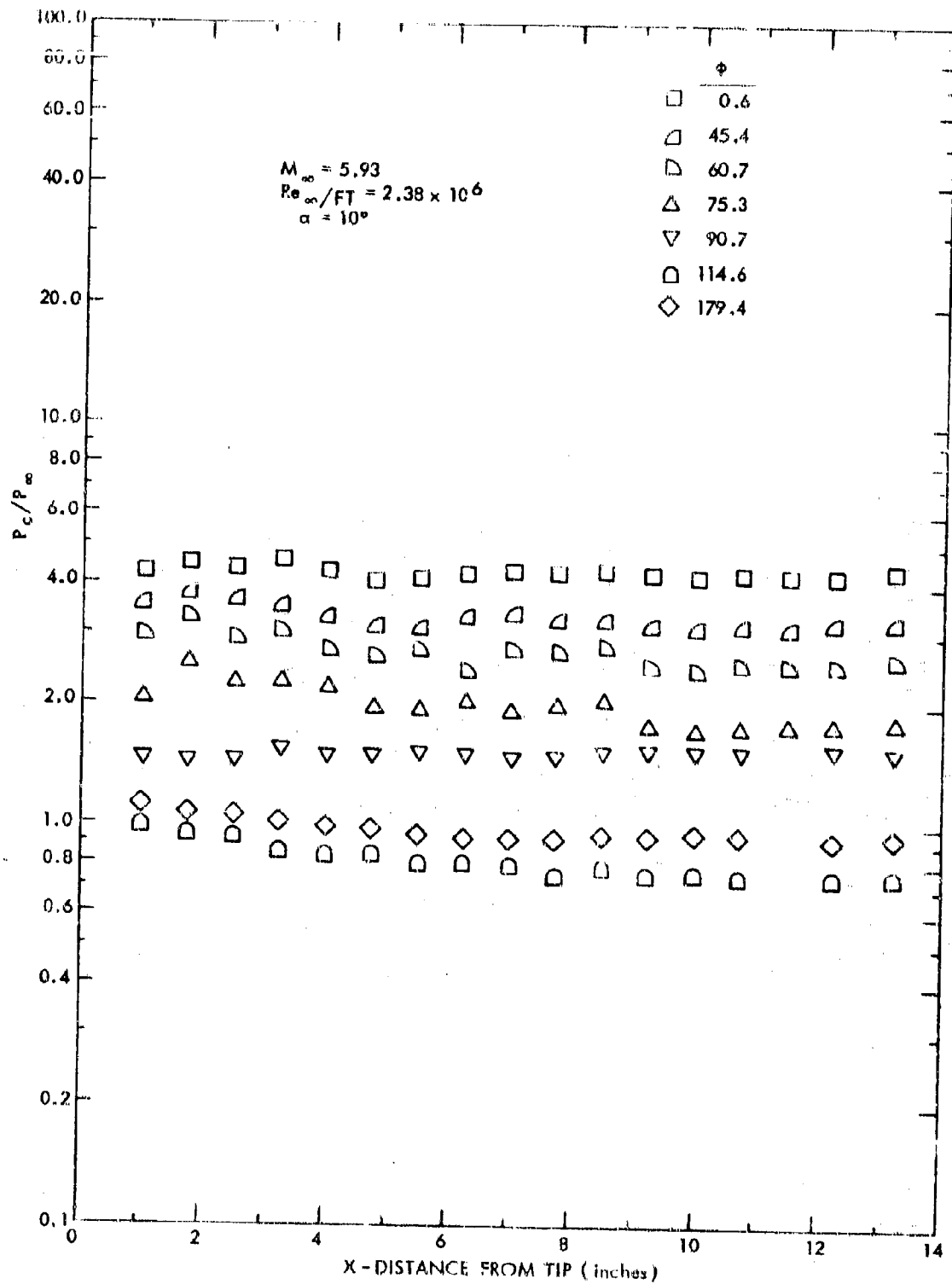
FIG. 7 SURFACE PRESSURE DISTRIBUTION- α = 10°
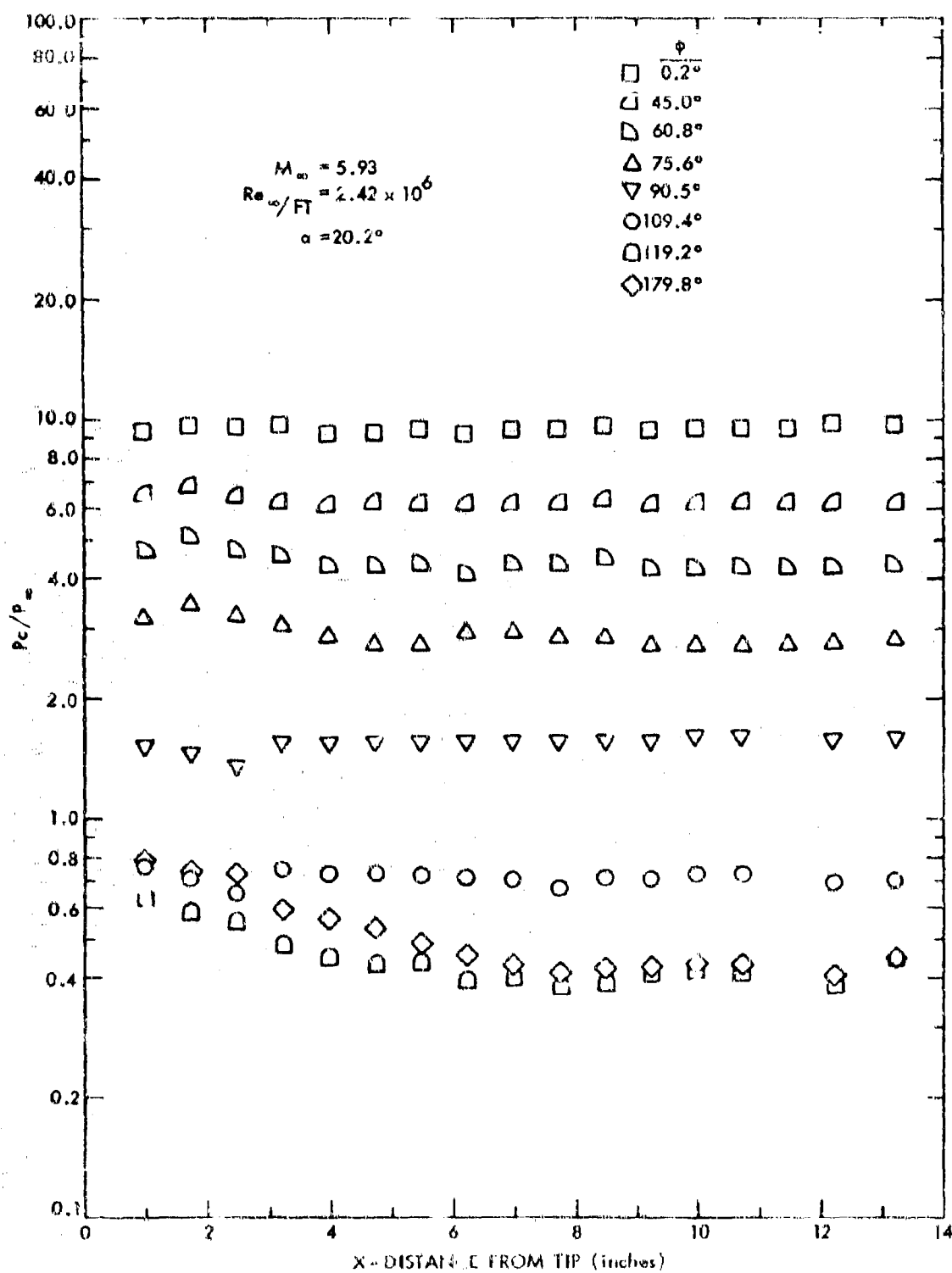
FIG. 8 SURFACE PRESSURE DISTRIBUTION — α = 20.2°
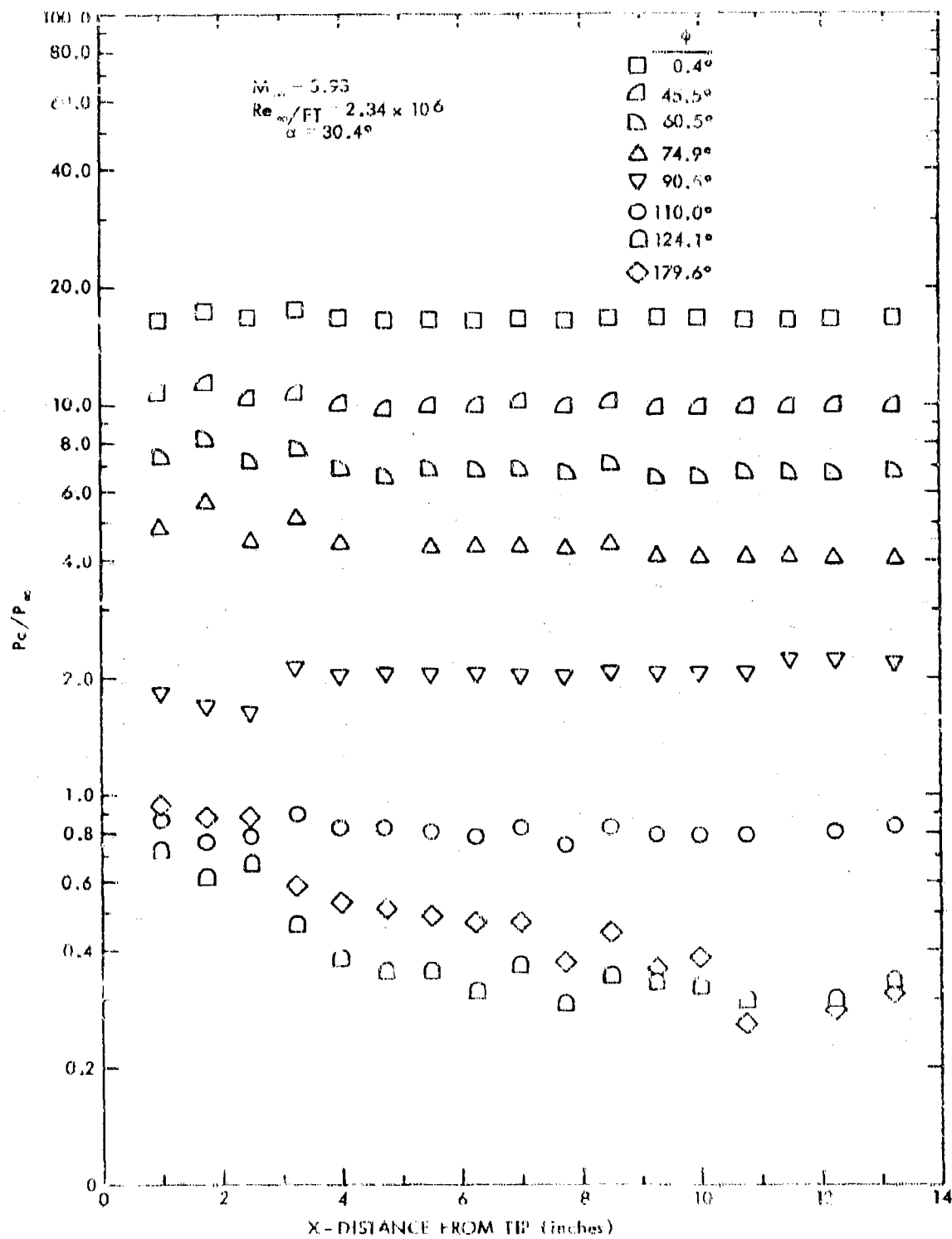
FIG. 9 SURFACE PRESSURE DISTRIBUTION α = 30.4°
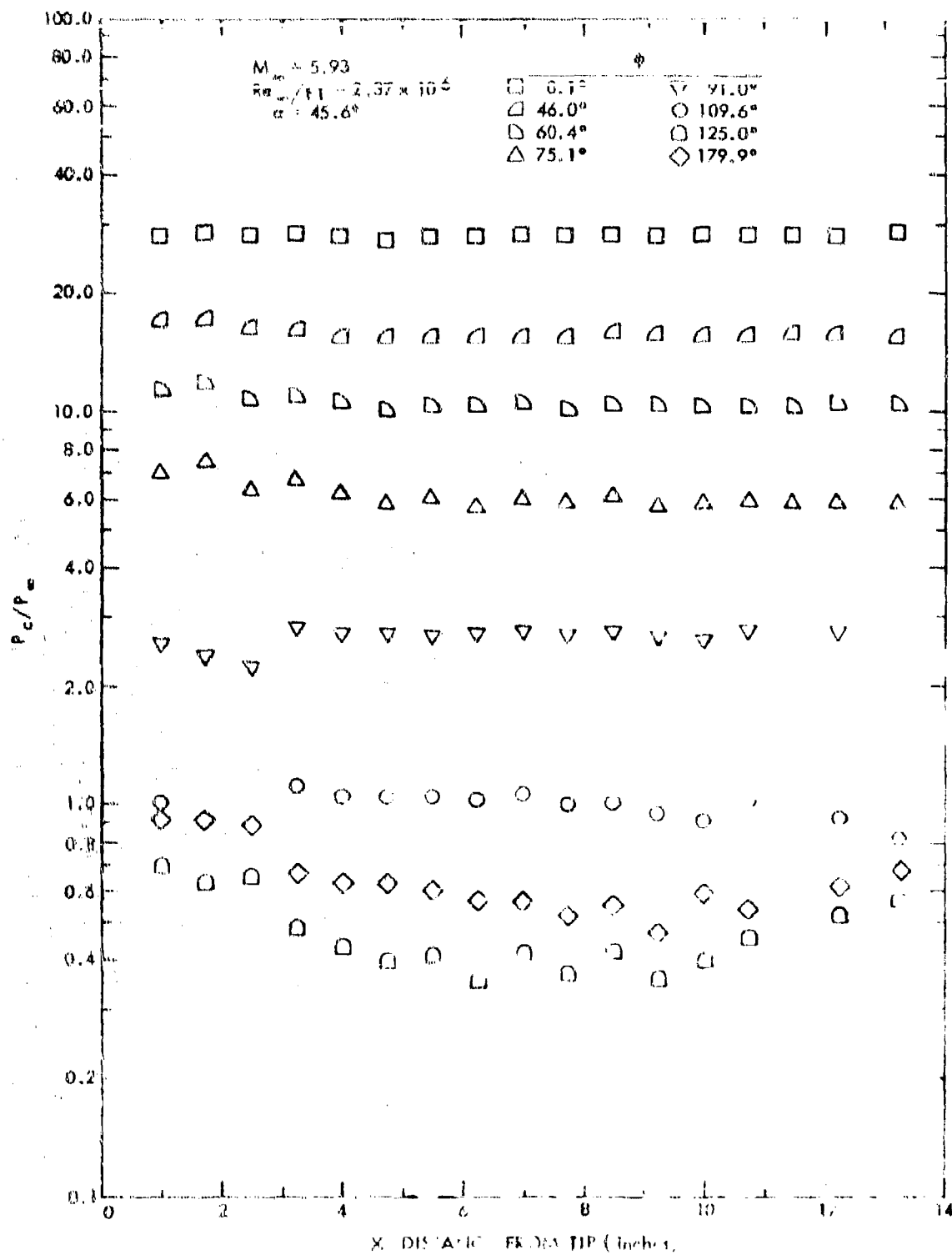
FIG. 10 SURFACE PRESSURE DISTRIBUTION α = 45.6°
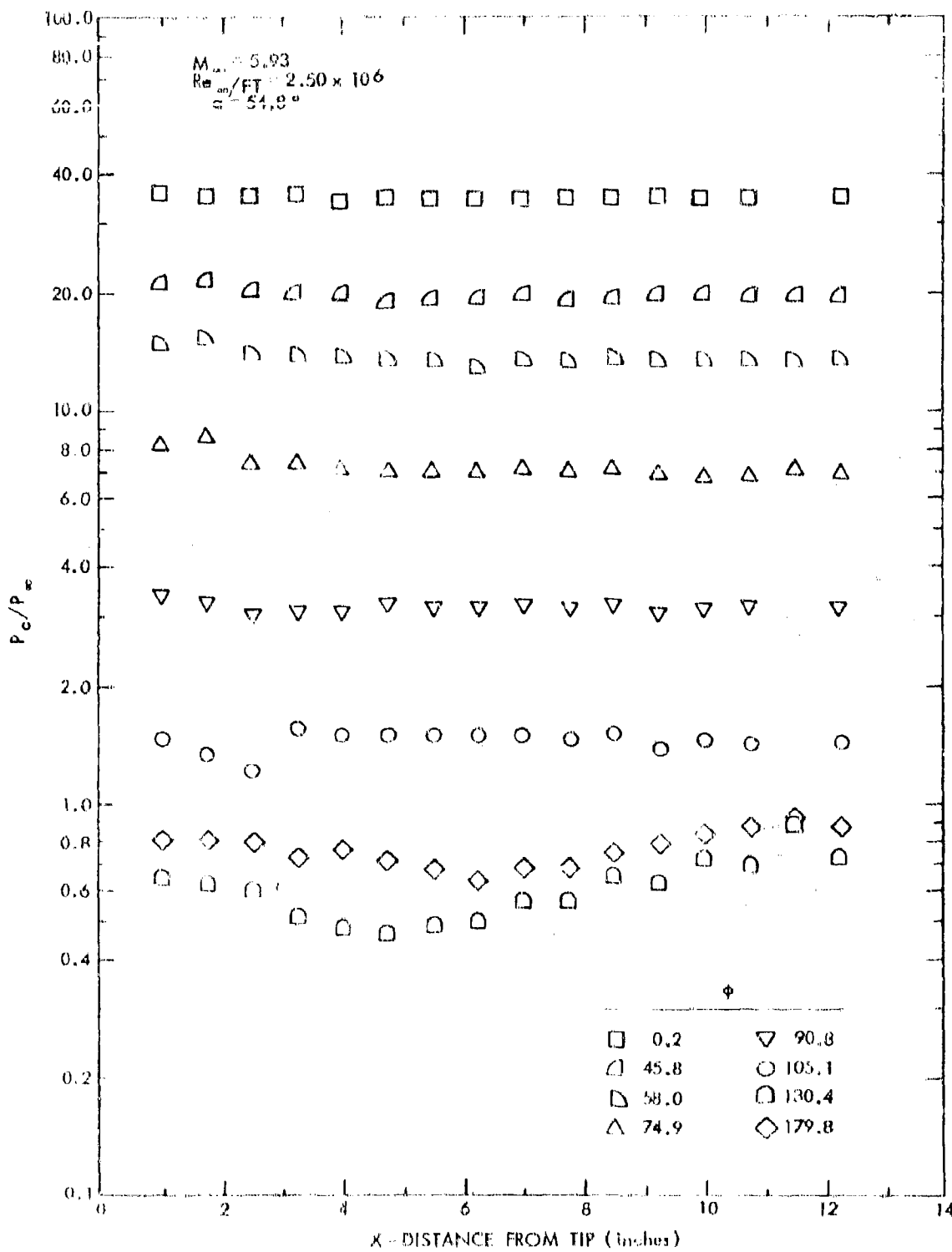
FIG. 11 SURFACE PRESSURE DISTRIBUTION—α 54.8°
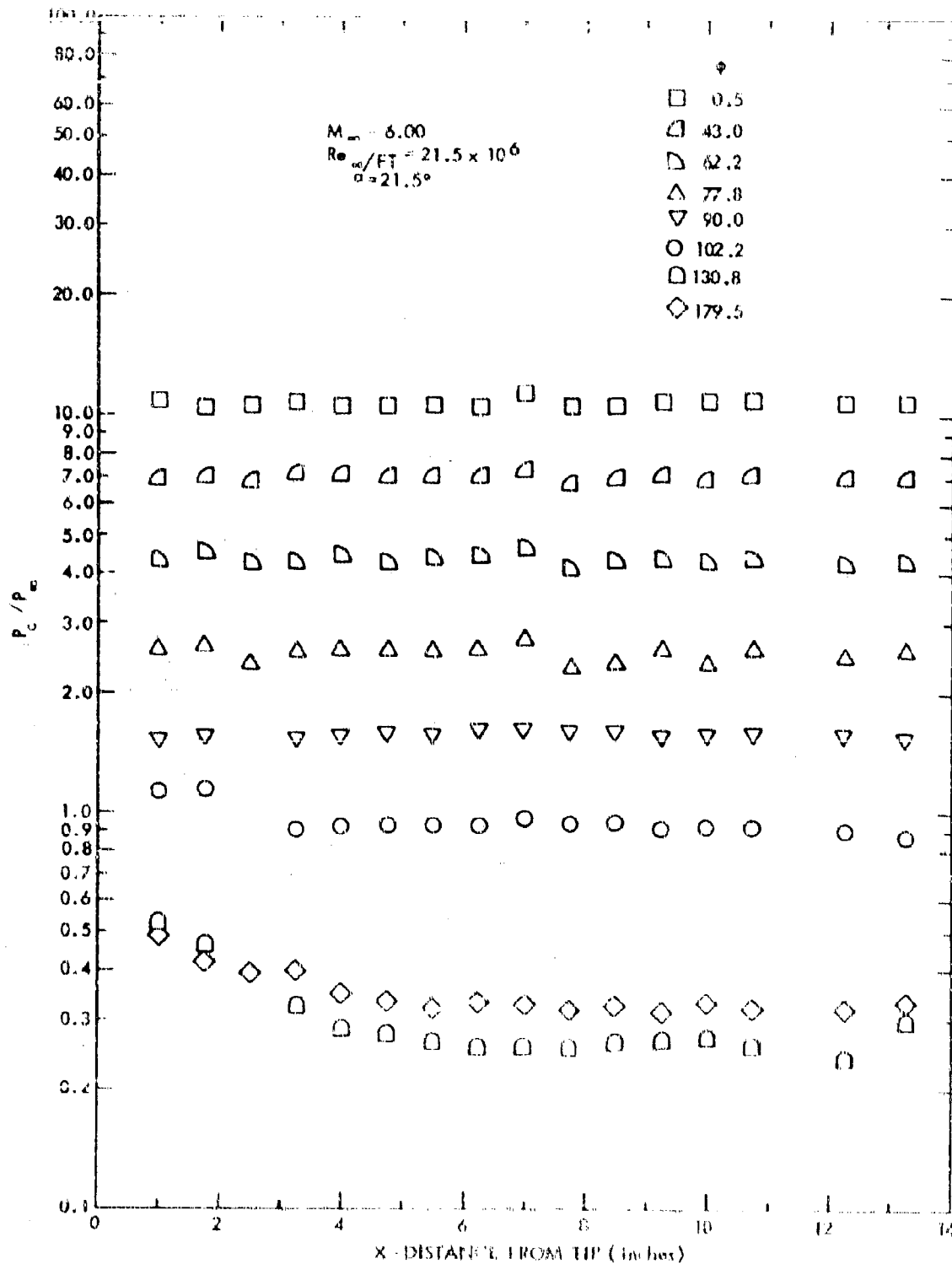
FIG. 12 SURFACE PRESSURE DISTRIBUTION α = 21.5°
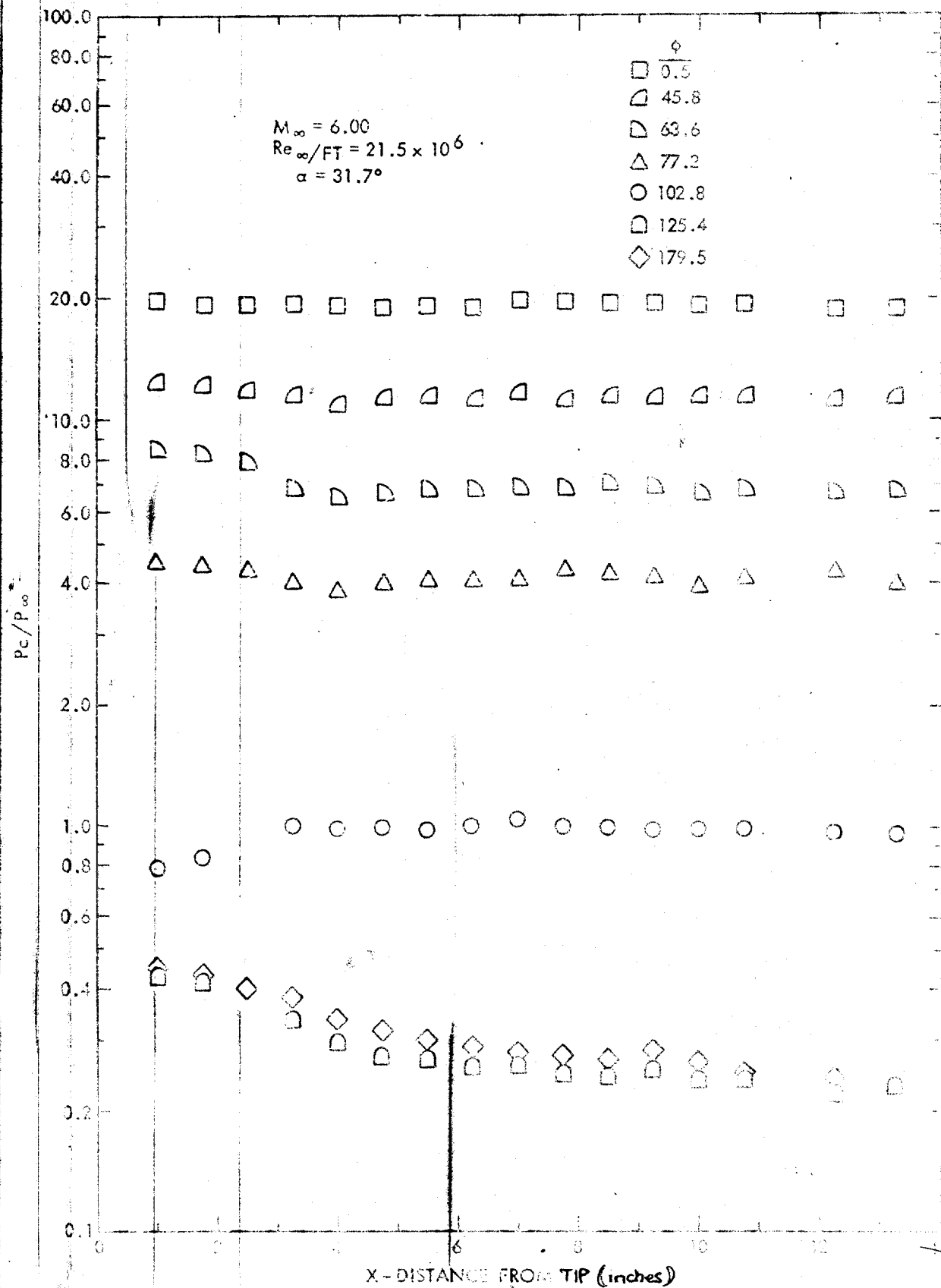
FIG. 13 SURFACE PRESSURE DISTRIBUTION - α = 31.7°
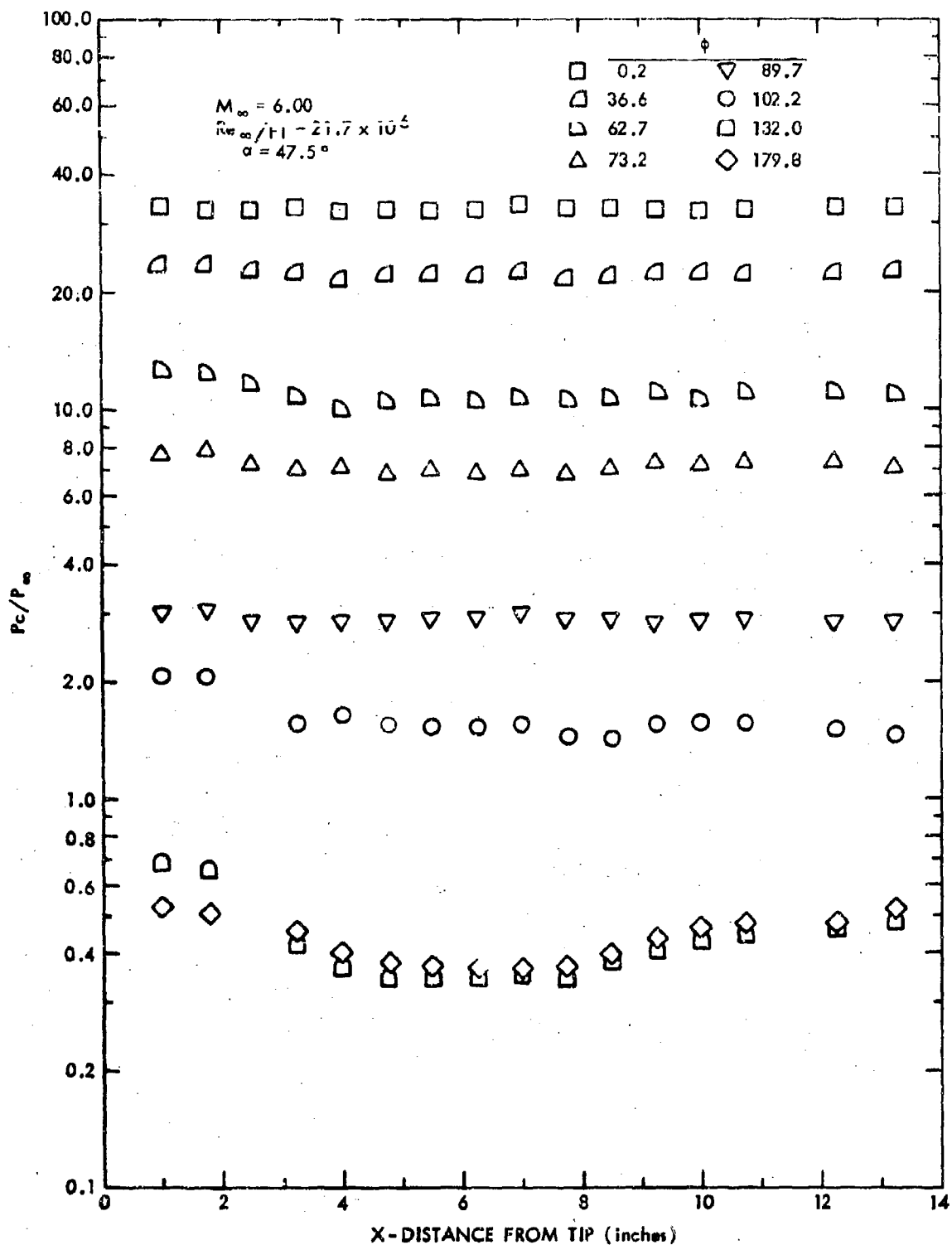
FIG. 14 SURFACE PRESSURE DISTRIBUTION - α = 47.5°
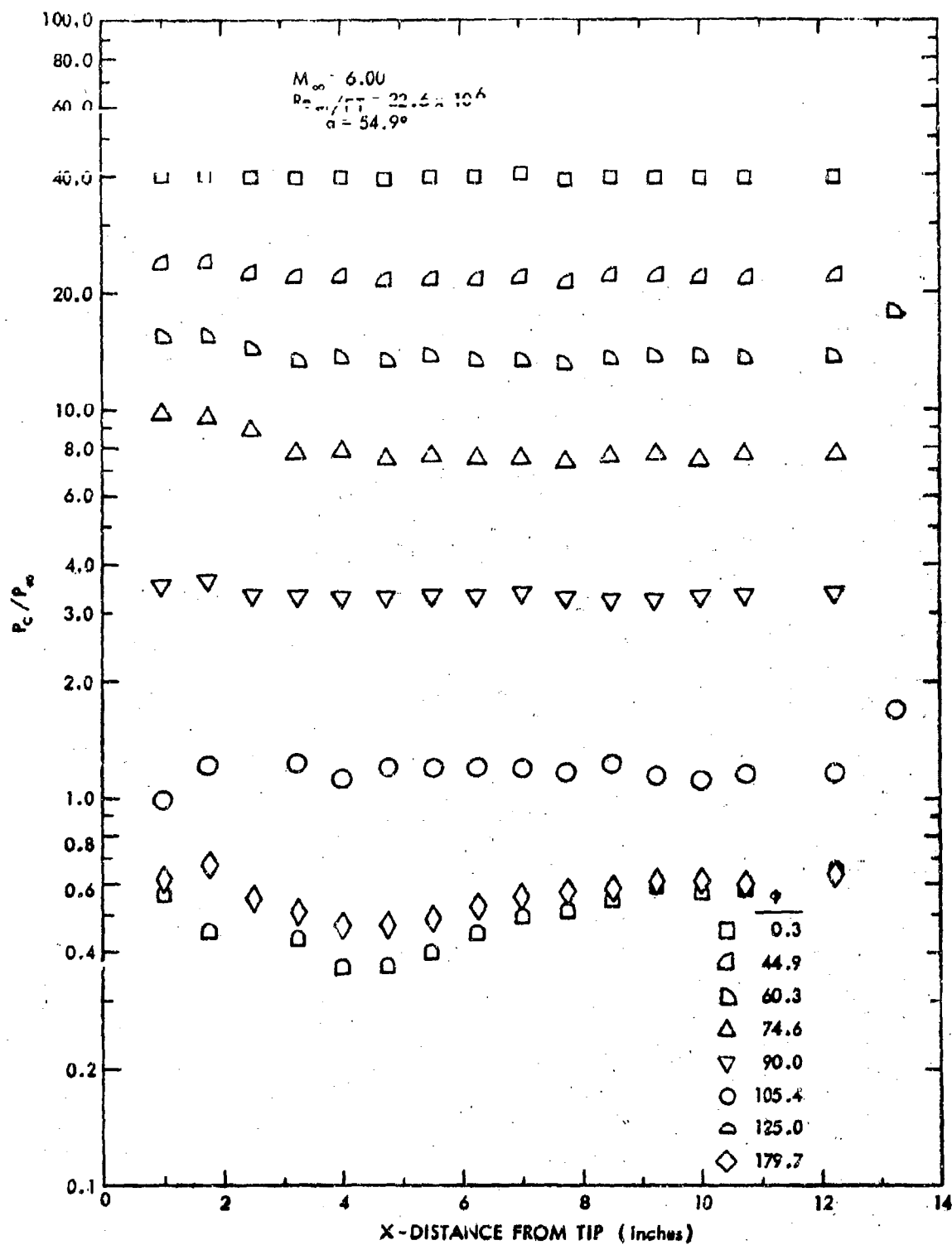
FIG. 15 SURFACE PRESSURE DISTRIBUTION - a= 54.9°
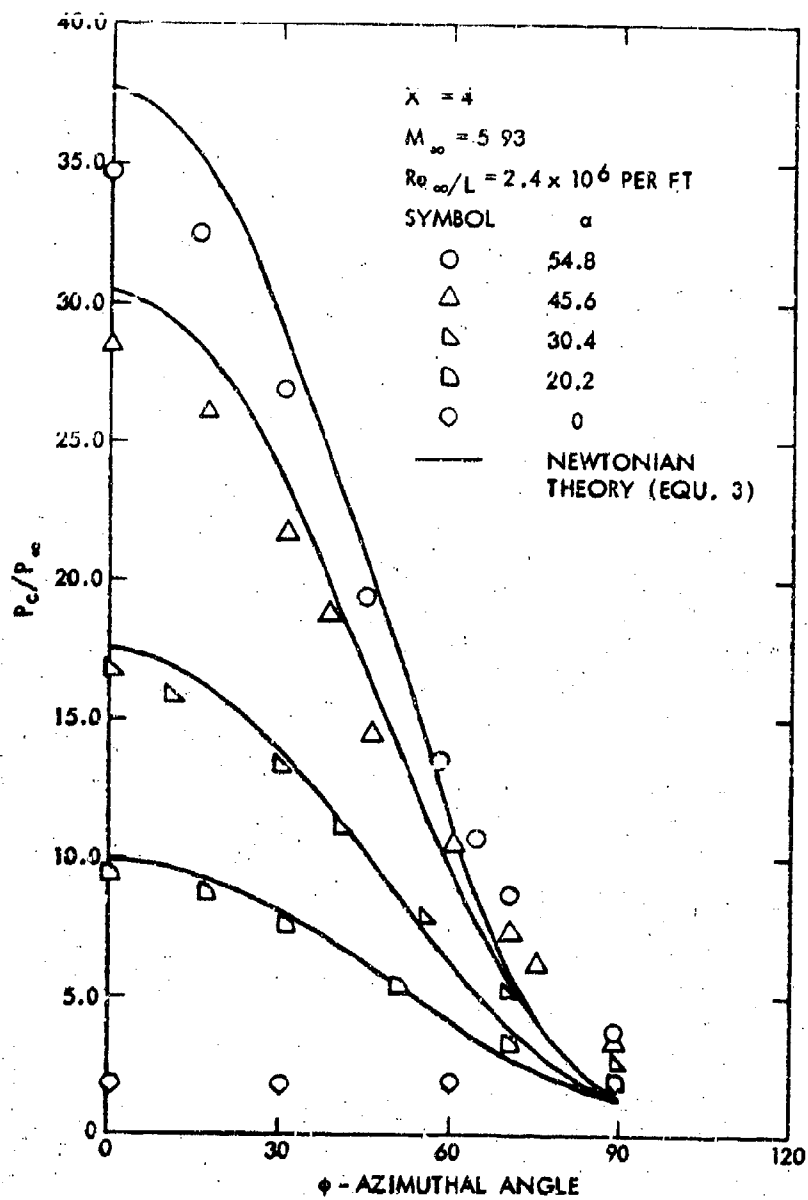
FIG. 16 CIRCUMFERENTIAL PRESSURE DISTRIBUTION
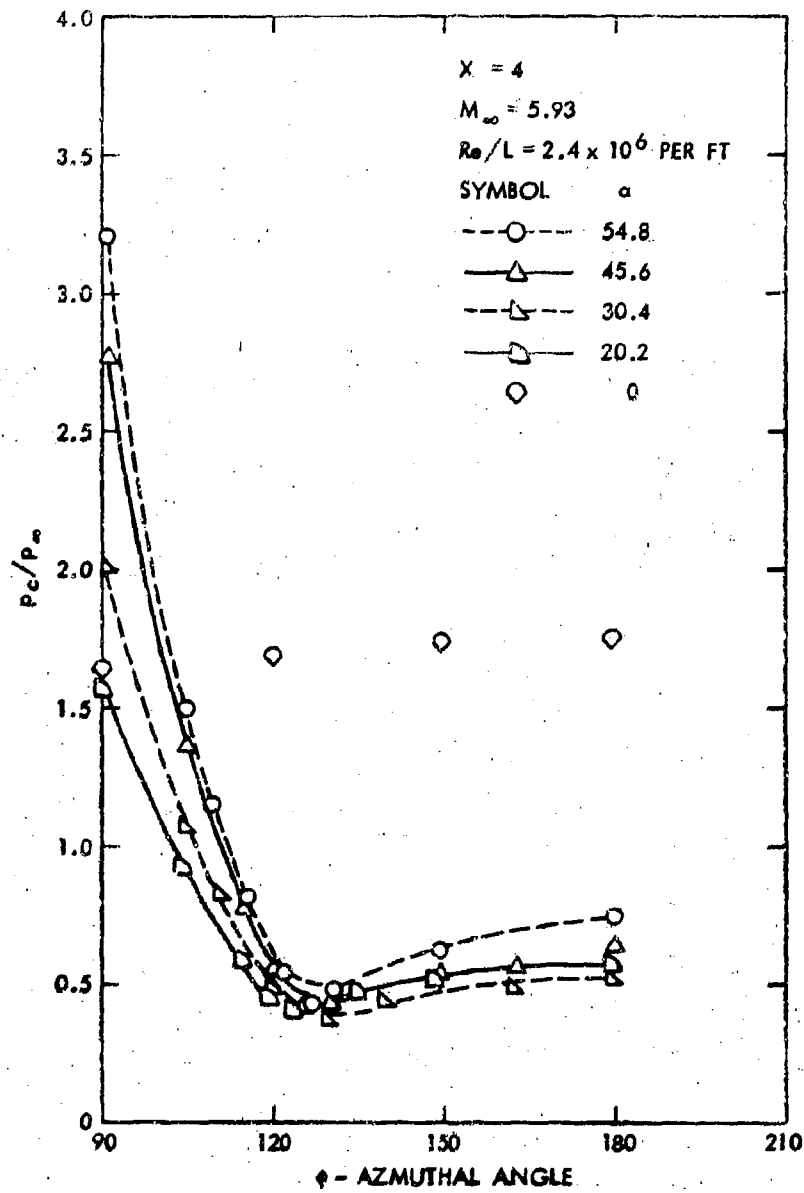
FIG. 17 CIRCUMFERENTIAL PRESSURE DISTRIBUTION
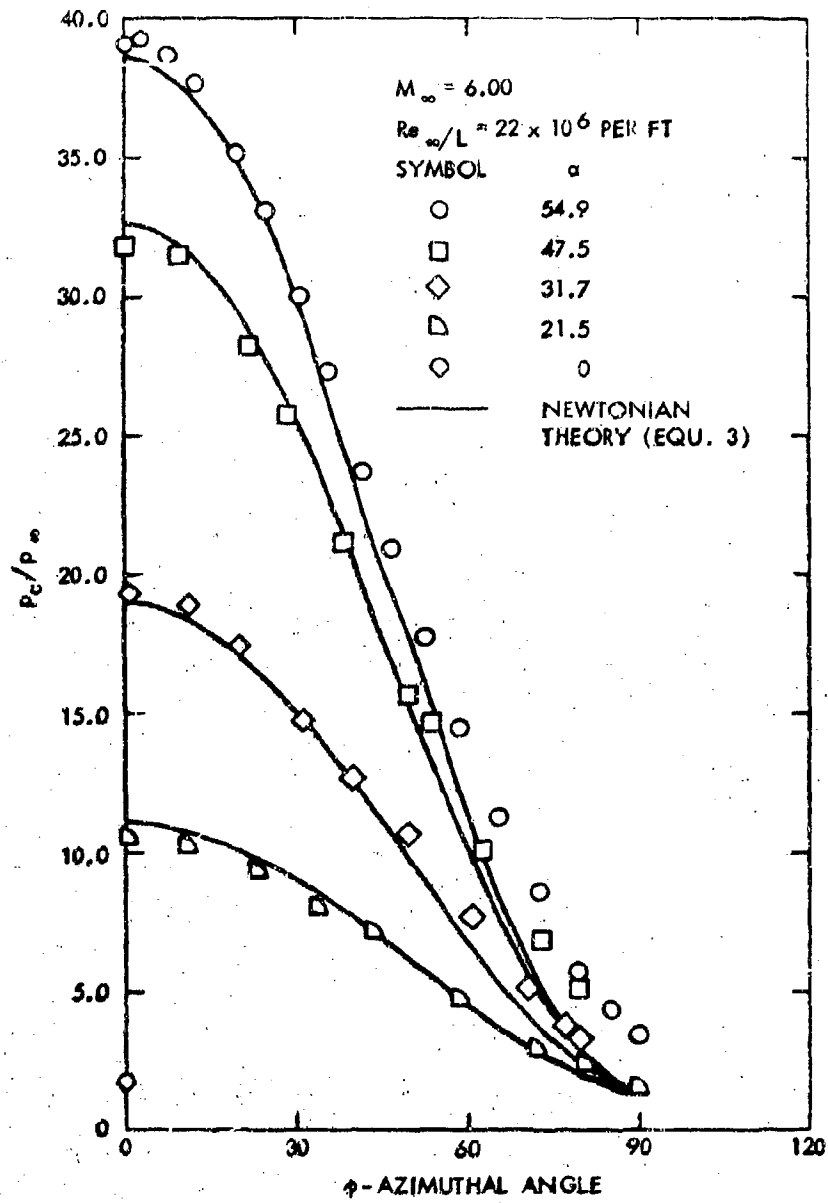
FIG. 18 CIRCUMFERENTIAL PRESSURE DISTRIBUTION
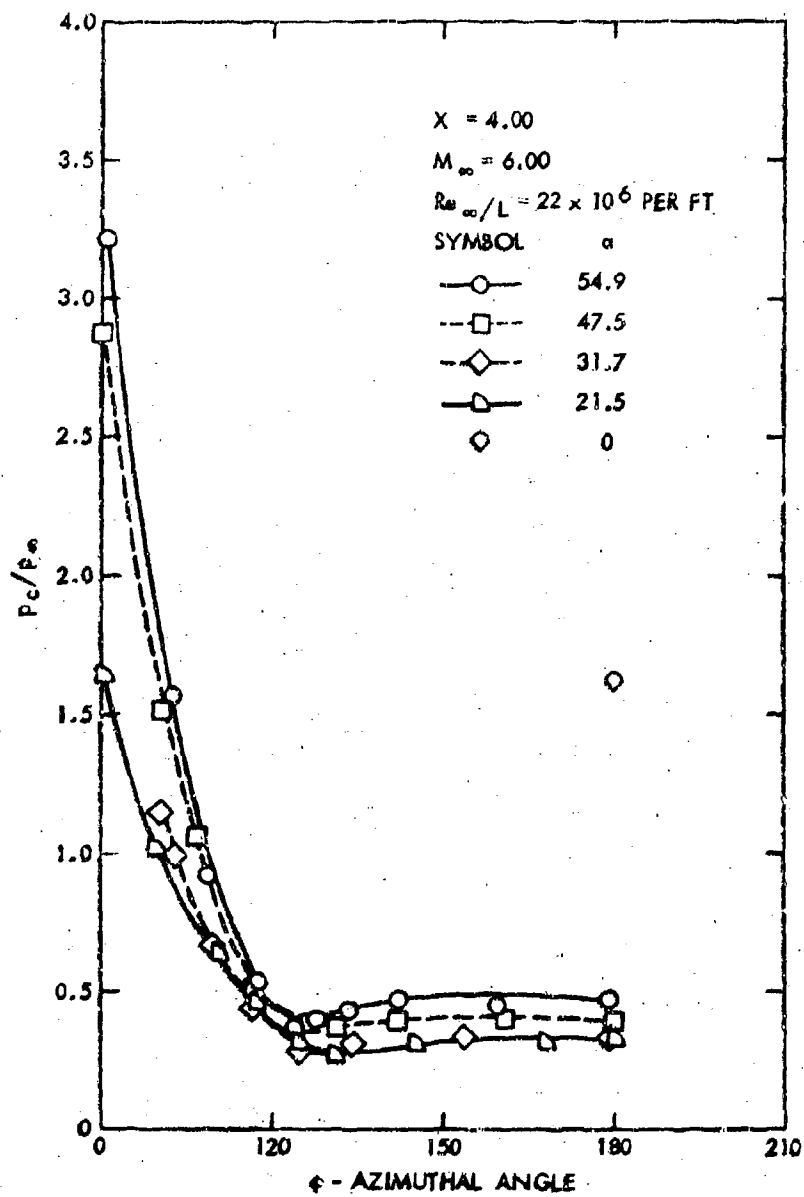
FIG. 19 CIRCUMFERENTIAL PRESSURE DISTRIBUTION
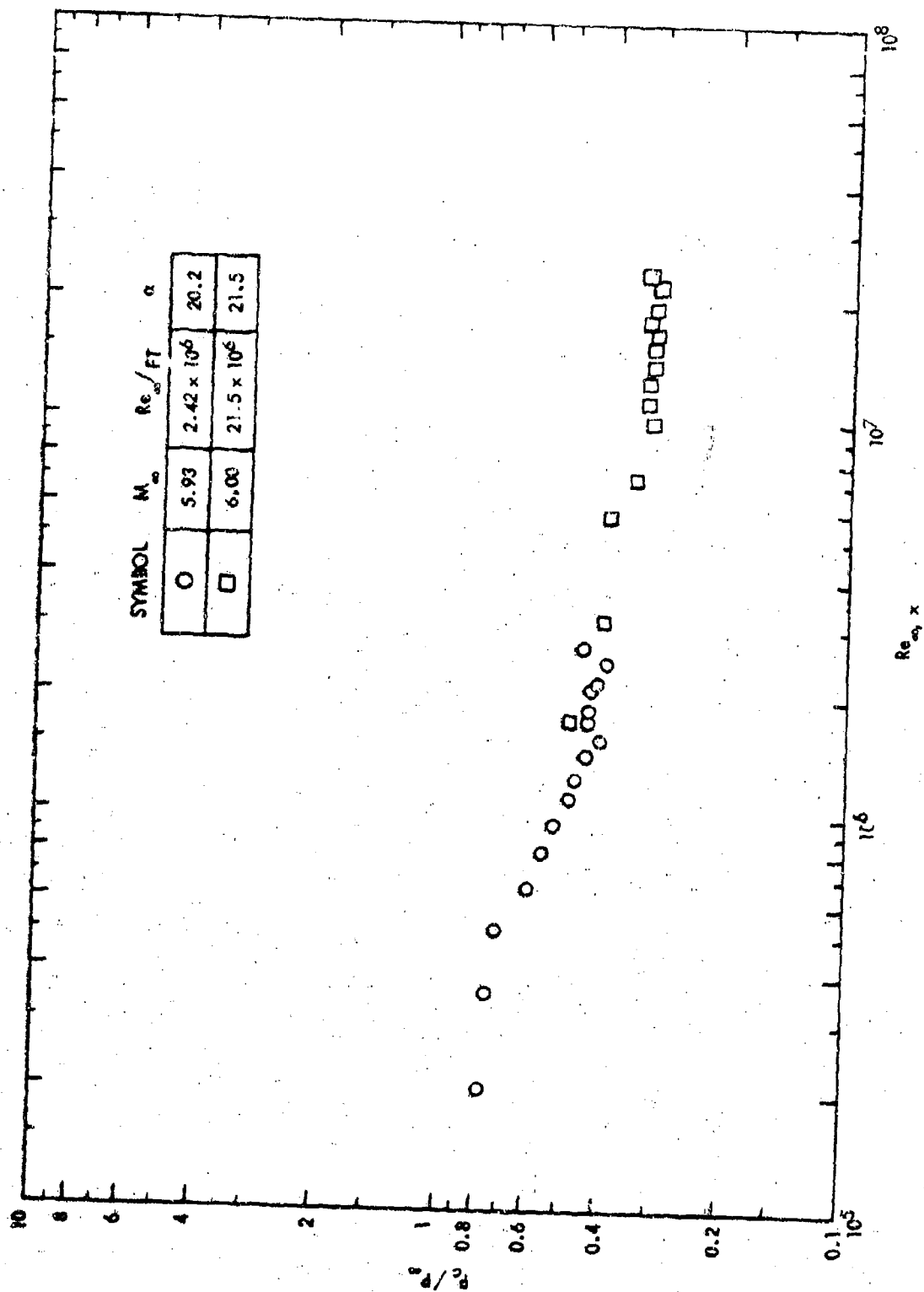
FIG. 20 STATIC PRESSURE VARIATION ALONG THE MOST LEEWARD MERIDIAN PLANE - α = 20°
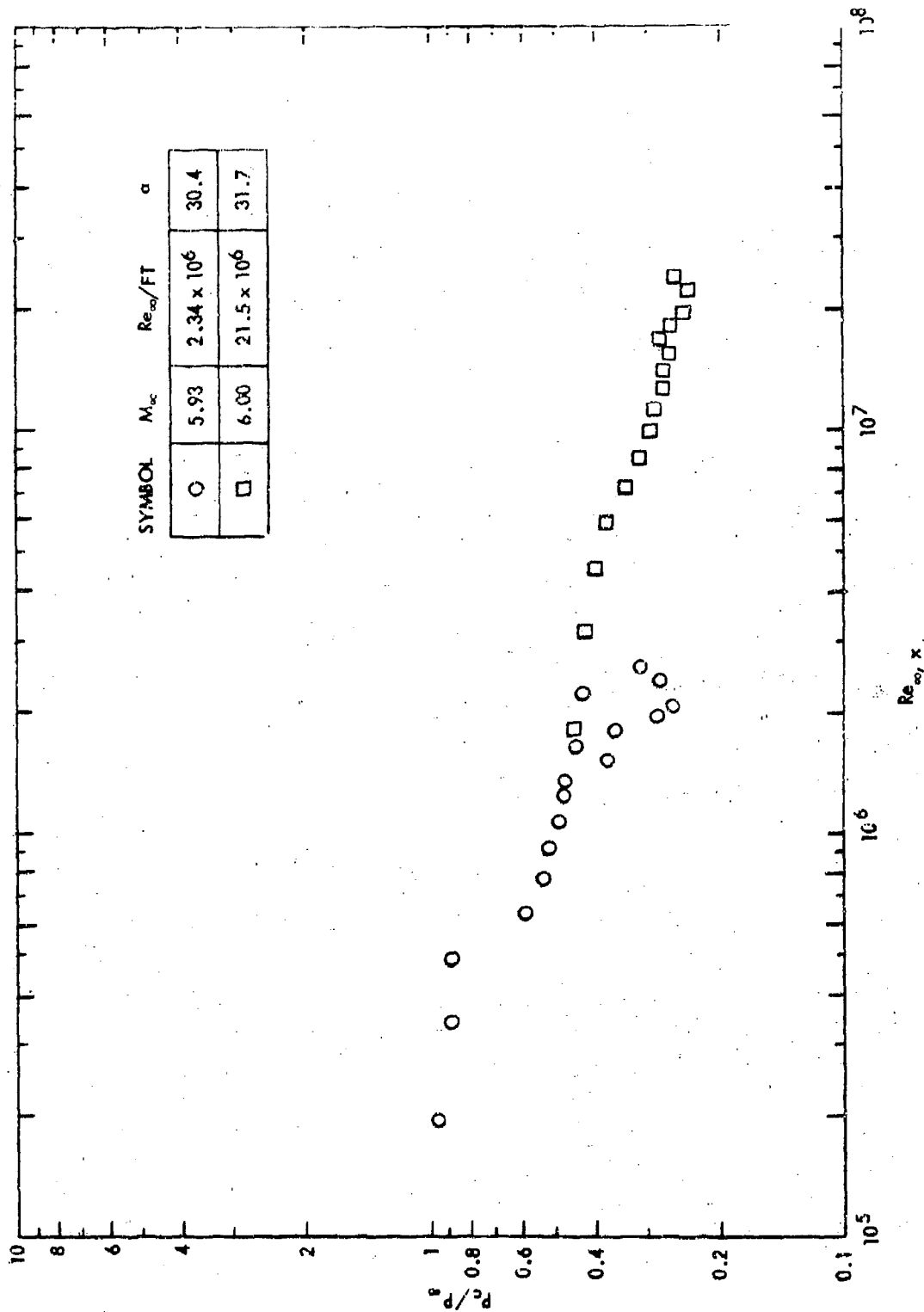
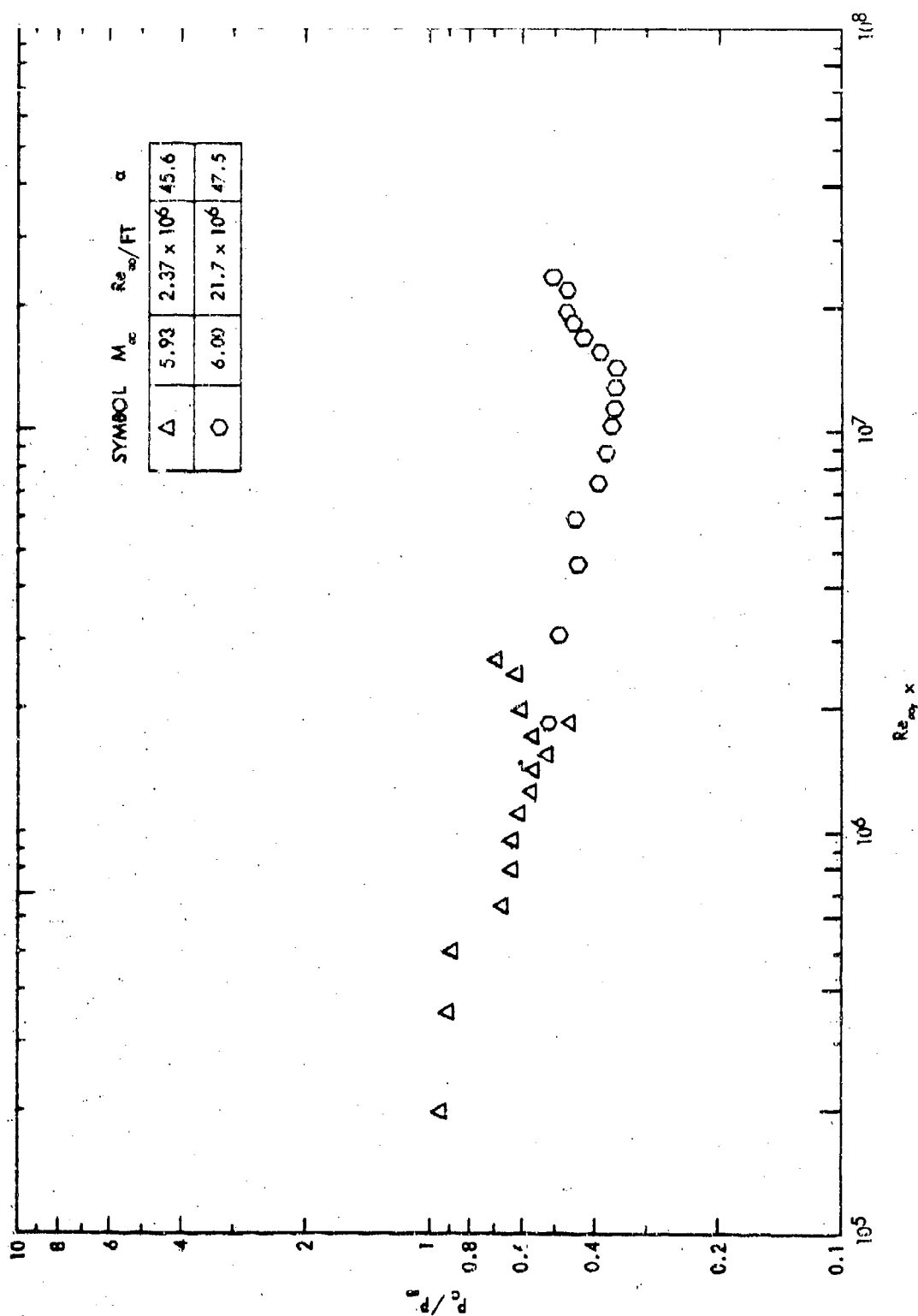FIG. 21 STATIC PRESSURE VARIATION ALONG THE MOST LEEWARD MERIDIAN PLANE $\alpha = 30°$

SYMBOL	M_∞	Re_∞/FT	α
○	5.93	2.34×10^6	30.4
□	6.00	21.5×10^6	31.7

FIG. 22 STATIC PRESSURE VARIATION ALONG THE MOST LEEWARD MERIDIAN PLANE - α = 45°

TARE

SIDE VIEW

WINDWARD VIEW

LEEWARD VIEW

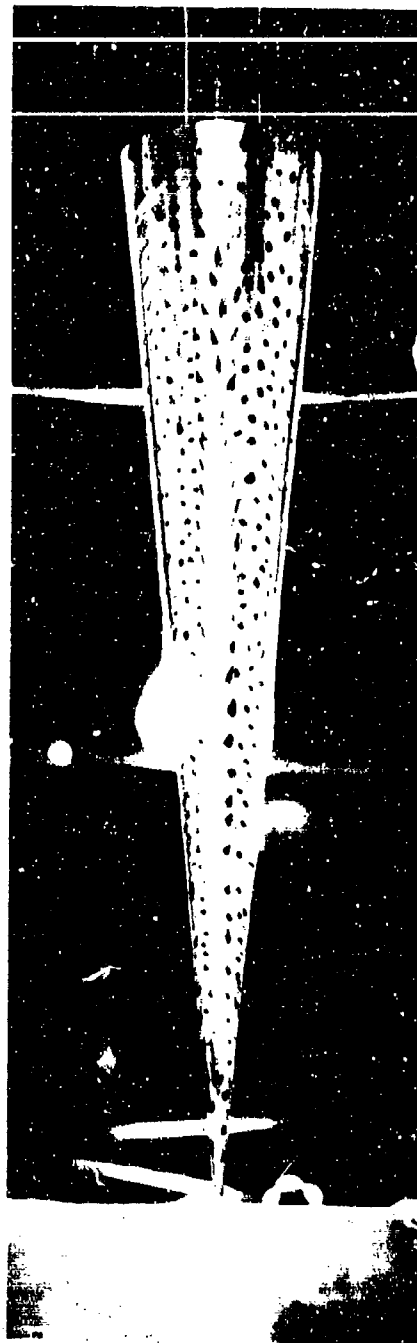FIG. 23 SURFACE OIL FLOW PATTERNS ON AN INCLINED CONE - a = 15°

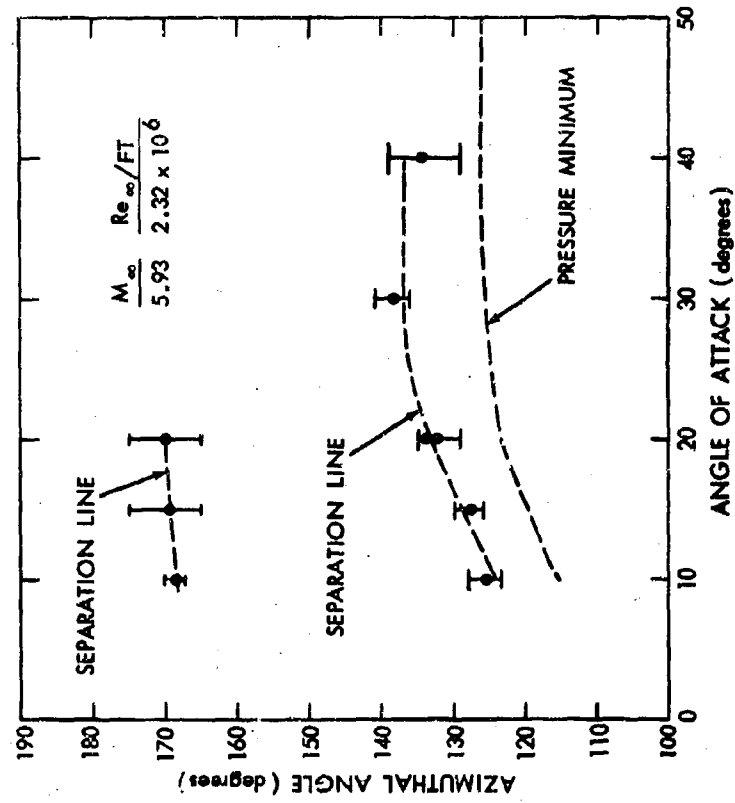FIG. 24 SURFACE OIL FLOW PATTERN LEEWARD SURFACE – $\alpha = 15°$

FIG. 25 SEPARATION MEASUREMENTS

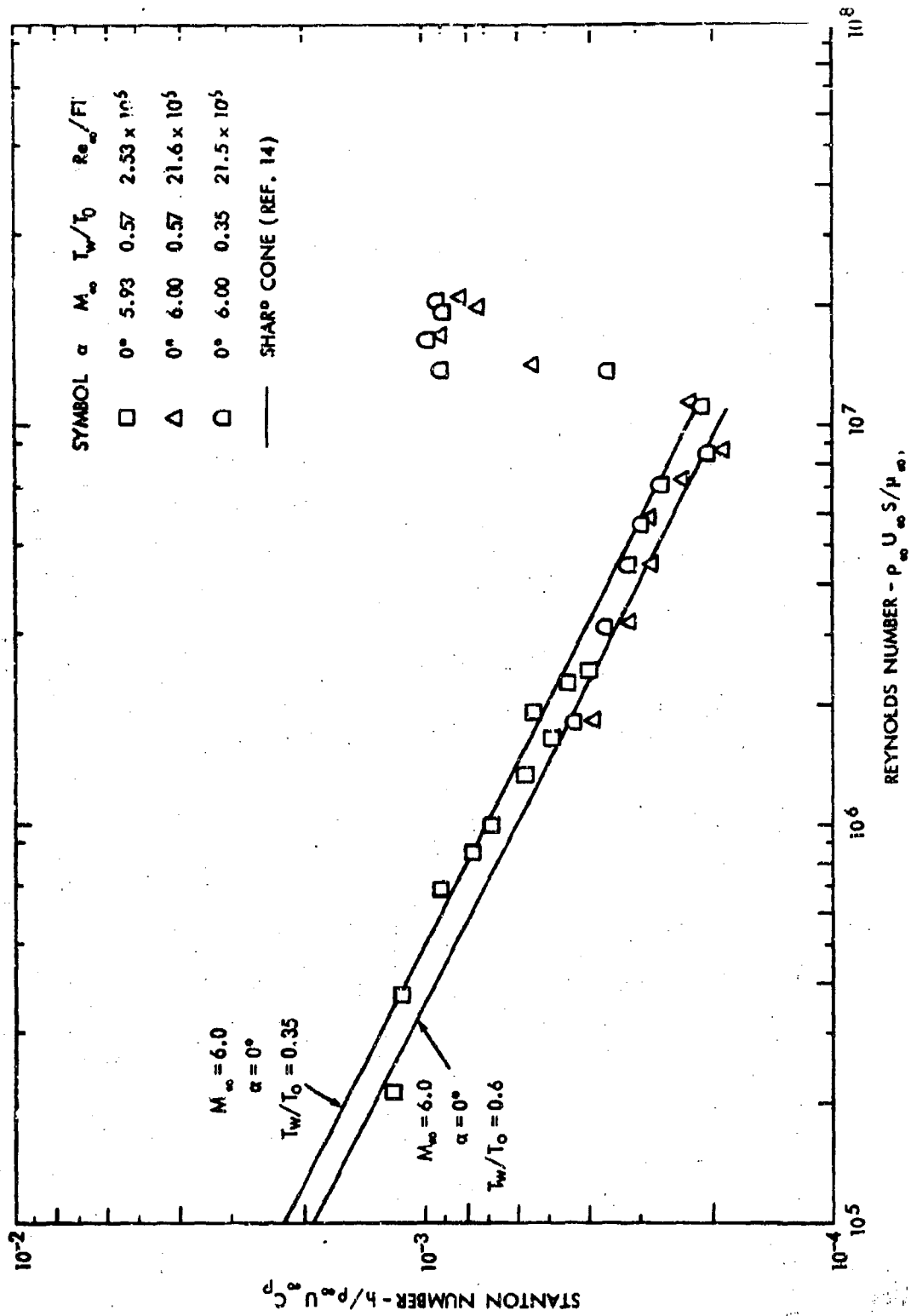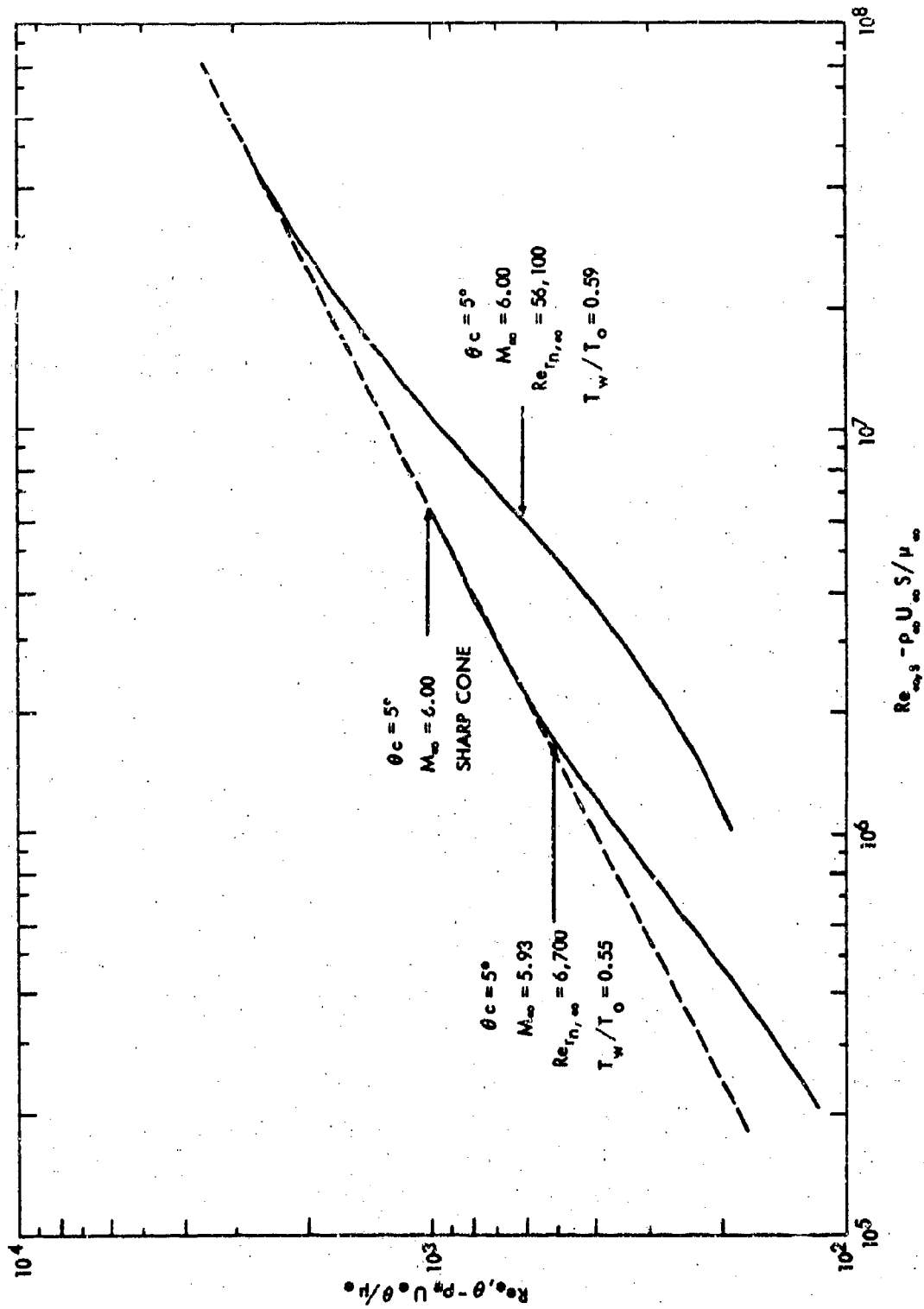FIG. 26 ZERO ANGLE OF ATTACK HEAT TRANSFER DISTRIBUTION

$$Re_{\infty,s} = \rho_\infty U_\infty S / \mu_\infty$$

$$Re_{e,\theta} = \rho_e U_e \theta / \mu_e$$

$\theta c = 5°$
$M_\infty = 6.00$
$Re_{r_{n,\infty}} = 56,100$
$T_w / T_o = 0.59$

$\theta c = 5°$
$M_\infty = 6.00$
SHARP CONE

$\theta c = 5°$
$M_\infty = 5.93$
$Re_{r_{n,\infty}} = 6,700$
$T_w / T_o = 0.55$

FIG. 27 EFFECT OF BLUNTNESS ON MOMENTUM THICKNESS REYNOLDS NUMBER
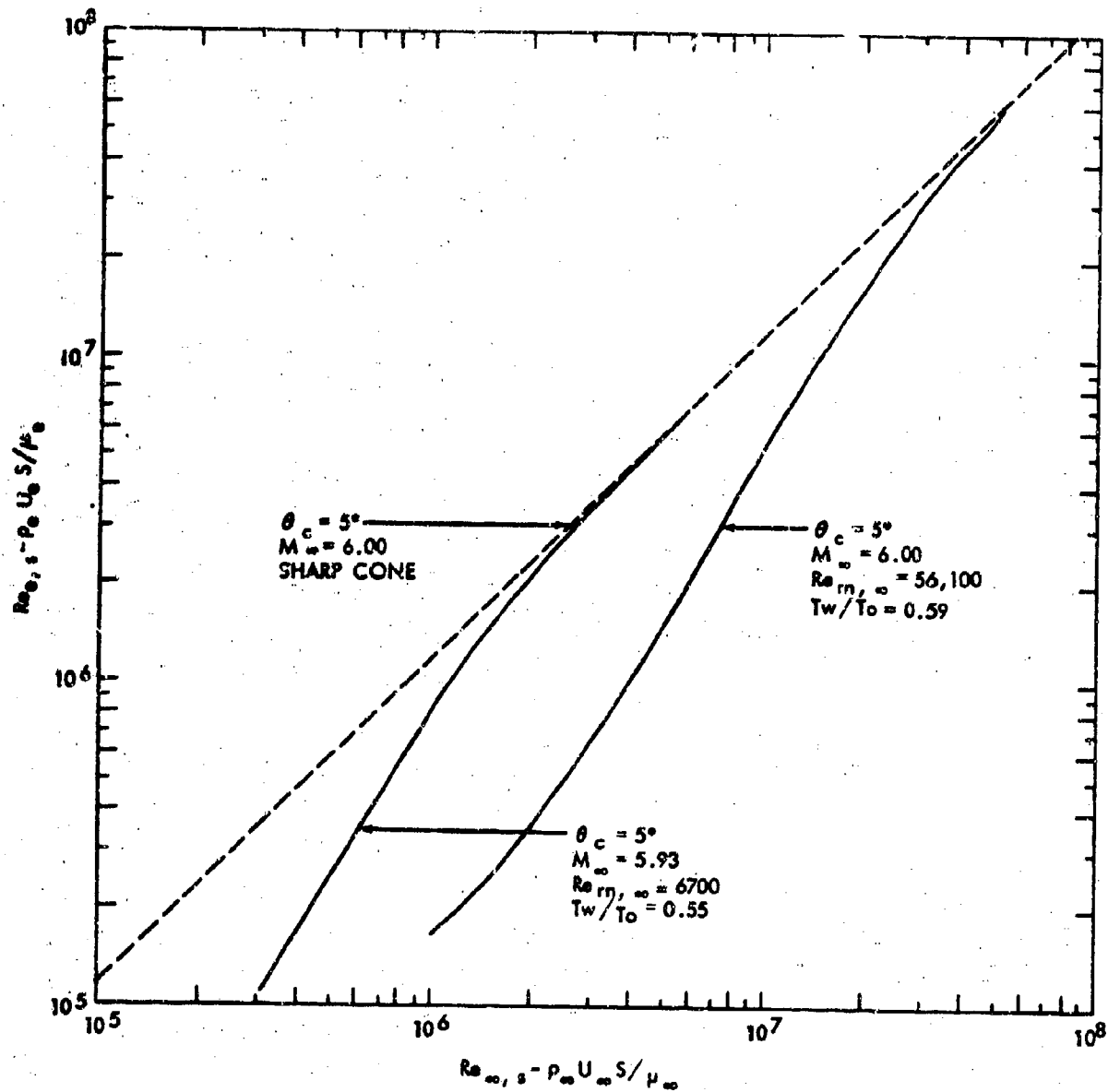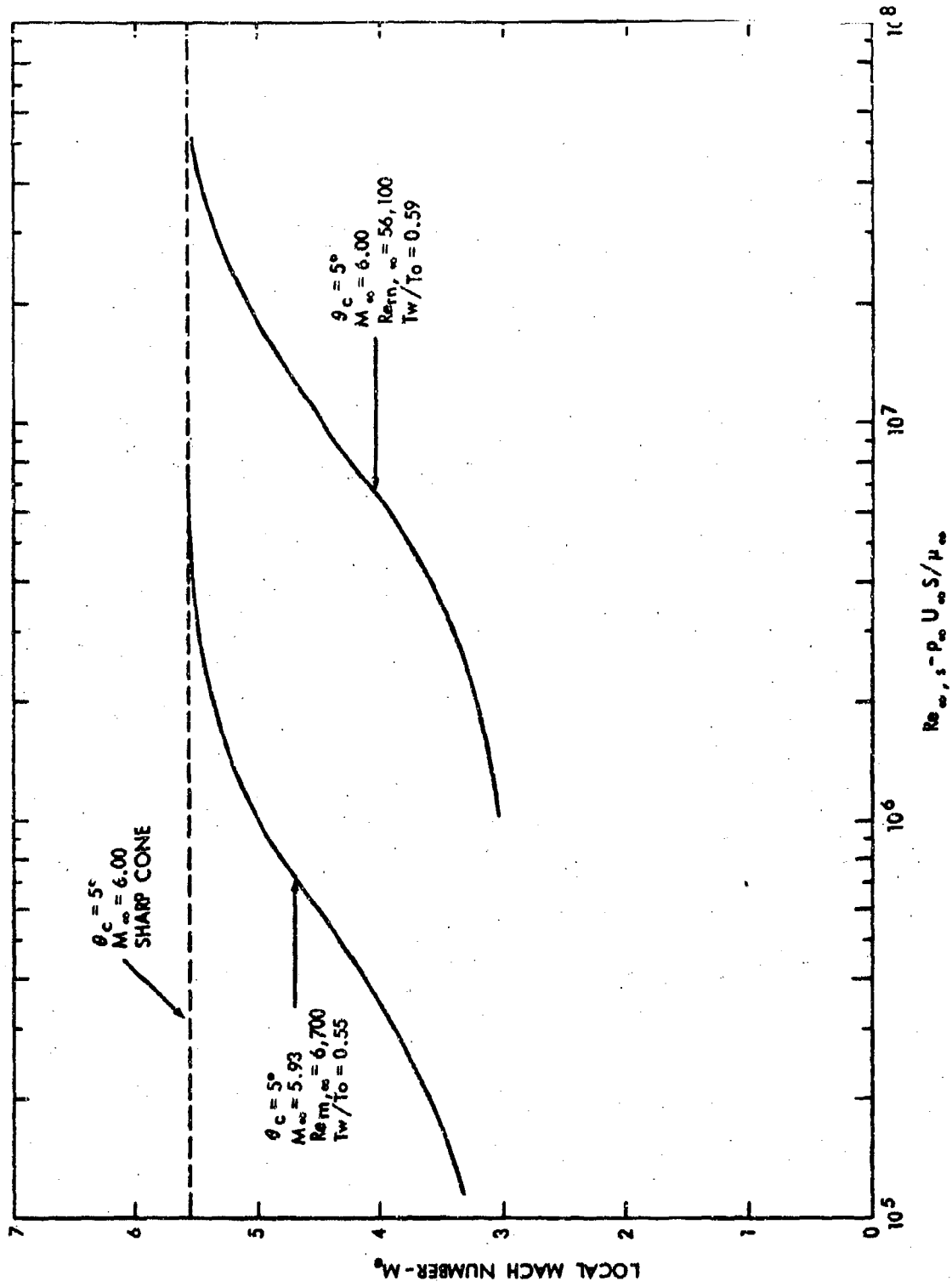
FIG. 28   EFFECT OF BLUNTNESS ON LOCAL REYNOLDS NUMBER
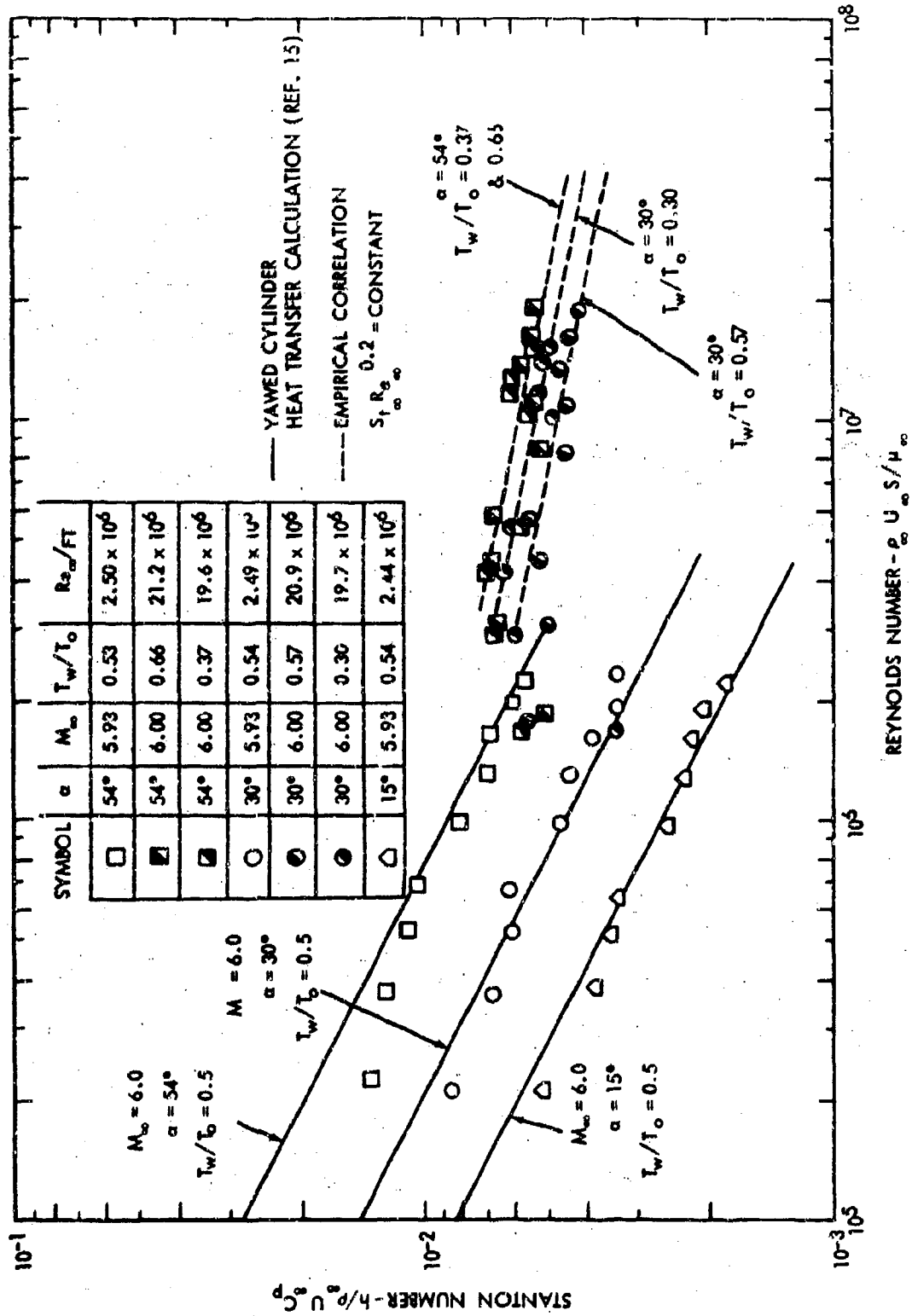
FIG. 29 EFFECT OF BLUNTNESS ON LOCAL MACH

$Re_{\infty,s} = \rho_\infty U_\infty S / \mu_\infty$

$\theta_c = 5^c$
$M_\infty = 6.00$
SHARP CONE

$\theta_c = 5^\circ$
$M_\infty = 5.93$
$Re_{n,\infty} = 6,700$
$T_w/T_o = 0.55$

$\theta_c = 5^\circ$
$M_\infty = 6.00$
$Re_{n,\infty} = 56,100$
$T_w/T_o = 0.59$

LOCAL MACH NUMBER—M_s

FIG. 30 HEAT TRANSFER DISTRIBUTION ALONG STAGNATION STREAMLINE

FIG. 31 HEAT TRANSFER DISTRIBUTION ALONG STAGNATION STREAMLINE

$M_\infty = 5.93$
$\alpha = 15°$

SYMBOL	X (inches)	Re$_\infty$/FT	Tw/T$_o$
$\bigcirc$	1.75	2.47 × 10^6	0.54
$\square$	3.25		
$\diamondsuit$	7.75		
$\triangleleft$	10.75		

NORMALIZED STANTON NUMBER - S$_T$/S$_T$ ϕ = 0
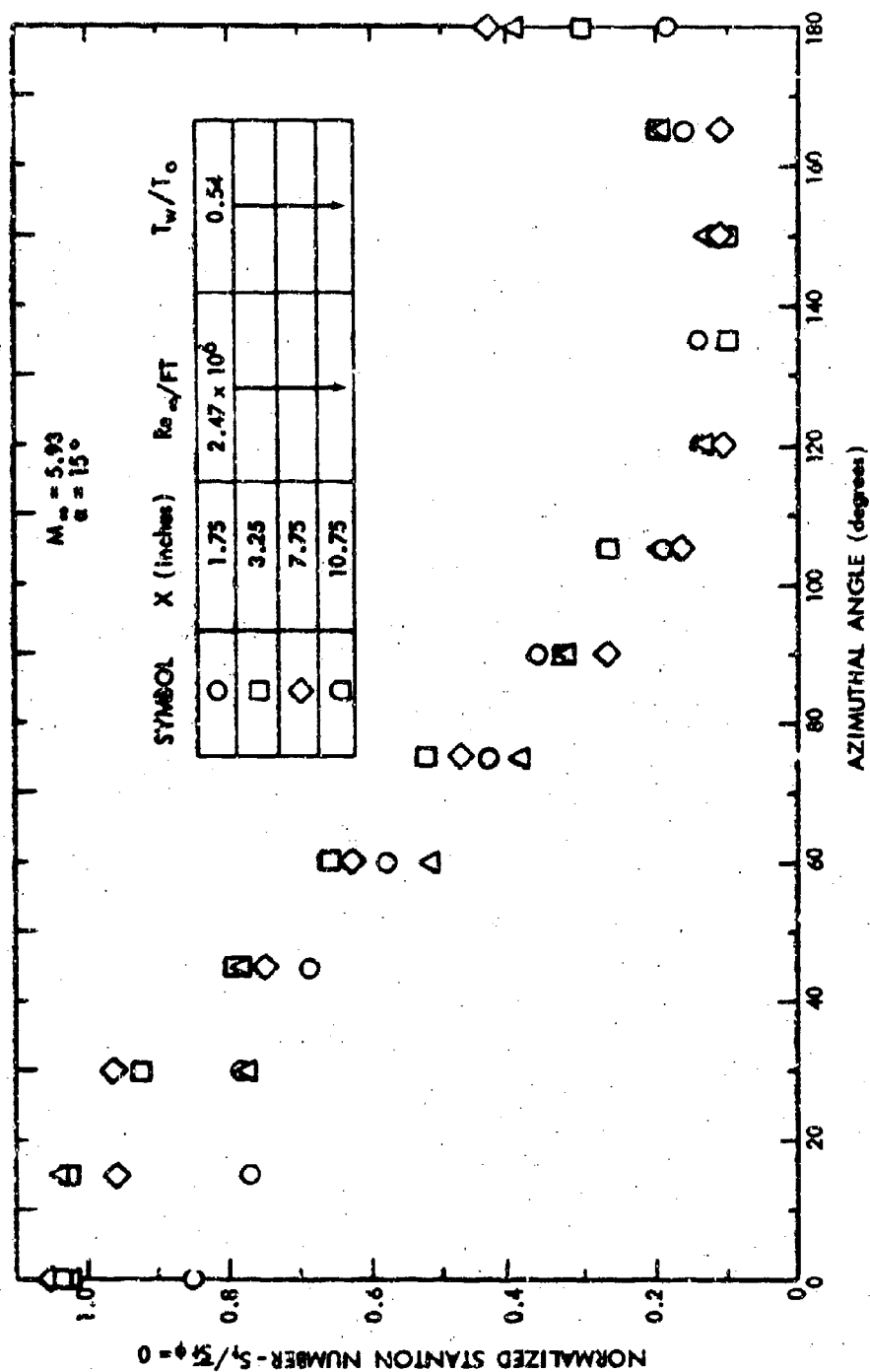
AZIMUTHAL ANGLE (degrees)
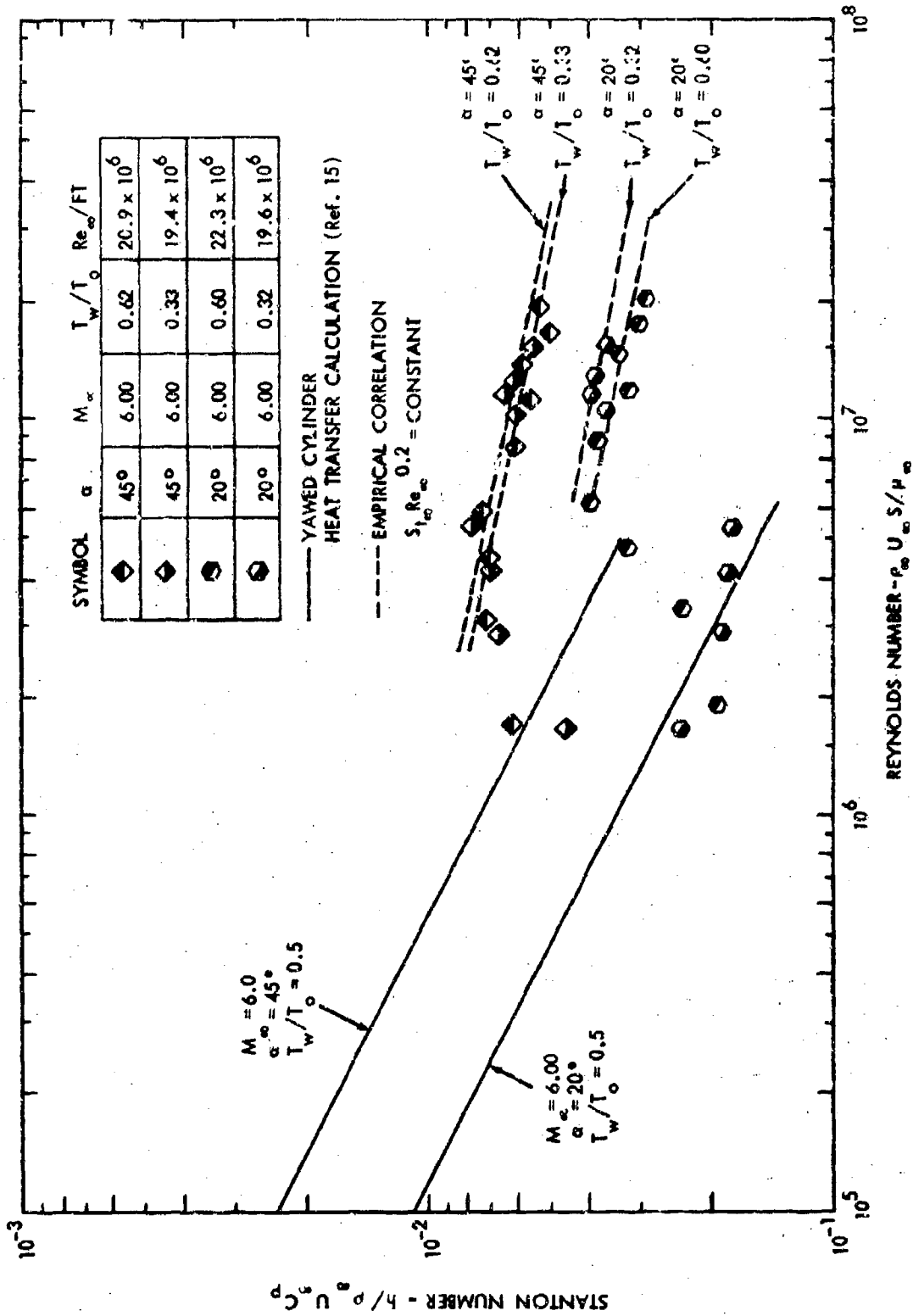
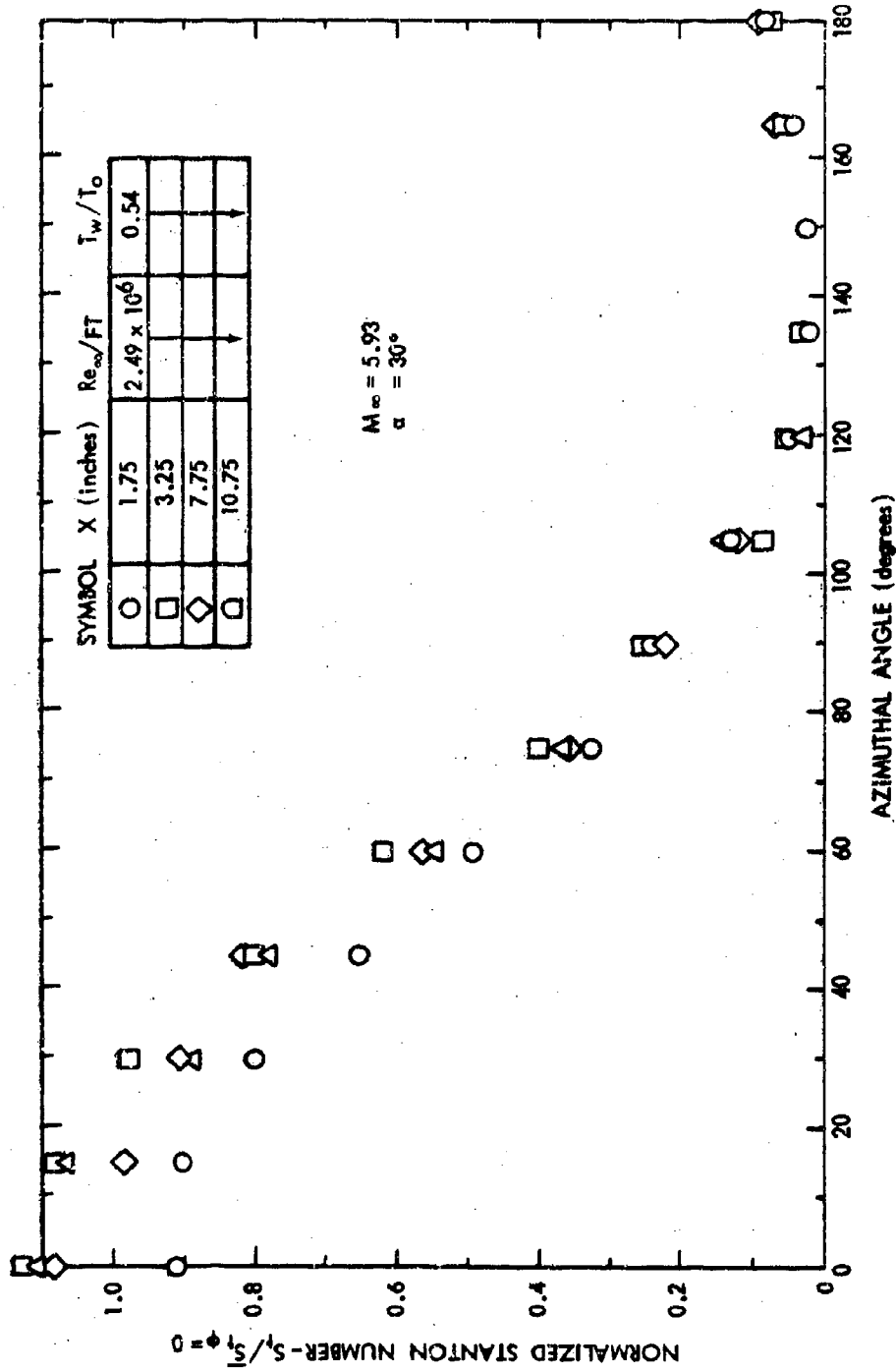FIG. 32 CIRCUMFERENTIAL HEAT TRANSFER DISTRIBUTIONS
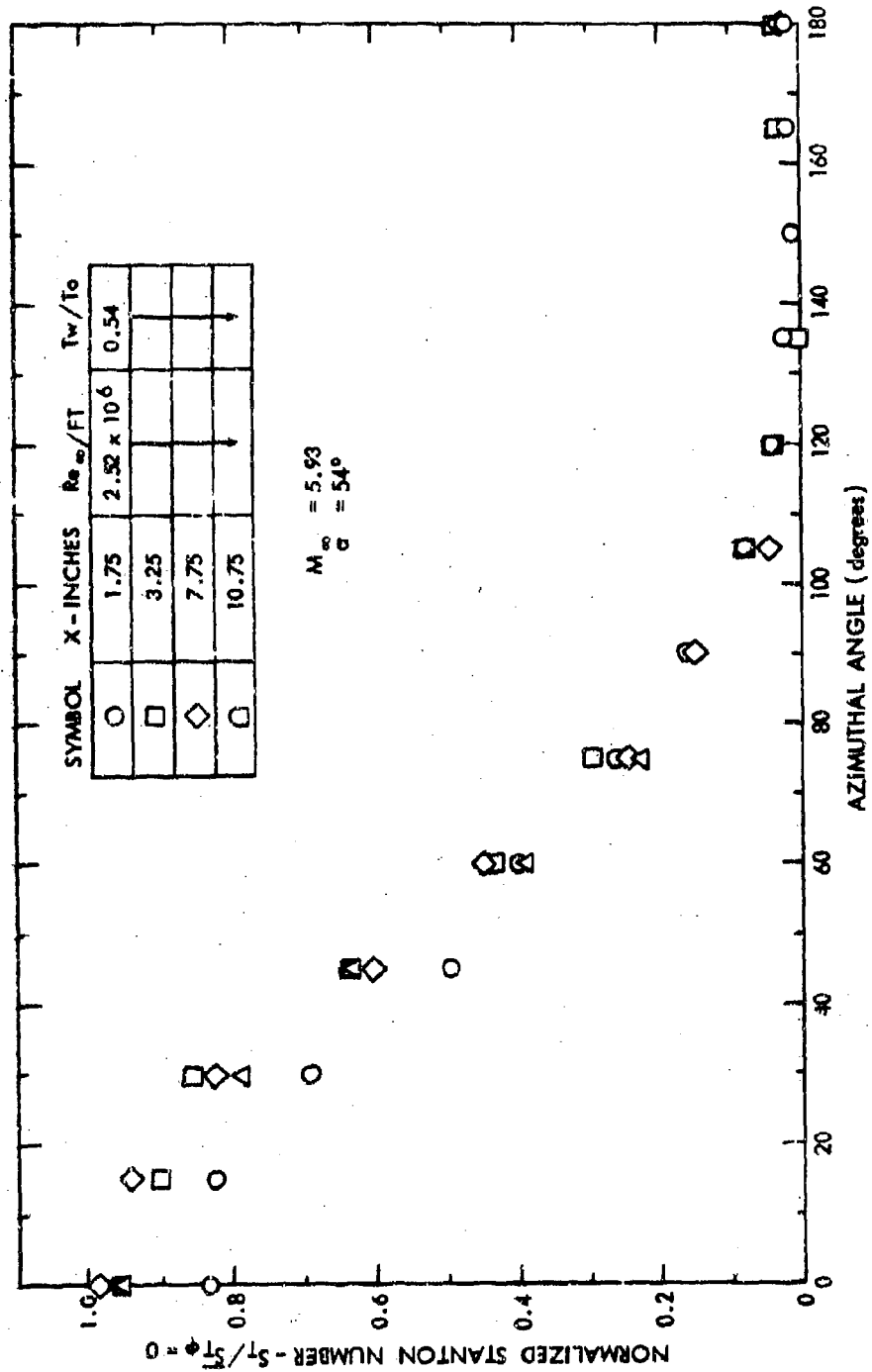
FIG. 33 CIRCUMFERENTIAL HEAT TRANSFER DISTRIBUTIONS
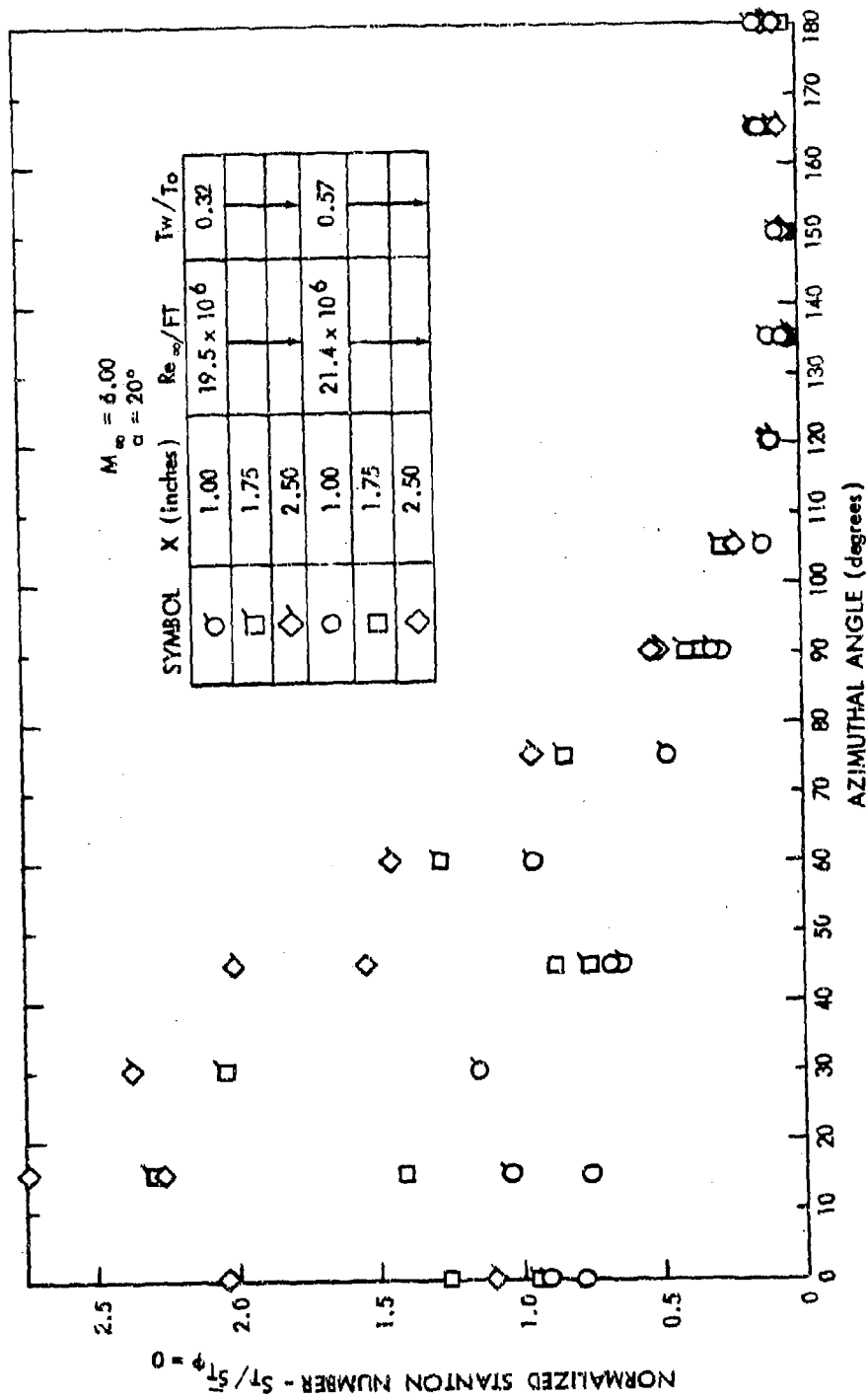
FIG. 34 CIRCUMFERENTIAL HEAT TRANSFER DISTRIBUTIONS

FIG. 35a.   CIRCUMFERENTIAL HEAT TRANSFER DISTRIBUTIONS

BLANK PAGE

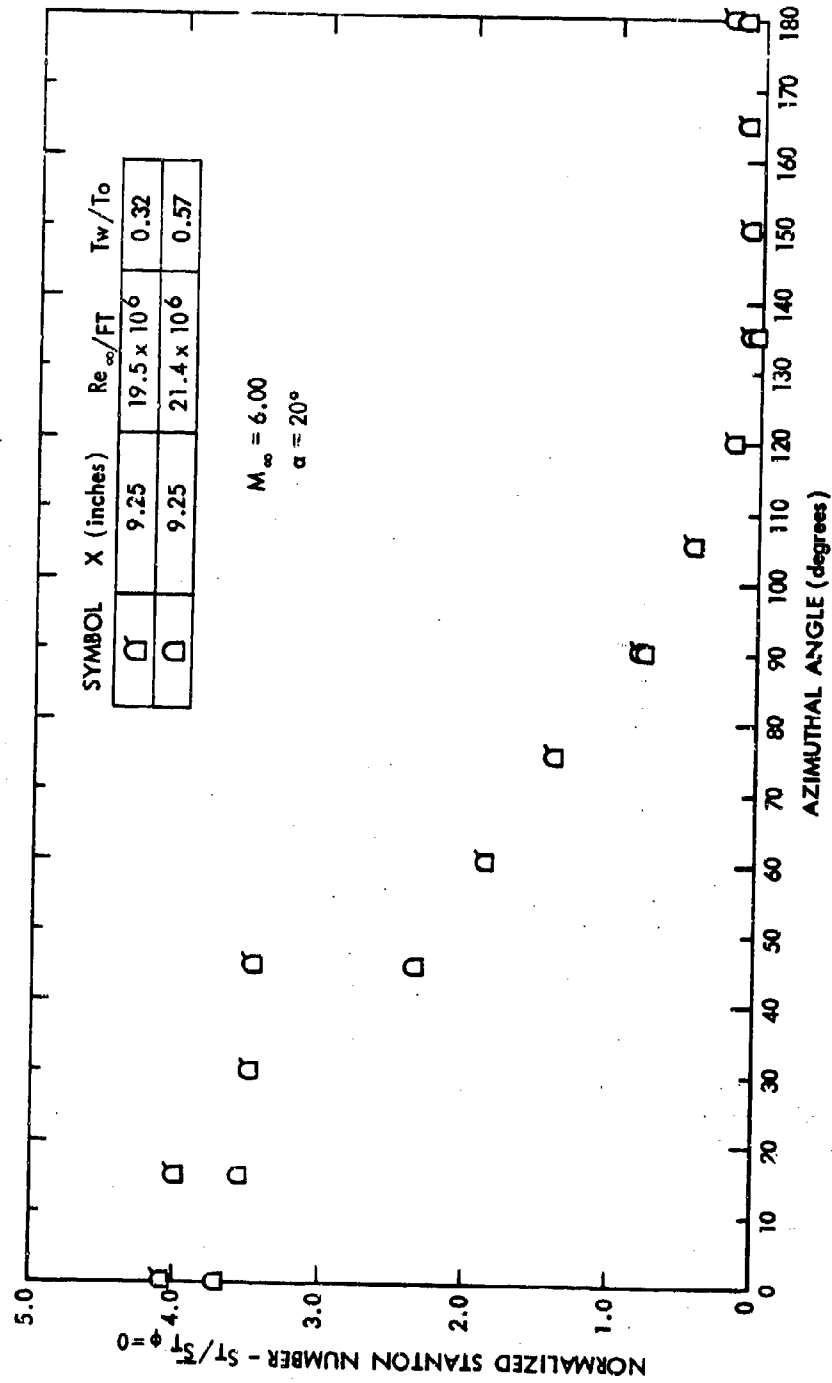FIG. 35b CIRCUMFERENTIAL HEAT TRANSFER DISTRIBUTIONS

SYMBOL	X (inches)	Re_∞/FT	Tw/To
⟂	9.25	19.5×10^6	0.32
⟂	9.25	21.4×10^6	0.57

$M_\infty = 6.00$

$\alpha = 20°$

SYMBOL	X (inches)	Re_∞/FT	Tw/To
◐	1.00	19.3×10^6	0.35
◰	1.75		
◇	2.50		
◨	9.25		
○	1.00	20.3×10^6	0.56
□	1.75		
◇	2.50		
◨	9.25		

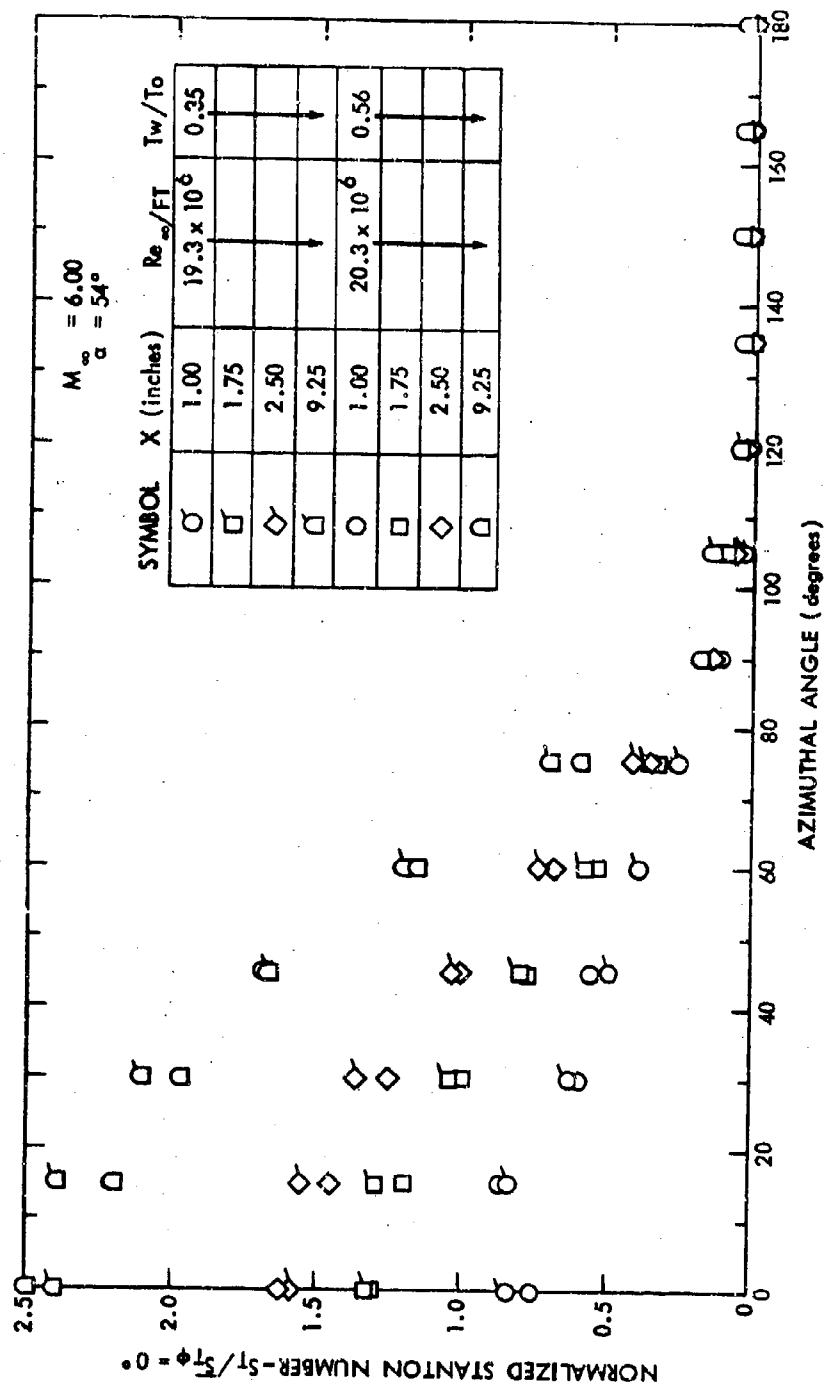$M_\infty = 6.00$
$\alpha = 54°$

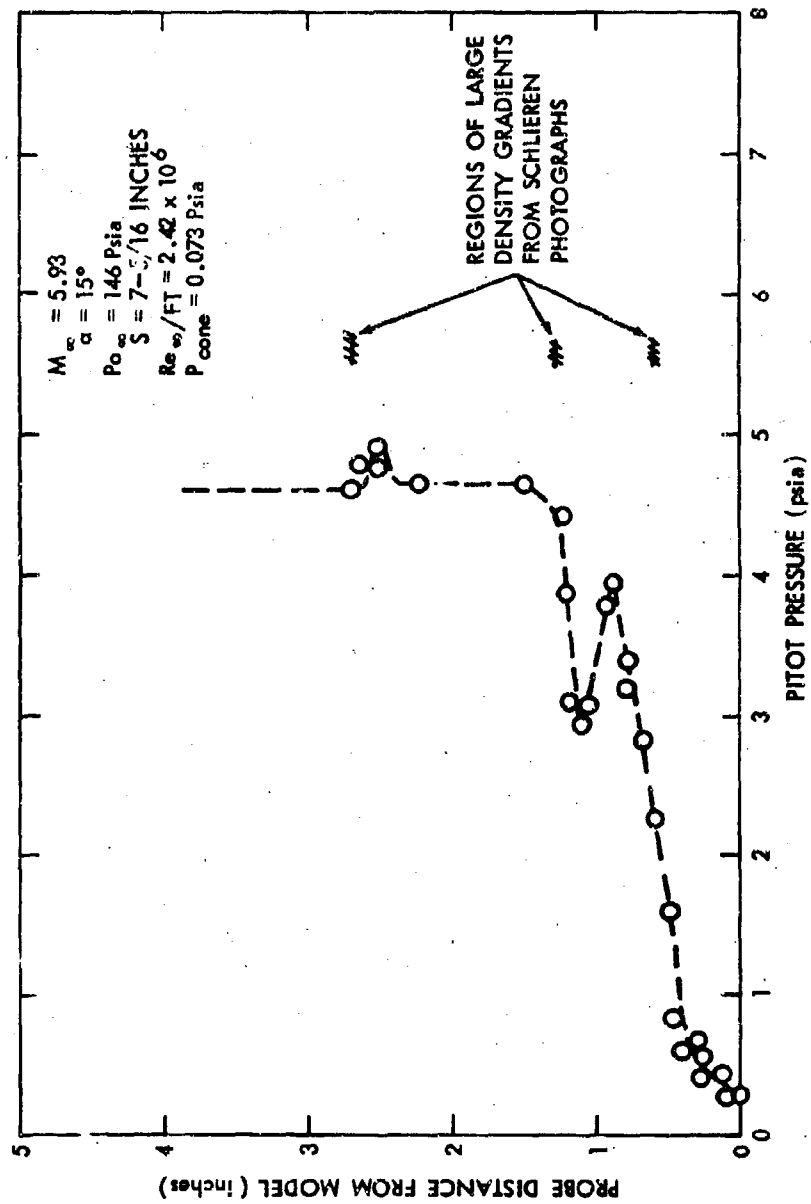FIG. 36 CIRCUMFERENTIAL HEAT TRANSFER DISTRIBUTIONS

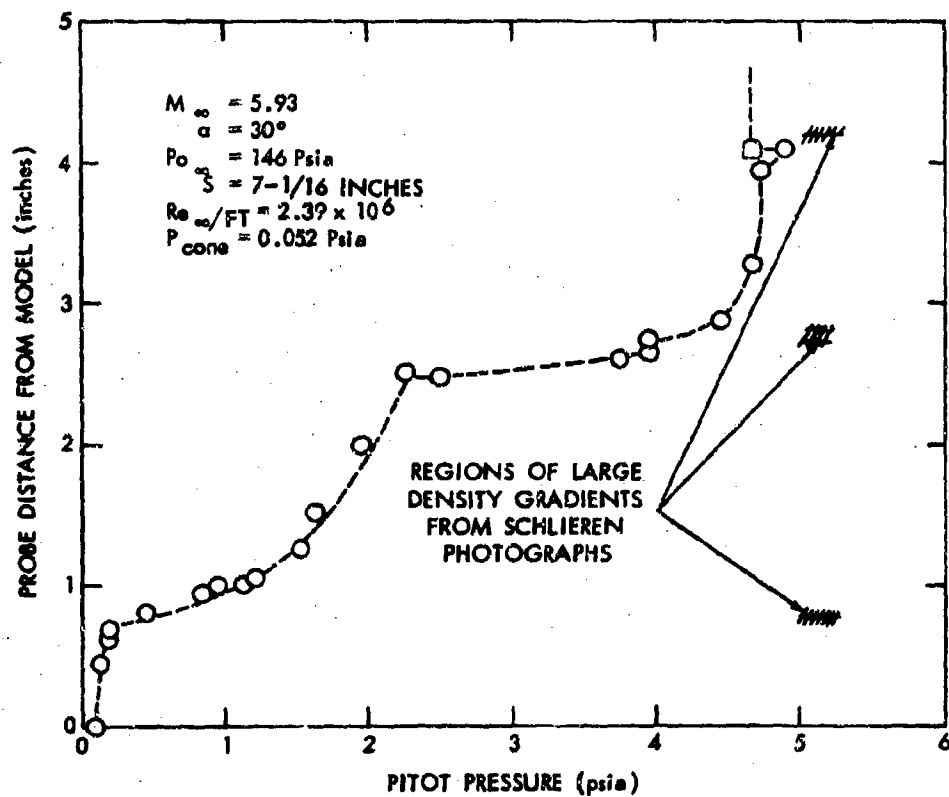FIG. 37 PITOT PRESSURE DISTRIBUTION IN THE MOST LEEWARD MERIDIAN PLANE

FIG. 38 PITOT PRESSURE DISTRIBUTION IN THE MOST LEEWARD MERIDIAN PLANE

FIG. 39   PITOT PRESSURE DISTRIBUTION IN THE MOST LEEWARD MERIDIAN PLANE

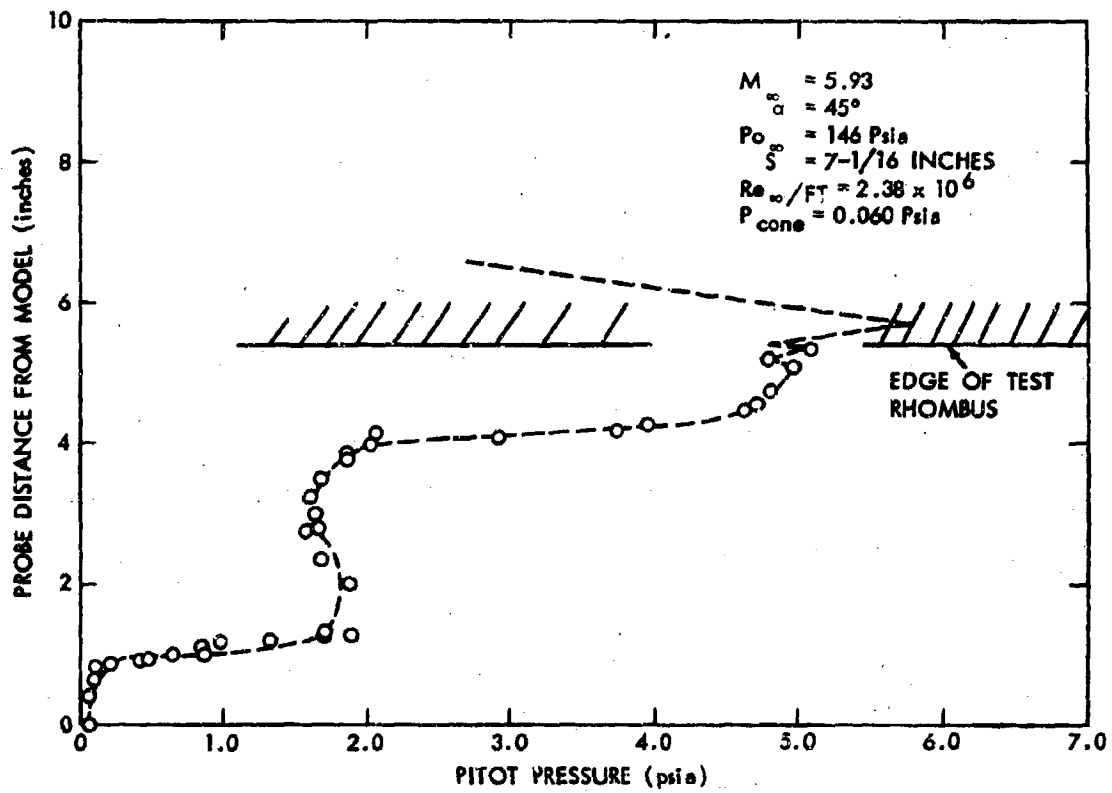FIG. 40 SCHLIEREN PHOTOGRAPH OF AN INCLINED SLENDER CONE ($\alpha = 30°$)

FIG. 41 SCHLIEREN PHOTOGRAPH OF AN INCLINED SLENDER CONE ($\alpha = 15°$)

FIG. 42 SCHLIEREN PHOTOGRAPH OF AN INCLINED SLENDER CONE ($\alpha = 16.2°$)

FIG. 43 SCHLIEREN PHOTOGRAPH OF AN INCLINED SLENDER CONE ($\alpha = 27.5°$)
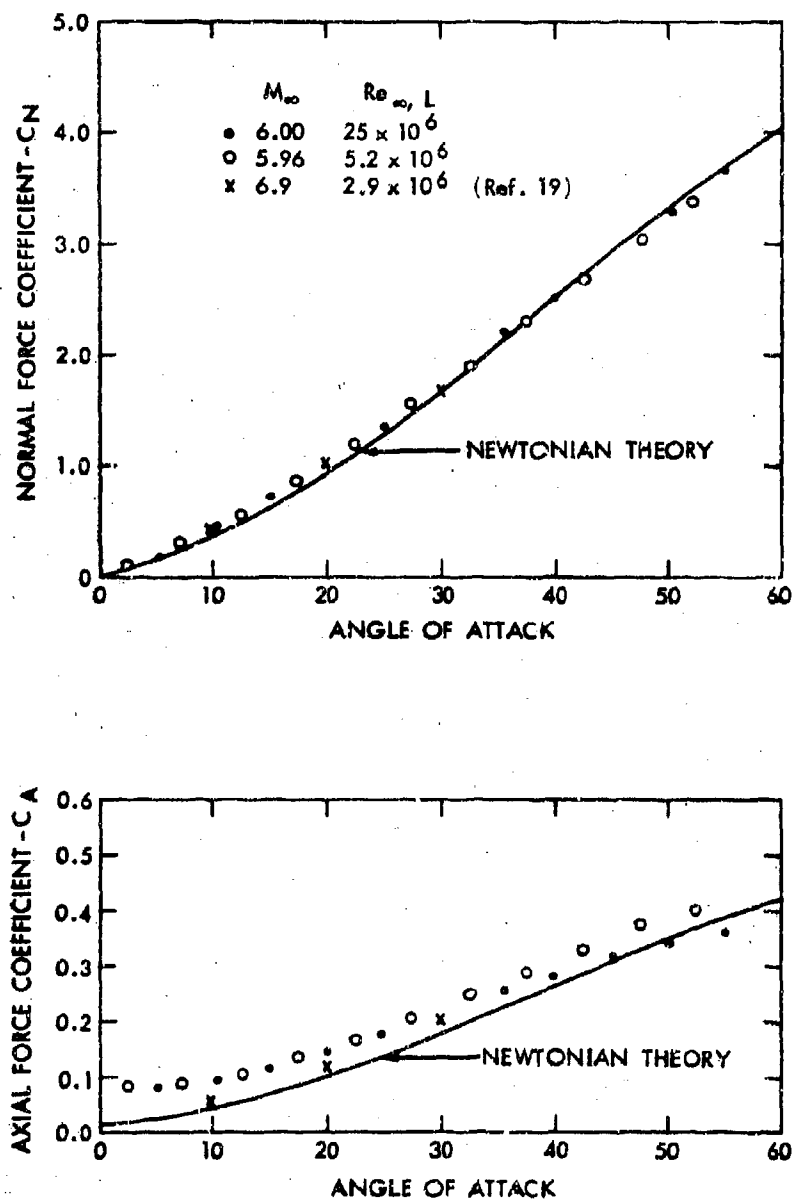
FIG. 44 NORMAL AND AXIAL FORCE COEFFICIENTS - CONFIGURATION 6FN
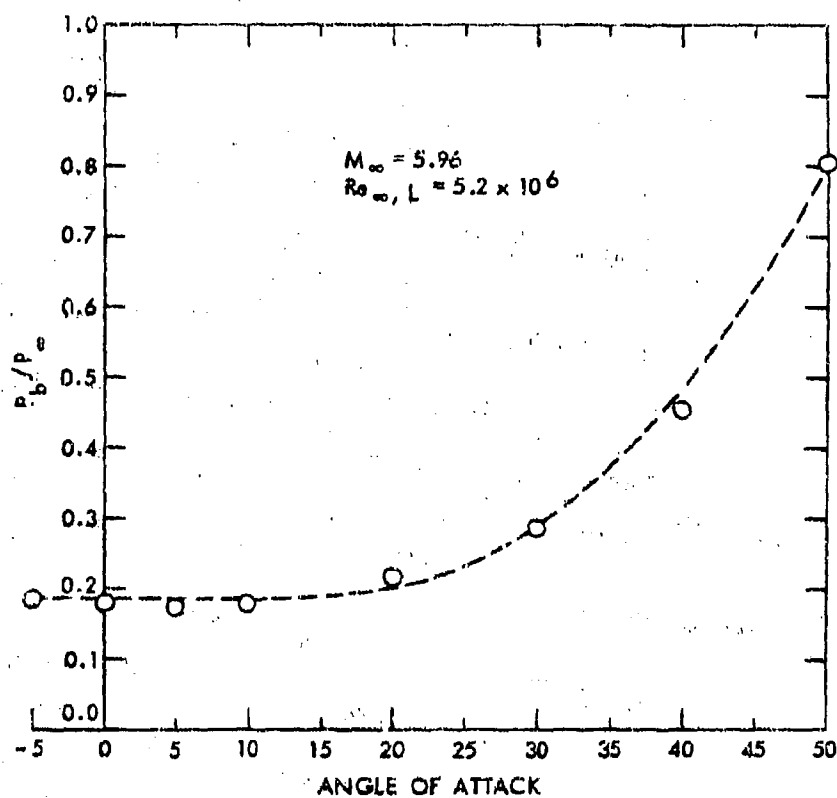
FIG. 45 VARIATION OF BASE PRESSURE WITH ANGLE OF ATTACK - CONFIGURATION 6 FN
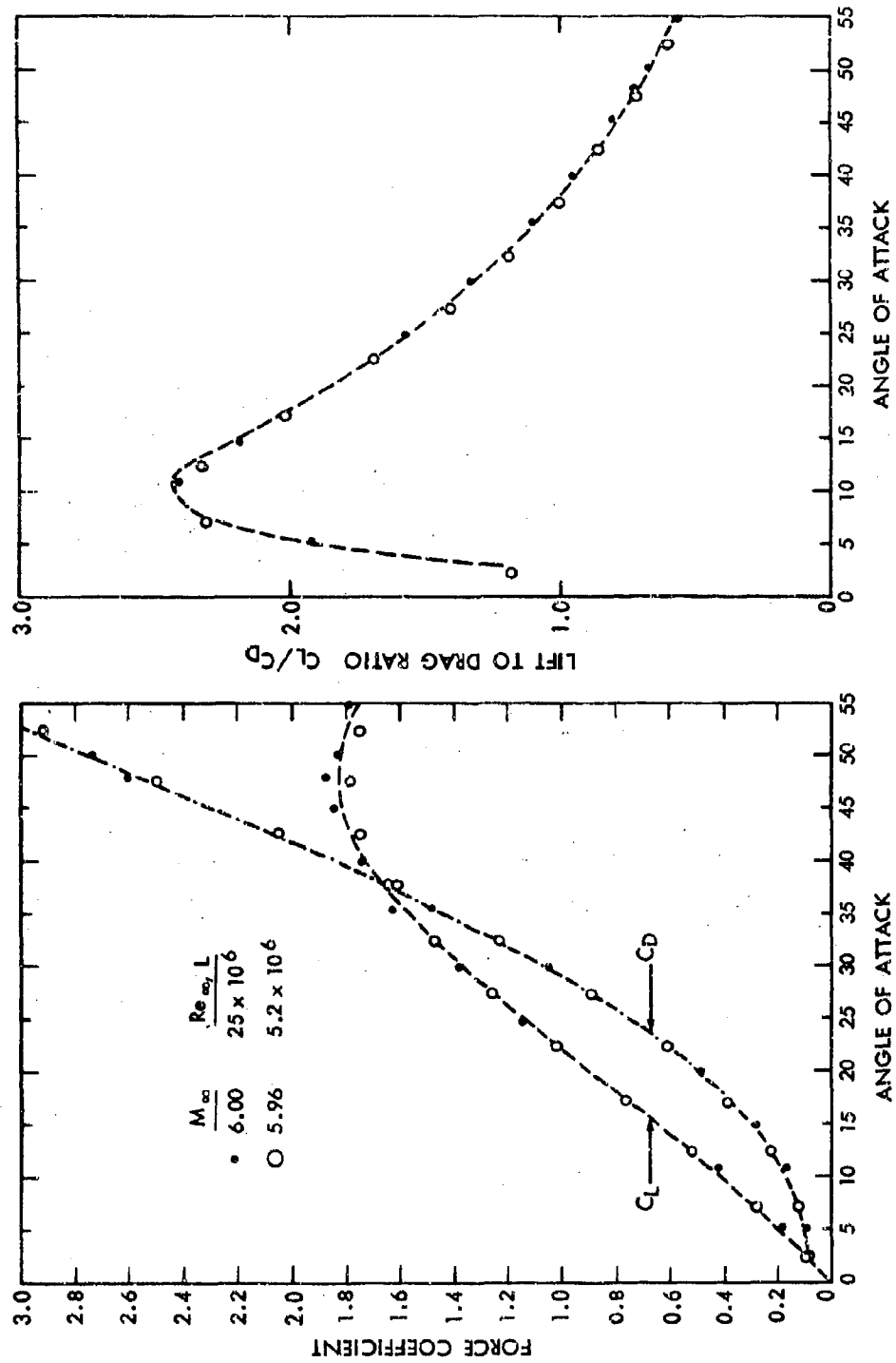
FIG. 46 LIFT AND DRAG COEFFICIENTS AND LIFT TO DRAG RATIO-CONFIGURATION 6 FN

SYMBOL	CONFIGURATION	M_∞	$Re_{\infty, L}$
O	6 FN	5.96	5.2×10^6
•	6 FN	6.00	25×10^6
X	6 FX-1	6.00	25×10^6
□	6 FX-2-1	6.00	30×10^6
△	6 FX-2-2	6.00	29×10^6
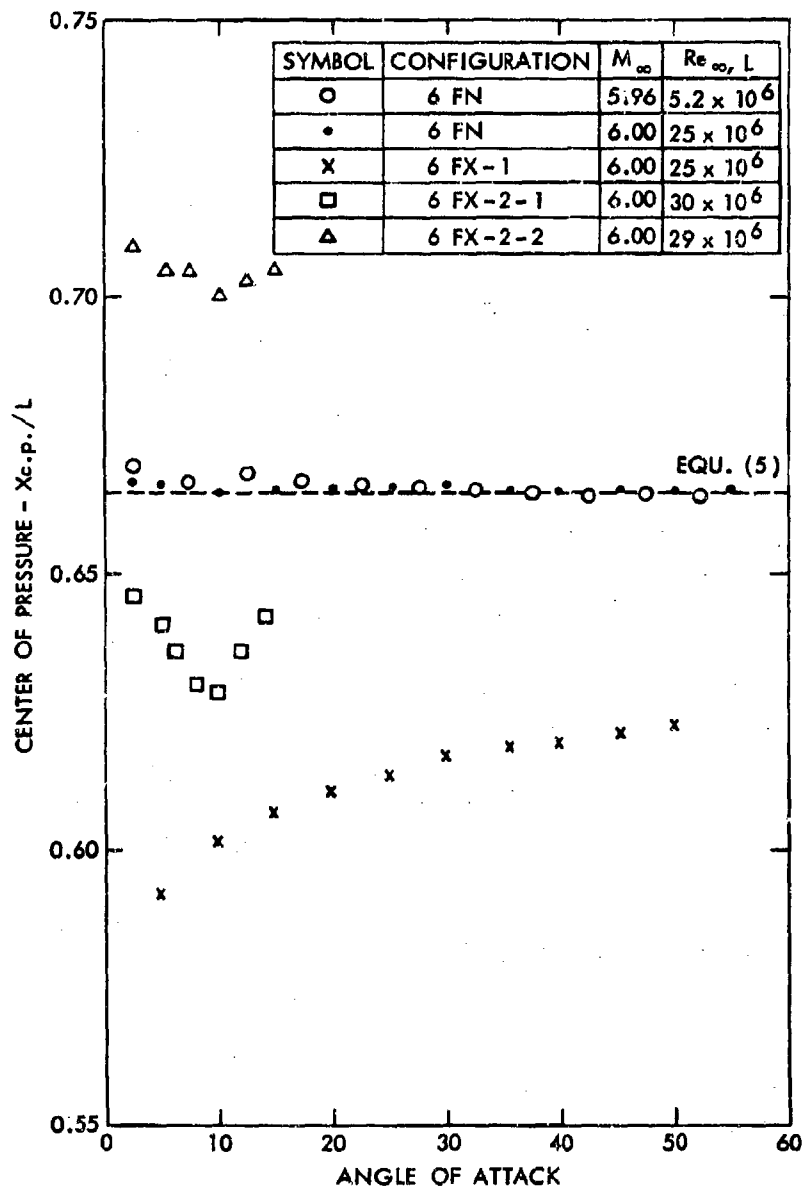
FIG. 47 VARIATION OF CENTER OF PRESSURE

FIG. 48 NORMAL AND AXIAL FORCE COEFFICIENTS - CONFIGURATION 6FX-1

FIG. 49 LIFT AND DRAG COEFFICIENTS AND LIFT TO DRAG RATIO - CONFIGURATION 6FX-1

FIG. 50   NORMAL AND AXIAL FORCE
COEFFICIENTS - CONFIGURATION 6 FX - 2 - 1

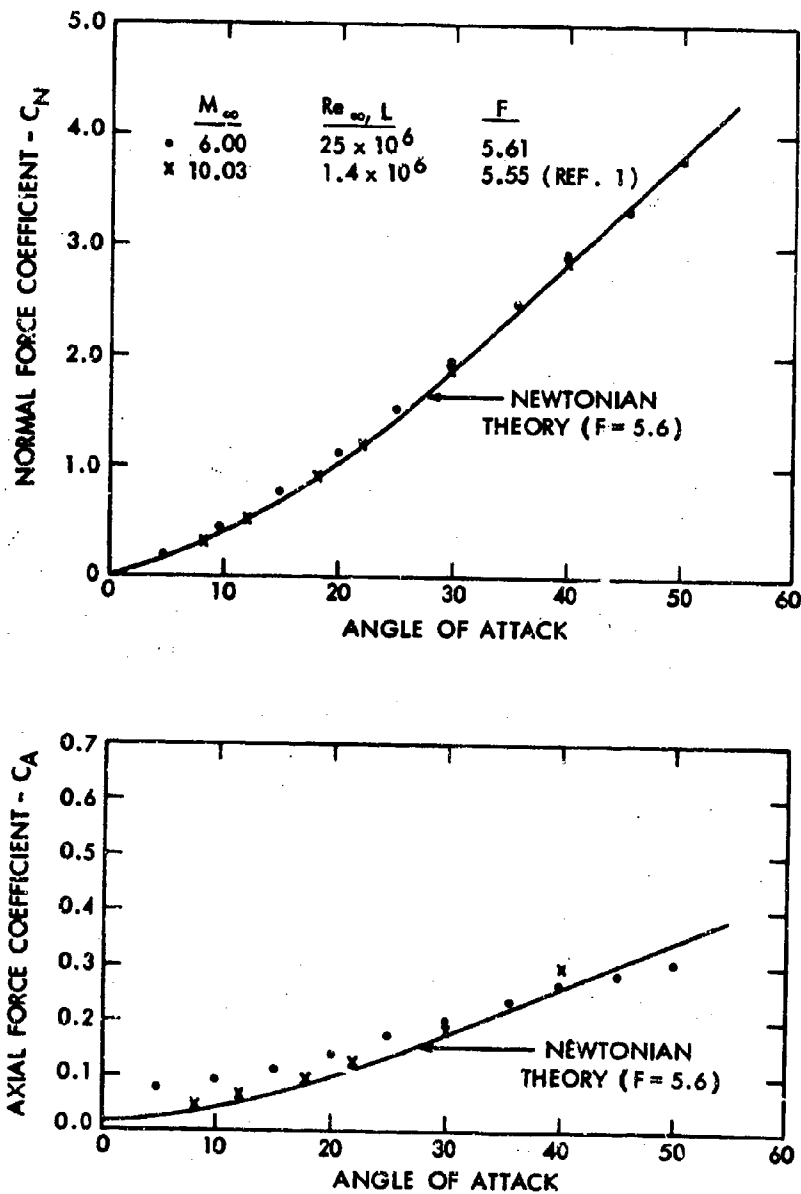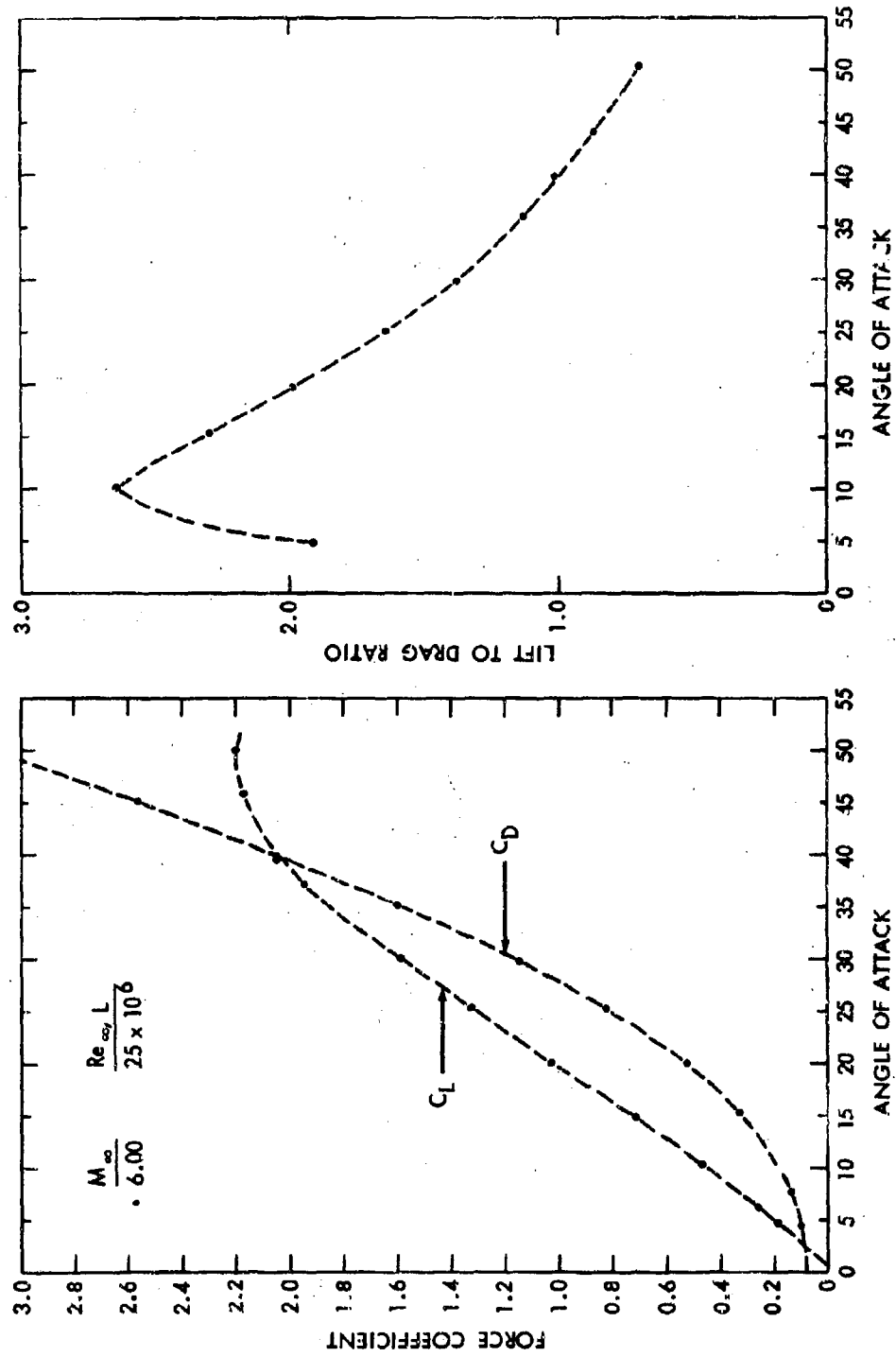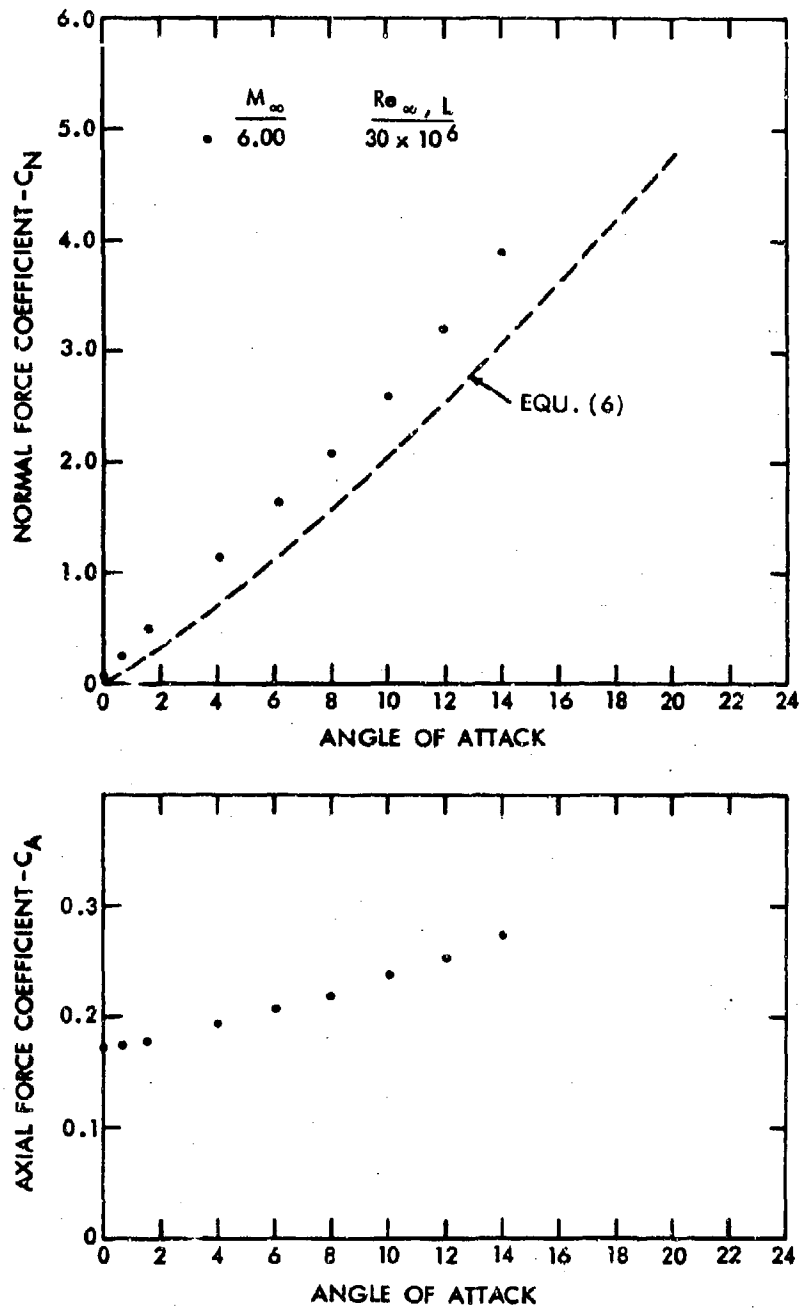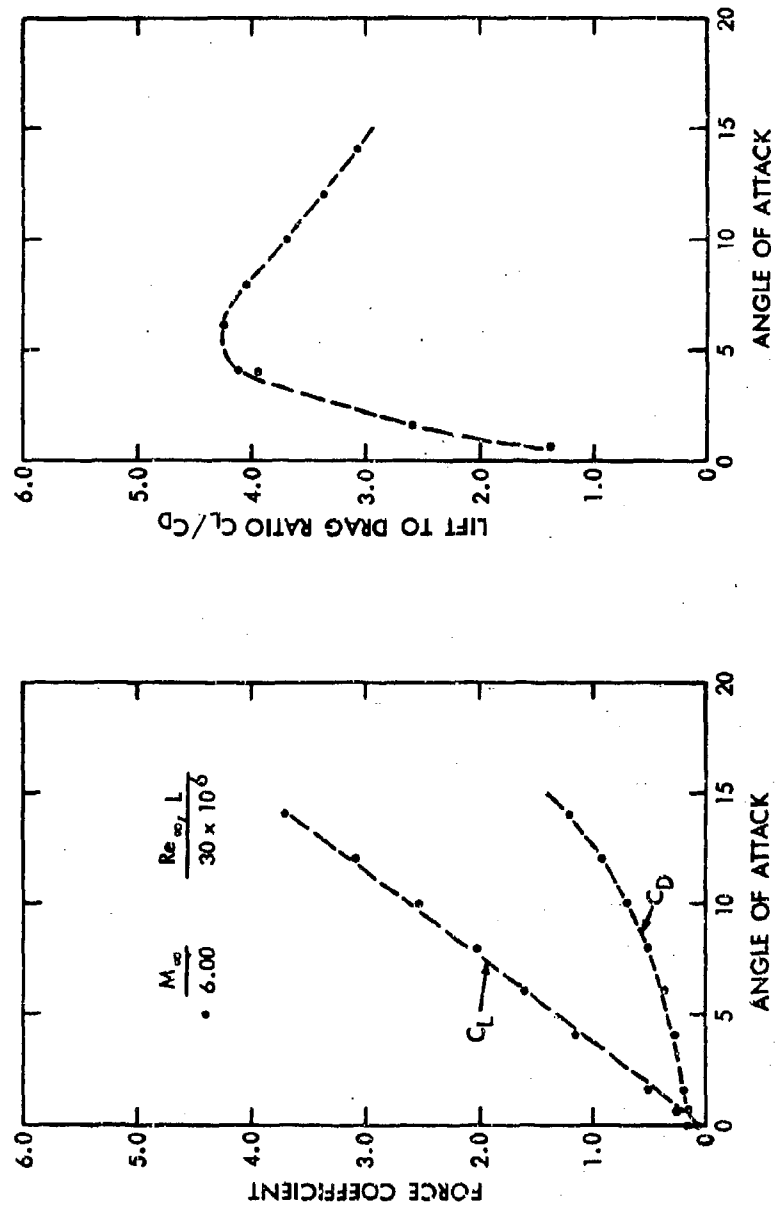FIG. 51 LIFT AND DRAG COEFFICIENTS AND LIFT TO DRAG RATIO - CONFIGURATION 6FX-2-1
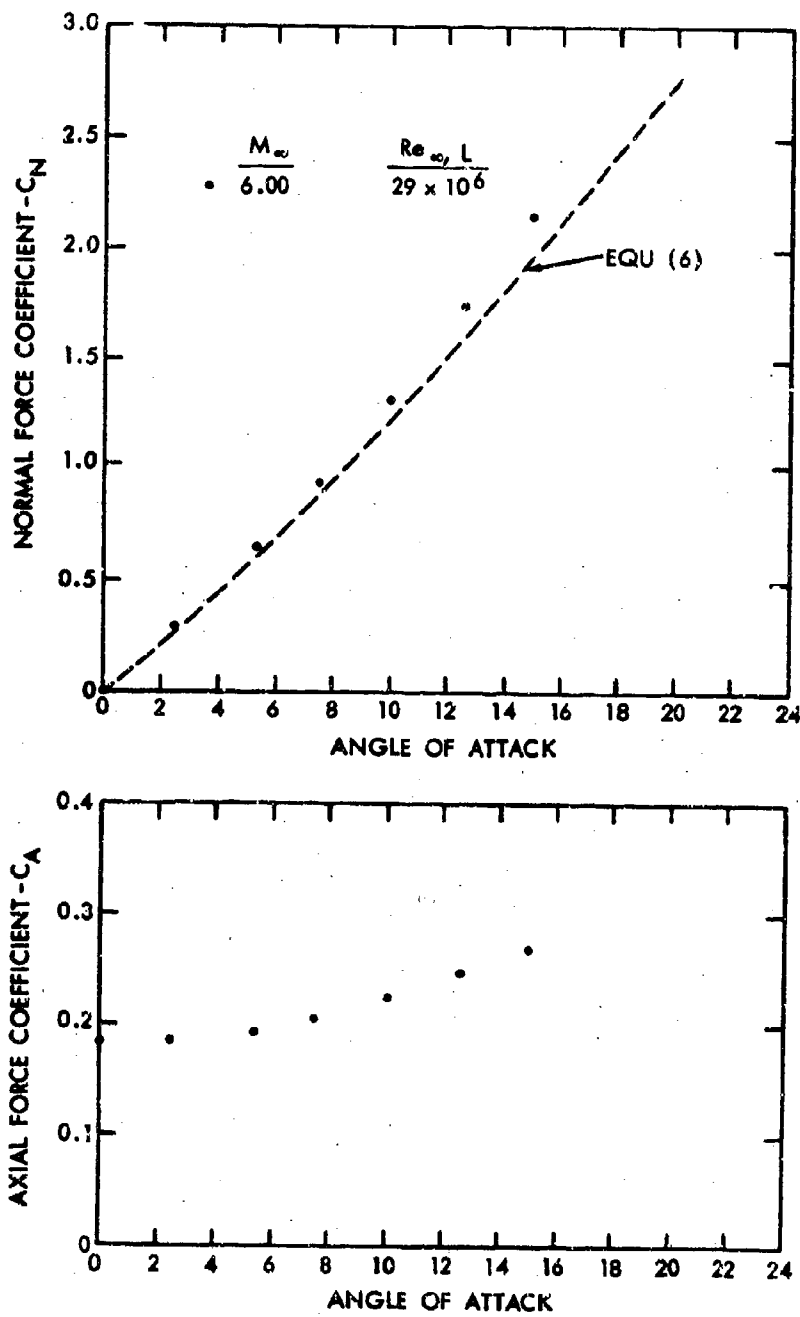
FIG. 52 NORMAL AND AXIAL FORCE COEFFICIENTS -
CONFIGURATION 6FX-2-2
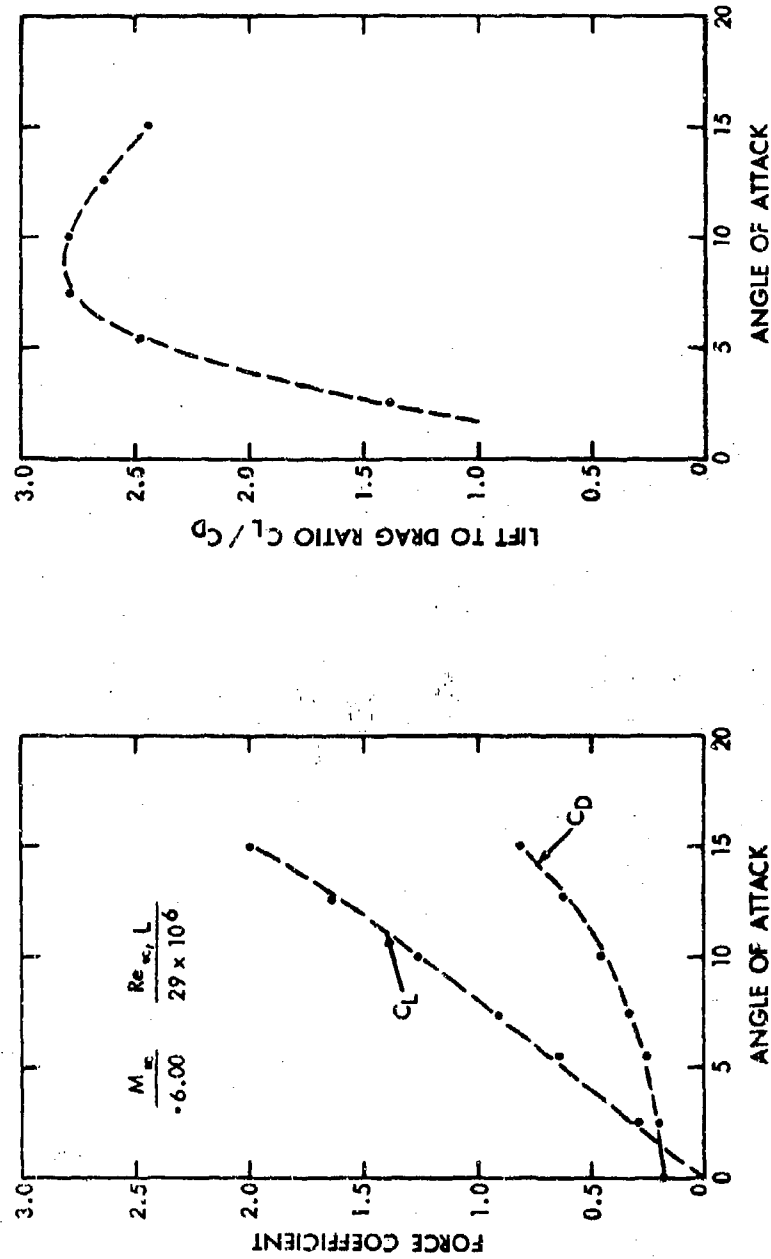
FIG. 53 LIFT AND DRAG COEFFICIENTS AND LIFT TO DRAG RATIO - CONFIGURATION 6FX-2-2

BLANK PAGE

APPENDIX

Heat Transfer Data Reduction

The heat transfer data has been determined by assuming that each element of the model acts like a calorimeter. The temperature gradient normal to the surface, and the heat lost due to tangential conduction have thus been neglected Normal and longitudinal heat transfer are separately considered in this appendix in order to provide a means of estimating the errors associated with these effects.

(1) Correction for normal temperature gradient:

The heat transfer data was determined by equating the rate at which heat is stored within each element of the model with the convective heat transfer rate to the surface:

$$-h'(T_w - T_e)(ds) = \rho_w c_w (dv) \frac{dT_w}{d\tau}$$

This equation can be readily integrated if h', ρ_w, c_w, and $\left(\frac{dv}{ds}\right)$ are assumed to be independent of temperature:

$$\frac{T(\tau) - T_e}{T_i - T_e} = e^{-\frac{h'd}{k}\left(\frac{\alpha_m \tau}{d^2}\right)}$$

$$\text{where } \alpha_m = k/\rho_w c_w$$

$$d = dv/ds$$

The measured Biot number $\left(\frac{h'd}{k}\right)$ is then determined from the measured temperatures at two different times and is expressed by:

$$\frac{h'd}{k} = \left(\frac{d^2}{-\alpha_m \Delta \tau}\right) \ln\left[\frac{T_e - T(\tau_1)}{T_e - T(\tau_2)}\right]$$

(1)

where $\Delta \tau = \tau_2 - \tau_1$

Associated with the data reduction in this manner, is the assumption that there is no temperature gradient across the thin skin. Consequently, one assumes for a thin skin heat transfer model that the knowledge of the distance of the thermocouples below the surface is not necessary for the data reduction. In order to assess the accuracy of this assumption, the results of calculations of the temperature distribution within an infinitely long thin flat plate, insulated on one surface and subjected to convective heating on the other surface have been analyzed in a manner similar to that presented in reference (22).

The solution for the temperature distribution within the convectively heated plate is given in reference (23) and the results are quoted below:

Solution:

$$\frac{T(x/d, \tau) - T_e}{T_i - T_e} = \sum_{n=1}^{\infty} \frac{2 \sin(\lambda_n d) \cos(\lambda_n d \cdot x/d)}{(\lambda_n d) + \sin(\lambda_n d) \cos(\lambda_n d)} e^{-(\lambda_n d)^2 \frac{\alpha_m}{d^2} \tau}$$

(2)

where

$$(\lambda_n d) \tan(\lambda_n d) = \frac{hd}{k}$$

The above solution shows that the temperature does vary across the slab of finite thickness (d). It should also be noted that for vanishingly small values of the Biot number $\left[(hd/k) \ll 1\right]$ and Fourier

numbers $(\alpha_m \tau/d^2)$ larger than approximately 1, the above expression for
the temperature distribution closely approximates that obtained by
balancing the convective heat transfer with the stored heat transfer.
(The dependence of the temperature distribution upon the distance from
the surface disappears for small Biot numbers as $\tan(\lambda_1 d) \approx \sin(\lambda_1 d) \approx$
$(\lambda_1 d)$ and $\cos(\lambda_1 d \frac{\ell}{d}) \approx 1.0$.)

In order to assess the accuracy of the results obtained from
equation 1 a simple iterative procedure was employed using the above
exact solution:

(1) A Biot number (hd/k) and a time increment $(\alpha_m \Delta\tau/d^2)$ were
assumed to calculate the temperature variation with respect to time
at any point of the flat plate.

(2) The temperature at two Fourier numbers $\left(\dfrac{\alpha_m \tau_1}{d^2} \text{ and } \dfrac{\alpha_m \tau_2}{d^2}\right)$
were than substituted into equation 1 to calculate the Biot number
$\left(\dfrac{h'd}{k}\right)$ over that interval of time.

(3) The difference between (h') and (h) is the error incurred
by neglecting the temperature gradient normal to the surface of the
flat plate.

The results of these calculations are presented in figures
(A-1) & (A-2), in the form of calculated Biot number versus Fourier
number for different increments of the Fourier number. It is noted
from these results that for Biot numbers less than 0.5, the Biot
number determined from the calorimeter assumption is independent of
the point in the surface where the measurement is made if the tempera-
ture data obtained before a Fourier number of approximately 0.5 is
neglected. It is also noted that the error between the Biot number
determined from the calorimeter assumption $(h'd/k)$ and the actual

Biot number $h'd/k$ increases with increasing Biot number.

If one considers the first two terms in the infinite series representations for the temperature distribution (equation 2) and the tangent function, then it can be shown by considering equations 1, 2 and 3 for $\frac{\alpha_m \tau}{d^2} > 1.0$, that a better approximation for the Biot number is given by:

$$\frac{h''d}{k} = \frac{3}{4}\left[\left(\frac{2}{3}\frac{h'd}{k}+1\right)^2 - 1\right]$$

(4)

The relative errors (defined as $\frac{h-h'}{h}$ and $\frac{h-h''}{h}$) introduced into the measured heat transfer coefficients by reducing the data by the calorimeter method (equation 1) and by the calorimeter method with a correction (equation 4) are presented in figure (A-3) as a function of the actual Biot number.

It is noted for a thin flat plate, that the error in the heat transfer coefficient which is introduced by assuming that each element of the plate acts like a calorimeter is approximately 10 percent at a Biot number of approximately 0.3. For the present series of tests, the measured Biot number did not exceed 0.10 and the maximum error associated with the uncorrected calorimeter approximation is estimated to be less than 3.5 percent.

By applying the single correction (equation 4) which accounts for the fact that $d/k \neq 0$, the error can be reduced to less than 3 percent for Bi < 0.5.

(2) Tangential conduction corrections:

As noted previously, the presented data has been reduced by assuming that each element of the body surface acts like a calorimeter. Losses associated with heat transfer by conduction around or along the model, or down the thermocouple leads have also been neglected.

A-4

Since the rate at which heat is conducted across a solid surface varies inversely with the cross-sectional area, the heat transfer model was instrumented with 0.005 (inch) diameter thermocouple wire in an attempt to minimize thermocouple losses.

In order to assess the errors introduced by heat conduction around or along the model, an analysis similar to that presented in reference (24) was performed for a thin conical shell subjected to convective heat transfer on one surface and insulated on the other. In order to simplify the analysis, the temperature gradient normal to the surface of the cone at each station, and any variation of wall thickness along the cone have been neglected. A sketch illustrating the important dimensions of the problem is shown below.
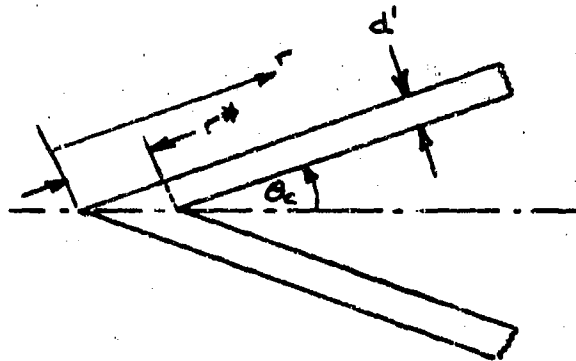
The differential equation and boundary conditions are given below for an infinite thin conical shell which is insulated on one side.

$$\rho_\omega C_\omega d \frac{\partial T}{\partial \tau} = -h(T - T_e) + dk \left[\frac{\partial^2 T}{\partial r^2} + \left(\frac{1}{r - \frac{d'}{2}} \right) \frac{\partial T}{\partial r} + \frac{1}{(r - \frac{d'}{2})^2 \sin^2 \theta_c} \frac{\partial^2 T}{\partial \varphi^2} \right]$$

where: $d = \left(\frac{dv}{ds} \right) = d' \left[1 - \frac{d'}{2r \tan \theta_c} \right]$

Boundary conditions:

(1) $\tau = 0 \qquad T = T_e (r, \varphi)$

(2) $\tau > 0 \qquad h = h(r, \varphi)$

A-5

The above differential equations and boundary conditions can be expressed as follows.

$$-\frac{hd}{k}\frac{d_m T^*}{d^2}\Theta - \frac{\partial\Theta}{\partial\chi} - \alpha_m T^*\left[\frac{\partial^2\Theta}{\partial\xi^2} + \frac{1}{\xi}\frac{\partial\Theta}{\partial\xi} + \frac{1}{\xi^2\sin^2\theta_c}\frac{\partial^2\Theta}{\partial\varphi^2}\right]$$

where $\Theta = \dfrac{T - T_e}{T_2 - T_e}$; $\xi = r - \dfrac{\xi^*}{\xi}$; $\chi = t/t^*$

Boundary conditions: (1) $\chi = 0$ $\Theta = \Theta_i(\xi,\varphi)$; (2) $\chi > 0$ $h = h(\xi,\varphi)$

In order to obtain a solution for θ, it is assumed that θ is expressible as a series solution of the form:

$$\Theta(\xi,\varphi,\chi) = \Theta_0(\xi,\varphi,\chi) + \alpha_m T^*\Theta_1(\xi,\varphi,\chi) + \ldots\ldots + (\alpha_m T^*)^m\Theta_n + \ldots$$

It is assumed that

$$\left|\frac{\partial\Theta_n}{\partial\chi} + \frac{hd}{k}\frac{d_m T^*}{d^2}\Theta_n\right| \gg \left|(\alpha_m T^*)\left(\frac{\partial^2\Theta_n}{\partial\xi^2} + \frac{1}{\xi}\frac{\partial\Theta_n}{\partial\xi} + \frac{1}{\xi^2\sin^2\theta_c}\frac{\partial^2\Theta}{\partial\varphi^2}\right)\right|$$

$$\left|(\alpha_m T^*)^n\Theta_n\right| \ll \left|(\alpha_m T^*)^{n-1}\Theta_{n-1}\right|$$

$$\partial d/\partial\xi \approx 0$$

After substituting the series solution into the partial differential equation, collecting the coefficients of the same powers of $\alpha_m T^*$ and equating them to zero, the following differential equations are obtained:

$$0 = \frac{\partial\Theta_0}{\partial\chi} + \frac{hd}{k}\frac{d_m T^*}{d^2}\Theta_0$$

$$\frac{\partial^2\Theta_0}{\partial\xi^2} + \frac{1}{\xi}\frac{\partial\Theta_0}{\partial\xi} + \frac{1}{\xi^2\sin^2\theta_c}\frac{\partial\Theta_0}{\partial\varphi^2} = \frac{\partial\Theta_1}{\partial\chi} + \frac{hd}{k}\frac{d_m T^*}{d^2}\Theta_1$$

$$\vdots \qquad \vdots \qquad \vdots \qquad \vdots$$

$$\frac{\partial\Theta_{n-1}}{\partial\xi^2} + \frac{1}{\xi}\frac{\partial\Theta_{n-1}}{\partial\xi} + \frac{1}{\xi^2\sin^2\theta_c}\frac{\partial\Theta_{n-1}}{\partial\varphi^2} = \frac{\partial\Theta_n}{\partial\chi} + \frac{hd}{k}\frac{d_m T^*}{d^2}\Theta_n$$

The initial conditions for these equations are given by:

(1) $\chi = 0$ $\Theta_0 = \Theta_i$, $\Theta_n = 0$ $n \neq 0$

(2) $\chi > 0$ $h = h(\xi,\varphi)$

The physical interpretation of the series solution can be obtained from an inspection of the series of differential equations. The first term in the series expansion represents the solution obtainable

A-6

from the assumption that each element acts like a calorimeter which is insulated with respect to all elements adjacent to it. Any variation in the initial wall temperature distribution, or heat transfer coefficients on the surface will lead to the establishment of temperature gradients and therefore heat conduction around or along the model. The terms associated with these temperature gradients appear as forcing functions in the differential equations for the next term in the series expansion. If one considers only the first two terms in the series, the temperature distribution can be expressed as

$$\frac{\Theta(\xi,\tau)}{\Theta_i\, e^{-\frac{h d}{k}\frac{d_m \tau}{d^2}}} = 1 + \frac{d_m \tau}{d^2}\left(\frac{\partial^2 \Theta_i}{\partial \xi^2} + \frac{1}{\xi}\frac{\partial \Theta_i}{\partial \xi} + \frac{1}{\xi^2 \sin^2\alpha}\frac{\partial^2 \Theta_i}{\partial \varphi^2}\right)$$

$$- \frac{d_m \tau}{2}\left(\frac{h d}{k}\frac{d_m \tau}{d^2}\right)\left(\frac{1}{h}\right)\left[\frac{\partial^2 h}{\partial \xi^2} + \frac{1}{\xi}\frac{\partial h}{\partial \xi} + \frac{1}{\xi^2 \sin^2\alpha}\frac{\partial^2 h}{\partial \varphi^2} + \frac{2}{\Theta_i}\frac{\partial \Theta_i}{\partial \xi}\frac{\partial h}{\partial \xi} + \frac{2}{\Theta_i}\frac{1}{\xi^2 \sin^2\alpha}\frac{\partial \Theta_i}{\partial \varphi}\frac{\partial h}{\partial \varphi}\right]$$

$$+ \frac{d_m \tau}{3}\left(\frac{h d}{k}\frac{d_m \tau}{d^2}\right)^2\left(\frac{1}{h^2}\right)\left[\left(\frac{\partial h}{\partial \xi}\right)^2 + \frac{1}{\xi^2 \sin^2\alpha}\left(\frac{\partial h}{\partial \varphi}\right)^2\right]$$

The heat transfer coefficient (h) referred to in the above analysis is the actual heat transfer coefficient associated with the flow field. The measured heat transfer coefficient is determined from the measured temperature variation with time and can be implicitly expressed as

$$\frac{\Theta(\xi,\tau)}{\Theta(\xi,\tau_i)} = e^{-\frac{h' d}{k}\frac{d_m(\tau_2-\tau_i)}{d^2}}$$

After some algebraic manipulation, the last two expressions can be combined to give the following estimate of the error in the measured heat transfer coefficients due to tangential or lateral heat conduction

$$\frac{h-h'}{h} \approx \frac{d^2 A}{(\frac{hd}{k})\Theta_i} - \alpha_m \bar{\tau} B + C\left(\frac{hd}{k}\right)\left(\frac{\alpha_m \bar{\tau}}{d^2}\right)\alpha_m \bar{\tau}$$

$$-\left[\frac{A}{\Theta_i}\frac{d^2}{(\frac{hd}{k})}\right]^2 \frac{\bar{\tau}}{\Delta\tau}\left(\frac{hd}{k}\frac{\alpha_m \bar{\tau}}{d^2}\right) - \left(\frac{8\alpha_m \bar{\tau}}{4}\right)^2\left(\frac{\alpha_m \bar{\tau}}{\alpha^2}\right)\left(\frac{hd}{k}\right)\frac{\bar{\tau}}{\Delta\tau}$$

$$-\frac{c^2}{9}(\alpha_m \bar{\tau})^2\left[\frac{hd}{k}\frac{\alpha_m \bar{\tau}}{d^2}\right]^3\frac{\bar{\tau}}{\Delta\tau} + \frac{d^2}{(\frac{hd}{k})}\frac{AB}{\Theta_i}(\alpha_m \bar{\tau})\frac{\bar{\tau}}{\Delta\tau}\left[\frac{\alpha_m \bar{\tau}}{d^2}\frac{hd}{k}\right]$$

$$-\frac{AC}{\Theta_i}\frac{2}{3}(\alpha_m \bar{\tau})^2\left(\frac{hd}{k}\frac{\alpha_m \bar{\tau}}{d^2}\right)^2\frac{\bar{\tau}}{\Delta\tau} + \frac{BC}{3}\left[\frac{hd}{k}\frac{\alpha_m \bar{\tau}}{d^2}\right]\frac{\bar{\tau}}{\Delta\tau}(\alpha_m \bar{\tau})^2$$

$$A = \left[\frac{\partial^2 \Theta_i}{\partial\xi^2} + \frac{1}{\xi}\frac{\partial\Theta_i}{\partial\xi} + \frac{1}{\xi^2\sin^2\alpha}\frac{\partial^2\Theta_i}{\partial\varphi^2}\right]$$

$$B = \frac{1}{h}\left[\frac{\partial^2 h}{\partial\xi^2} + \frac{1}{\xi}\frac{\partial h}{\partial\xi} + \frac{1}{\xi^2\sin^2\alpha}\frac{\partial^2 h}{\partial\varphi^2} + \frac{2}{\Theta_i}\frac{\partial\Theta_i}{\partial\xi}\frac{\partial h}{\partial\xi} + \frac{2}{\xi^2\sin^2\alpha}\frac{1}{\Theta_i}\frac{\partial\Theta_i}{\partial\varphi}\frac{\partial h}{\partial\varphi}\right]$$

$$C = \frac{1}{h}\left[\left(\frac{\partial h}{\partial\xi}\right)^2 + \frac{1}{\xi^2\sin^2\alpha}\left(\frac{\partial h}{\partial\varphi}\right)^2\right]$$

$$\bar{\tau} = \frac{\tau_1 + \tau_2}{2} \approx \sqrt{\tau_1 \tau_2}$$

$$\Delta\tau = \tau_2 - \tau_1$$

If

$$\frac{A d^2}{(\frac{hd}{k})\Theta_i}, \quad \alpha_m\bar{\tau} B, \quad C\left(\frac{hd}{k}\right)\frac{\alpha_m\bar{\tau}}{d^2} \quad\text{and}\quad \frac{hd}{k}\frac{\alpha_m\bar{\tau}}{d^2}$$

are of the order of 0.1, then for Fourier numbers and non-dimensional time increments of the order of 1.0, the above expression is approximated by

$$\frac{h-h'}{h} \approx \frac{d^2 A}{(\frac{hd}{k})\Theta_i} - \alpha_m\bar{\tau} B + C\left(\frac{hd}{k}\frac{\alpha_m\bar{\tau}}{d^2}\right)\alpha_m\bar{\tau}$$

The first and third term in the above expression are dependent upon the initial temperature gradient and convective heat transfer gradients respectively. The second term is dependent upon the variation of the convective heat transfer gradients and the initial temperature gradients.

In order to minimize the effects of lateral heat conduction in wind tunnel heat transfer experiments, it is desirable to obtain the

A-8

data as close to the initial instant as possible. However, as noted in the previous section, a time of approximately one Fourier number must elapse before valid measurements can be made by the transient calorimeter approximation.

Two additional restrictions which limit the minimum time at which the measurements can be made are the response time of sampling rate of the data recording system, and the time required to establish flow around the model.

In the present series of experiments conduction errors are introduced due to two primary factors.

(1) Some of the heat transfer measurements were obtained in regions on the cone where large circumferential gradients in the heat transfer coefficient occur.

(2) An initial temperature gradient is introduced on the surface of the cone because useful flow was not instantaneously established around the model. The delay in establishing useful flow is due to the fact that the cooling shield, which covers the model while steady flow is established in the test section, is withdrawn at a speed of approximately 2 ft/sec. Consequently, when the model is at the largest angle of attack, approximately 0.5 second passes before the tip of the cone is exposed to the incident flow. During this period a temperature gradient is established around the model surface due to the differences in the amounts of convective heat transfer that each portion of the model has experienced.

Since the thermocouples were situated along rays that were 180° removed from each other, it was impossible to measure the initial circumferential temperature gradients. In order to obtain an

estimate for the tangential heat conduction in the measured heat
transfer data, it is assumed that the presence of the cooling shield
does not alter the heat transfer coefficient from its true value.
This assumption neglects the problem associated with the interaction
between the shock wave from the shield and the boundary layer on the
cone. One can therefore express the error introduced by this initial
gradient as

$$\frac{d^2 A}{d\xi}\Theta_i \approx -\alpha_m \bar{\tau}_i \left[\frac{\partial (\ell_n h)}{\partial \xi^2} + \left[\frac{\partial (\ell_n h)}{\partial \xi} \right] \left\{ 1 + \frac{hd}{k}\frac{\alpha_m \bar{\tau}}{d\xi} \right\} + \frac{1}{\xi}\frac{\partial h}{\partial \xi} + \frac{1}{\xi^2 \sin^2 \alpha} \left\{ \frac{\partial^2 h}{\partial \psi^2} + \left[\frac{\partial \ell_n h}{\partial \psi} \right]^2 \right\} \left(1 + \frac{hd}{k} \chi 1 + \frac{\bar{\tau}}{\xi}\frac{hd}{k} \right) \right]$$

The quantity $\bar{\tau}_1$ is the time required for the shield to clear the
model at each point. This time is approximated by the relationship

$$\bar{\tau}_1 = \xi \, \sin(\psi + \alpha_c) / V_s \qquad\qquad V_s = \text{shield speed}$$

Substituting these results into the expression for the error
associated with tangential heat conduction, one obtains

$$\frac{h - h'}{h} \approx \left\{ \alpha_m \frac{\xi \sin(\psi + \alpha_c)}{V_s} \right\} \left\{ \frac{\partial^2 (\ell_n h)}{\partial \xi^2} + \left[\frac{\partial (\ell_n h)}{\partial \xi} \right]^2 \left[1 + \frac{hd}{k}\frac{\alpha_m}{d\xi}\frac{\xi \sin(\psi + \alpha_c)}{V_s} \right] + \frac{1}{\xi}\frac{\partial (\ell_n h)}{\partial \xi} \right.$$
$$\left. + \frac{1}{\xi^2 \sin^2 \alpha} \left[\frac{\partial^2 \ell_n h}{\partial \psi^2} + \left[\frac{\partial \ell_n h}{\partial \psi} \right]^2 \left[1 + \left(\frac{hd}{k}\right)\left(1 + \frac{hd}{k}\frac{\alpha_m \sin(\psi + \alpha)}{d\xi}\frac{\xi}{V_s} \right) \right] \right] \right\}$$
$$- \frac{\alpha_m \bar{\tau}}{h} \left\{ \frac{\partial^2 h}{\partial \xi^2} + \frac{1}{\xi}\frac{\partial h}{\partial \xi} + \frac{1}{\xi^2 \sin^2 \alpha}\frac{\partial^2 h}{\partial \psi^2} - 2\frac{hd}{k}\frac{\alpha_m \xi \sin(\psi + \theta_c)}{V_s}\left(\frac{1}{h}\left(\frac{\partial h}{\partial \xi}\right)^2 + \frac{1}{h \xi^2 \sin^2 \alpha}\left(\frac{\partial h}{\partial \psi}\right)^2 \right) \right\}$$
$$+ \alpha_m \bar{\tau}\left(\frac{hd}{k}\frac{\alpha_m \bar{\tau}}{d\xi} \right)\frac{1}{h^2}\left\{ \left(\frac{\partial h}{\partial \xi}\right)^2 + \frac{1}{\xi^2 \sin^2 \alpha}\left(\frac{\partial h}{\partial \psi}\right)^2 \right\}$$

It is noted that the relative error in transient heat transfer measurements due to tangential heat conduction depends upon the location on the cone, the heat transfer distribution and the time at which the measurements are made.

An estimate of the error associated with the measured heat transfer rate on the most windward streamline of the cone is presented in figure (A-4). These results were determined from the above formula with the following assumptions.

(1) windward heat transfer distribution: $h_o = c_1 \xi^{-0.25}$

(2) circumferential heat transfer distribution: $\frac{h}{h_o} = \cos^{3/2}\varphi$

(3) constant Biot number: $hd'/k = 0.1$

(4) shield speed: $V_s = 24$ inches/sec

(5) thermal diffusivity: $\alpha_m = 7.2 \times 10^{-3}$ (inches)^2/sec

(6) angle of attack: $\alpha = 55^\circ$

(7) wall thickness (d') = 0.020 inch

For the windward streamline case considered, heat conduction in the circumferential direction introduced the largest contribution to the conduction error. The results indicate that by taking the measurements within 0.20 seconds from the establishment of flow, the error due to tangential conduction in the windward measurements will be less than 10 percent at stations beyond 1.75 inches from the tip. In order to reduce the error in the data obtained at the thermocouple located 1.00 inches from the tip it was necessary to use the data obtained at approximately 0.10 second from the establishment of the flow. (Data could not be obtained any earlier than this time since approximately 0.110 second elapsed between measurements at each thermocouple.)

In view of the fact that tangential conduction effects required that the data be obtained at approximately 0.1-0.2 second from the time flow was established (Fourier number ≈ 2), the effects associated with normal conduction should also be considered. The maximum estimated relative errors associated with the windward streamline measurements due to normal and tangential conduction are tabulated below:

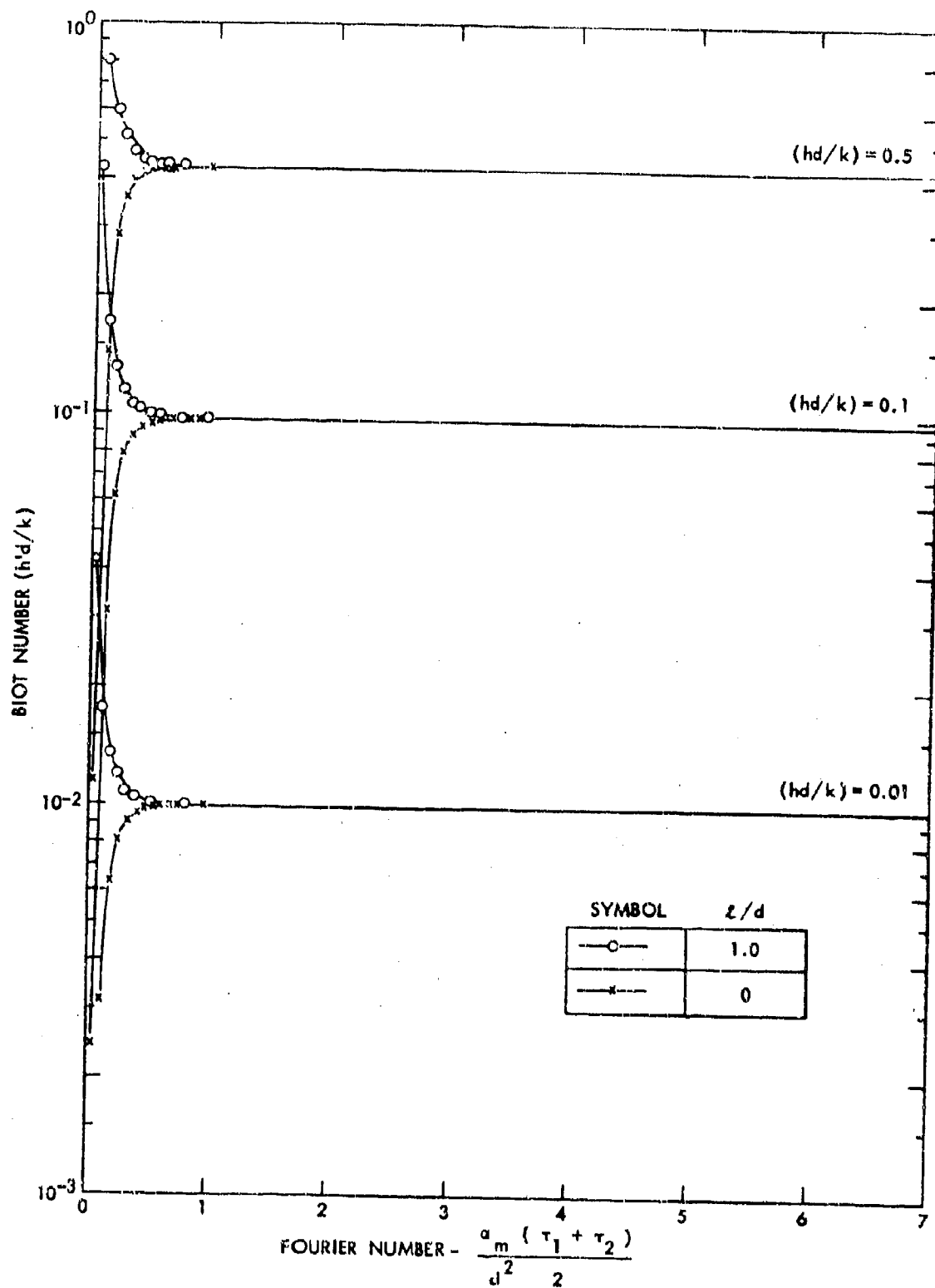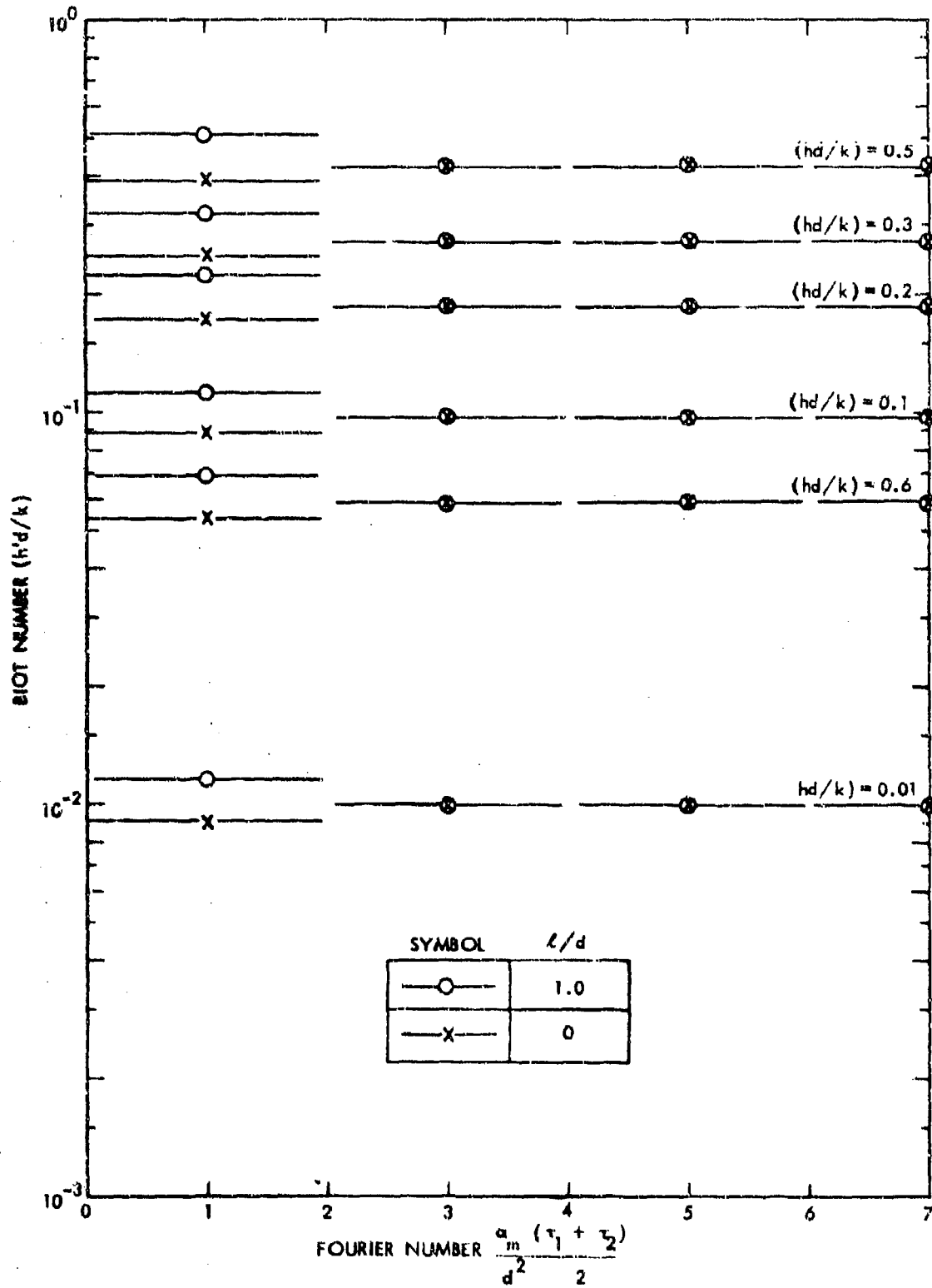| X	$\frac{h-h'}{h}$ Normal Conduction	$\frac{h-h'}{h}$ Tangential Conduction
1.00	±0.08	+0.21
1.75	±0.08	+0.10
2.50	±0.08	+0.06
3.25	±0.08	+0.04
6.25	±0.08	+0.02
7.00	±0.08	+0.02
7.75	±0.08	+0.01
8.50	±0.08	+0.01
9.25	±0.08	+0.01
10.75	±0.08	+0.01

FIG. A-1 CALCULATED BIOT NUMBER VARIATION WITH FOURIER NUMBER - $\frac{\alpha_m}{d^2} \frac{(\tau_2 - \tau_1)}{} = 0.07$

FIG. A-2 CALCULATED BIOT NUMBER VARIATION WITH FOURIER NUMBER $\frac{\alpha_m(\tau_2 - \tau_1)}{d^2} = 2.0$

$\Delta h = h - h''$ (EQU. A-4)

$\Delta h = h - h'$ (EQU. A-1)
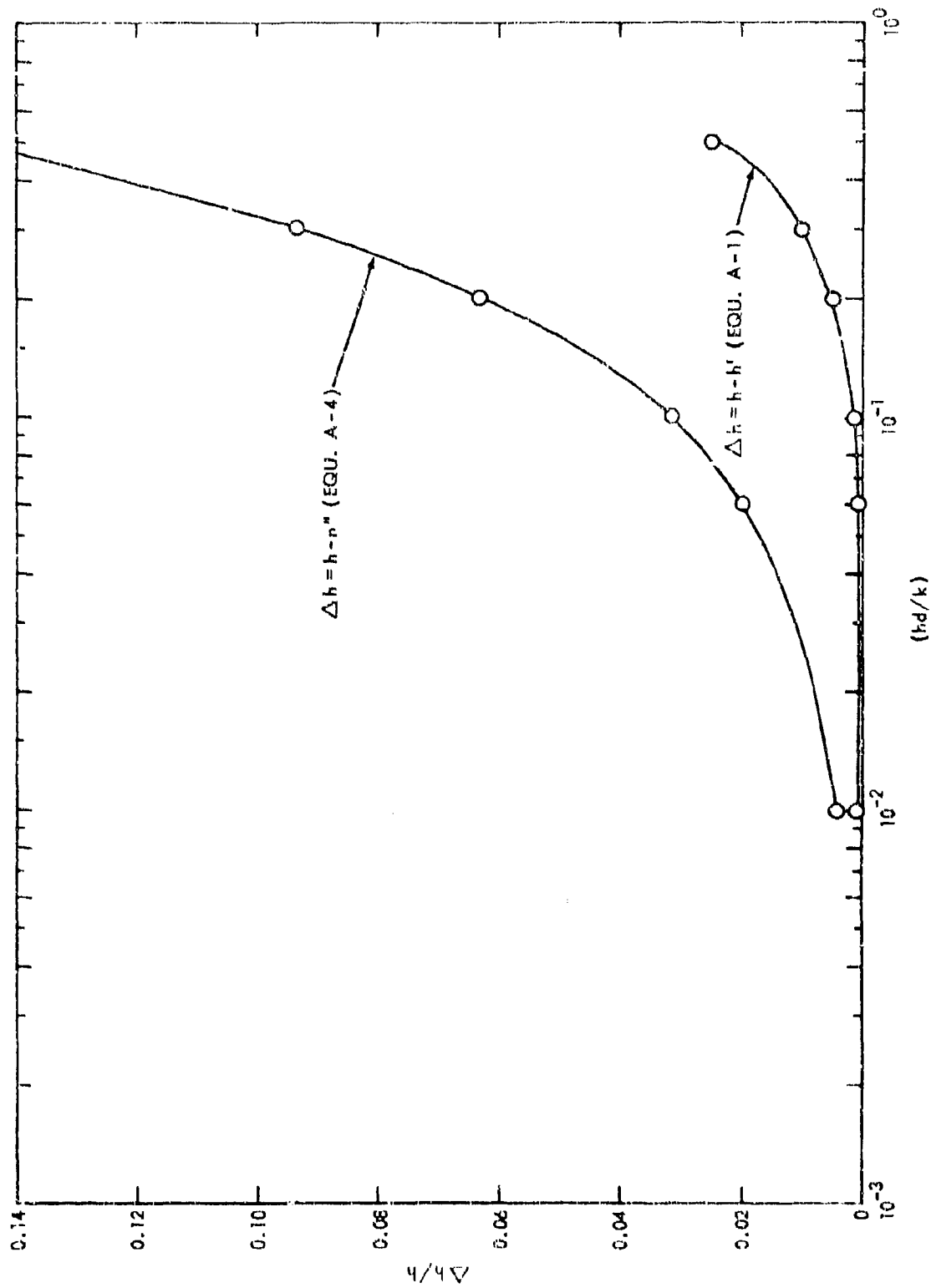
(hd/k)

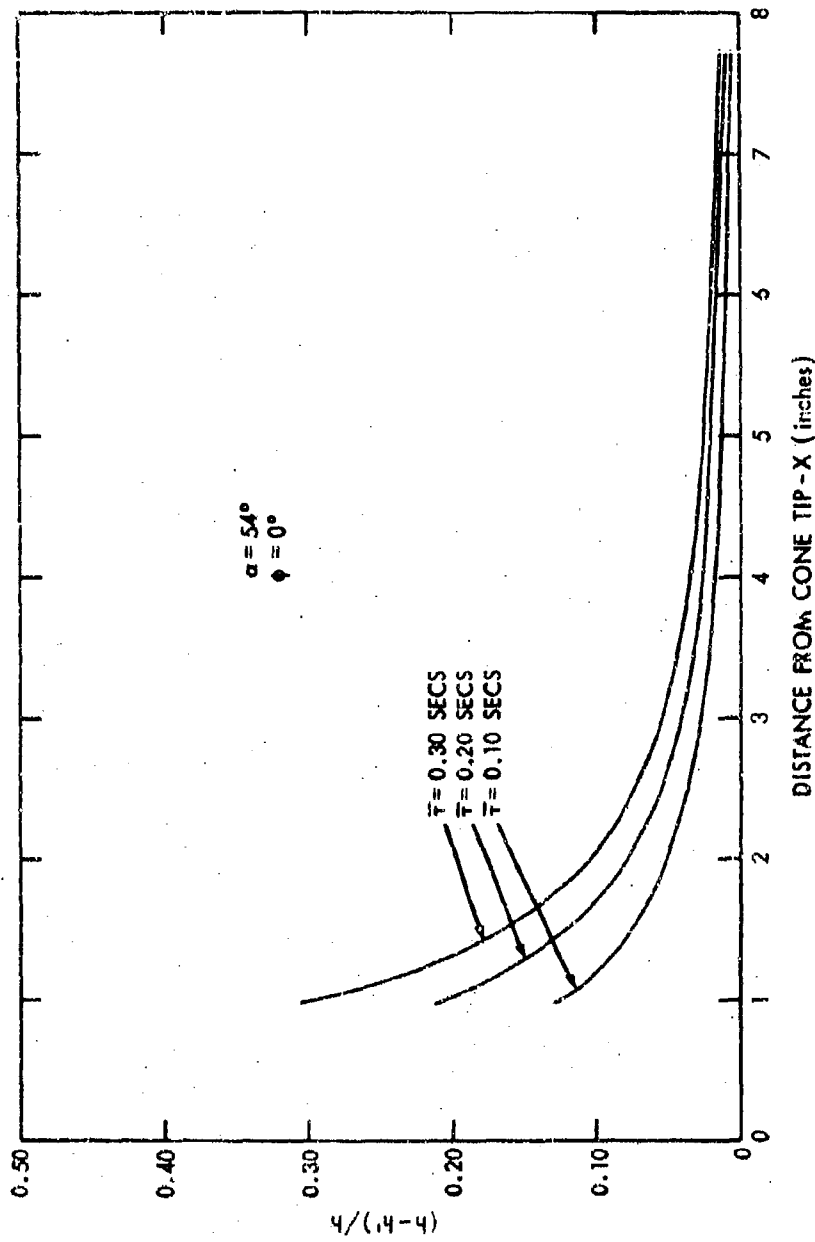$\Delta h/h$

FIG. A-3 ERROR IN CALCULATED BIOT NUMBER DUE TO NORMAL HEAT CONDUCTION

FIG. A-4 ESTIMATED ERROR IN MEASURED STAGNATION STREAMLINE HEAT TRANSFER DATA DUE TO TANGENTIAL HEAT CONDUCTION

DOCUMENT CONTROL DATA - R&D

(Security classification of title, body of abstract and indexing annotation must be entered when the overall report is classified)

1 ORIGINATING ACTIVITY (Corporate author)	2a. REPORT SECURITY CLASSIFICATION
U. S. Naval Ordnance Laboratory White Oak, Silver Spring, Maryland	UNCLASSIFIED
	2b. GROUP

3. REPORT TITLE

AN EXPERIMENTAL INVESTIGATION OF THE AERODYNAMIC CHARACTERISTICS OF SLENDER HYPERSONIC VEHICLES AT HIGH ANGLES OF ATTACK

4. DESCRIPTIVE NOTES *(Type of report and inclusive dates)*
final

5. AUTHOR(S) *(Last name, first name, initial)*
Feldhuhn, Robert H.
Pasiuk, Lionel

6. REPORT DATE	7a. TOTAL NO. OF PAGES	7b. NO. OF REFS
1 May 1968	46	24

8a. CONTRACT OR GRANT NO.	9a. ORIGINATOR'S REPORT NUMBER(S)
b. PROJECT NO.	NOLTR 68-52
c.	9b. OTHER REPORT NO(S) (Any other numbers that may be assigned this report)
d.	

10. AVAILABILITY/LIMITATION NOTICES

This document is subject to special export controls and each transmittal to foreign governments may be made only with prior approval of NOL.

11. SUPPLEMENTARY NOTES	12. SPONSORING MILITARY ACTIVITY

13. ABSTRACT

Pressure, heat transfer, force, flow field surveys and flow visualization measurements on an inclined cone were obtained in a wind tunnel at a nominal Mach number of 6. Force measurements were also obtained for a 2/3 power law body and two ducted-cone configurations.

DD ₁ᶠᴼᴿᴹⱼₐₙ₆₄ 1473

14. KEY WORDS	LINK A		LINK B		LINK C	
	ROLE	WT	ROLE	WT	ROLE	WT
1. cones						
2. aerodynamics						
3. heat transfer						
4. pressure distribution						
5. flow visualization						
6. force measurements						

INSTRUCTIONS

1. ORIGINATING ACTIVITY: Enter the name and address of the contractor, subcontractor, grantee, Department of Defense activity or other organization (corporate author) issuing the report.

2a. REPORT SECURITY CLASSIFICATION: Enter the overall security classification of the report. Indicate whether "Restricted Data" is included. Marking is to be in accordance with appropriate security regulations.

2b. GROUP: Automatic downgrading is specified in DoD Directive 5200.10 and Armed Forces Industrial Manual. Enter the group number. Also, when applicable, show that optional markings have been used for Group 3 and Group 4 as authorized.

3. REPORT TITLE: Enter the complete report title in all capital letters. Titles in all cases should be unclassified. If a meaningful title cannot be selected without classification, show title classification in all capitals in parenthesis immediately following the title.

4. DESCRIPTIVE NOTES: If appropriate, enter the type of report, e.g., interim, progress, summary, annual, or final. Give the inclusive dates when a specific reporting period is covered.

5. AUTHOR(S): Enter the name(s) of author(s) as shown on or in the report. Enter last name, first name, middle initial. If military, show rank and branch of service. The name of the principal author is an absolute minimum requirement.

6. REPORT DATE: Enter the date of the report as day, month, year; or month, year. If more than one date appears on the report, use date of publication.

7a. TOTAL NUMBER OF PAGES: The total page count should follow normal pagination procedures, i.e., enter the number of pages containing information.

7b. NUMBER OF REFERENCES: Enter the total number of references cited in the report.

8a. CONTRACT OR GRANT NUMBER: If appropriate, enter the applicable number of the contract or grant under which the report was written.

8b, 8c, & 8d. PROJECT NUMBER: Enter the appropriate military department identification, such as project number, subproject number, system numbers, task number, etc.

9a. ORIGINATOR'S REPORT NUMBER(S): Enter the official report number by which the document will be identified and controlled by the originating activity. This number must be unique to this report.

9b. OTHER REPORT NUMBER(S): If the report has been assigned any other report numbers (either by the originator or by the sponsor), also enter this number(s).

10. AVAILABILITY/LIMITATION NOTICES: Enter any limitations on further dissemination of the report, other than those imposed by security classification, using standard statements such as:

(1) "Qualified requesters may obtain copies of this report from DDC."

(2) "Foreign announcement and dissemination of this report by DDC is not authorized."

(3) "U. S. Government agencies may obtain copies of this report directly from DDC. Other qualified DDC users shall request through

_____."

(4) "U. S. military agencies may obtain copies of this report directly from DDC. Other qualified users shall request through

_____."

(5) "All distribution of this report is controlled. Qualified DDC users shall request through

_____."

If the report has been furnished to the Office of Technical Services, Department of Commerce, for sale to the public, indicate this fact and enter the price, if known.

11. SUPPLEMENTARY NOTES: Use for additional explanatory notes.

12. SPONSORING MILITARY ACTIVITY: Enter the name of the departmental project office or laboratory sponsoring (paying for) the research and development. Include address.

13. ABSTRACT: Enter an abstract giving a brief and factual summary of the document indicative of the report, even though it may also appear elsewhere in the body of the technical report. If additional space is required, a continuation sheet shall be attached.

It is highly desirable that the abstract of classified reports be unclassified. Each paragraph of the abstract shall end with an indication of the military security classification of the information in the paragraph, represented as (TS), (S), (C), or (U).

There is no limitation on the length of the abstract. However, the suggested length is from 150 to 225 words.

14. KEY WORDS: Key words are technically meaningful terms or short phrases that characterize a report and may be used as index entries for cataloging the report. Key words must be selected so that no security classification is required. Identifiers, such as equipment model designation, trade name, military project code name, geographic location, may be used as key words but will be followed by an indication of technical context. The assignment of links, roles, and weights is optional.